UNIVERSITAT ROVIRA I VIRGILI

SELF-OSCILLATING RESONANT CONVERTERS: GENERAL APPROACH AND APPLICATIONS

Ricardo Bonache Samaniego

ADVERTIMENT. L'accés als continguts d'aquesta tesi doctoral i la seva utilització ha de respectar els drets de la persona autora. Pot ser utilitzada per a consulta o estudi personal, així com en activitats o materials d'investigació i docència en els termes establerts a l'art. 32 del Text Refós de la Llei de Propietat Intel·lectual (RDL 1/1996). Per altres utilitzacions es requereix l'autorització prèvia i expressa de la persona autora. En qualsevol cas, en la utilització dels seus continguts caldrà indicar de forma clara el nom i cognoms de la persona autora i el títol de la tesi doctoral. No s'autoritza la seva reproducció o altres formes d'explotació efectuades amb finalitats de lucre ni la seva comunicació pública des d'un lloc aliè al servei TDX. Tampoc s'autoritza la presentació del seu contingut en una finestra o marc aliè a TDX (framing). Aquesta reserva de drets afecta tant als continguts de la tesi com als seus resums i índexs.

ADVERTENCIA. El acceso a los contenidos de esta tesis doctoral y su utilización debe respetar los derechos de la persona autora. Puede ser utilizada para consulta o estudio personal, así como en actividades o materiales de investigación y docencia en los términos establecidos en el art. 32 del Texto Refundido de la Ley de Propiedad Intelectual (RDL 1/1996). Para otros usos se requiere la autorización previa y expresa de la persona autora. En cualquier caso, en la utilización de sus contenidos se deberá indicar de forma clara el nombre y apellidos de la persona autora y el título de la tesis doctoral. No se autoriza su reproducción u otras formas de explotación efectuadas con fines lucrativos ni su comunicación pública desde un sitio ajeno al servicio TDR. Tampoco se autoriza la presentación de su contenido en una ventana o marco ajeno a TDR (framing). Esta reserva de derechos afecta tanto al contenido de la tesis como a sus resúmenes e índices.

WARNING. Access to the contents of this doctoral thesis and its use must respect the rights of the author. It can be used for reference or private study, as well as research and learning activities or materials in the terms established by the 32nd article of the Spanish Consolidated Copyright Act (RDL 1/1996). Express and previous authorization of the author is required for any other uses. In any case, when using its content, full name of the author and title of the thesis must be clearly indicated. Reproduction or other forms of for profit use or public communication from outside TDX service is not allowed. Presentation of its content in a window or frame external to TDX (framing) is not authorized either. These rights affect both the content of the thesis and its abstracts and indexes.

UNIVERSITAT
ROVIRA i VIRGILI

Self-oscillating resonant converters: general approach and applications

Ricardo Bonache Samaniego

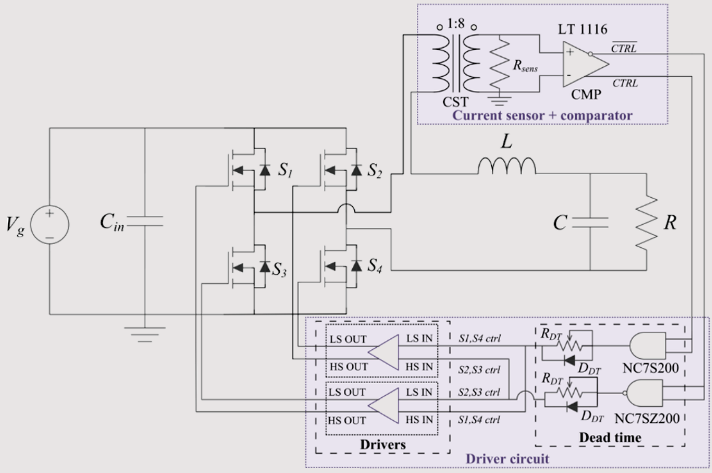

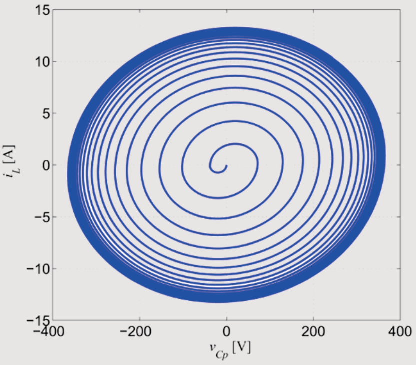

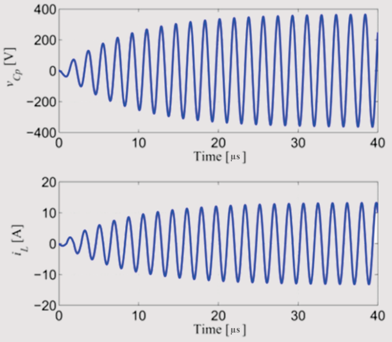

DOCTORAL THESIS

2016

Ricardo Bonache Samaniego

Self-oscillating resonant converters: general approach and applications

Doctoral Thesis

Thesis Advisors
Dr. Carlos Olalla Martínez
Dr. Luís Martínez Salamero

Department of Electronic, Electric and Automatic Control Engineering

Automatic Control and Industrial Electronics Group

UNIVERSITAT ROVIRA I VIRGILI

Tarragona 2016

UNIVERSITAT
ROVIRA I VIRGILI

FEM CONSTAR que aquest treball, titulat “Self-oscillating resonant converters: general theory and applications” i presentat per Ricardo Bonache Samaniego per a l’obtenció del títol de Doctor, ha estat realitzat sota la nostra direcció al Departament d’Enginyeria Electrònica Elèctrica i Automàtica d’aquesta universitat i acompleix els requisits per a poder optar a la Menció Internacional.

HACEMOS CONSTAR que el presente trabajo, titulado “Self-oscillating resonant converters: general theory and applications” y presentado por Ricardo Bonache Samaniego para la obtención del título de Doctor, ha sido realizado bajo nuestra dirección en el Departamento de Ingeniería Electrónica Eléctrica y Automática de esta universidad y cumple los requisitos para poder optar a la Mención Internacional.

WE STATE that the present study, entitled “Self-oscillating resonant converters: general theory and applications”, presented by Ricardo Bonache Samaniego for the award of the degree of Doctor, has been carried out under our supervision at the Department of Electronic, Electric and Automatic Control Engineering of this university and accomplishes all the requirements for being granted with the International Mention.

Tarragona, 15 December 2016

El/s director/s de la tesi doctoral
El/los director/es de la tesis doctoral
Doctoral Thesis Supervisor/s

Luís Martínez Salamero

Carlos Olalla Martínez

ACKNOWLEDGEMENTS

Everything that has a beginning has an end. This PhD Thesis is the result of three years of work in which the help of several people has lessened the burden. These lines are devoted to these people who contributed to the completion of this work.

In first place thanks to my advisors, Luis Martínez Salamero and Carlos Olalla. Both have shared their deep knowledge and passion about Electronic Engineering, having always helped me in finding a solution to the problems encountered.

In addition, thanks to all my colleagues at the GAEI laboratory. I have enjoyed each minute in the laboratory with you. Thanks for all the help and for all the funny moments together.

Special thanks to professor Dragan Maksimovic for accepting me as a visitor student in the CoPEC laboratory and for sharing his time and knowledge with me. Thanks for giving me the opportunity to stay in Boulder and live a life-changing experience. Additionally, thanks to all the students in the CoPEC laboratory and to all the new friends in Boulder. They have shared lots of hours of conversation with me and have helped me in the difficult moments.

Deep thanks to my parents, Jose Bonache and Esther Samaniego, for everything. Lots of people have helped to accomplish this work but it is really true that without you I would have never done it. Indeed, I would not be who I am. Thanks for your guidance during all my life, for all your help on countless occasions and for letting me be what I wanted to be and supporting me always. Deep thanks also to my chosen family, Veronica Rodriguez, with whom I have shared all the ups and downs during the realization of this work. Your trust on me has pushed me forward. This research also belongs to all of you.

Furthermore, thanks to my life-long friends, not to forget those who I happened to meet during these recent years. You have supported me always. Thanks for making my day easier and for listening me whenever I needed.

Finally, I want to mention that this work is not only a scientific document, it is also the materialization of a path around a life-changing experience and is not only the result of the author's work, it is the result of lots of people that supported and helped me in some extent. It has been a long path, plenty of challenges and difficulties but also of grateful days and huge rewards. Thanks to all of them.

Thesis written by Ricardo Bonache Samaniego

Self-oscillating resonant converters: general approach and applications

Ph.D. in Technologies for Nanosystems, Bioengineering and Energy

The work presented in this PhD Thesis has been funded by the Spanish Ministry of Economy and Competitiveness under grants DPI2012-31580/BES-2013-063288, EEBB-I-2016-10687 and CSD2009-00046.

The research leading to the results presented here has been developed in Universitat Rovira i Virgili, Tarragona, Spain and University of Colorado at Boulder, Boulder, Colorado, USA; under supervision of Dr. Carlos Olalla Martínez and Dr. Luís Martínez Salamero at Universitat Rovira i Virgili and Dr. Dragan Maksimovic at University of Colorado.

To my beloved family and friends, who have supported and trusted me during this long path.

CONTENTS

ABSTRACT

Self-oscillation in resonant converters is a simple operating mode to generate a sinusoidal signal without requiring an external reference. Scattered in the literature, this mode has been attained by means of different techniques, all having in common the change of the input voltage polarity induced by the internal state of the resonant converter. Due to this spread, the absence of a unified approach in their analysis and the inherent delay in the different processing stages of the feedback path, self-oscillating converters have been relegated to the margins of the main stream in resonant converters, which is largely dominated by a frequency modulation-based operating mode.

A general approach for self-oscillating resonant converters is presented in this dissertation for a particular class of circuits in which the change of input voltage polarity is caused by the zero-crossings of the input inductor current. The key features of the method are an analytical description in the time-domain of a spiral that eventually converges into an ellipse, and a frequency-domain analysis that explains the behavior of the ellipse as a limit cycle. On a theoretical basis, this class of circuits behaves as loss-free resistors because in steady-state the input inductor current is in phase with the first harmonic of the input voltage.

The proposed analytical procedure predicts accurately the amplitude and frequency of the limit cycle and justifies the stability of its generation. This accuracy is reflected in the close agreement between the theoretical expressions and the corresponding simulated and measured waveforms. Second, third and fourth order resonant converters are designed following simple guidelines derived from the theoretical analysis. In addition, a voltage regulation loop is inserted to fully exploit the benefits of the self-oscillation by mitigating the effect of the perturbations entering through the input voltage or the output load.

The problem of delay in the control feedback path is appropriately compensated when dealing with the practical implementation of this class of resonant converters in view of its industrial applications.

1

CHAPTER 1

INTRODUCTION

Despite being intensively researched during the last decades, resonant converters exist since the early years of the 19th century and the concept of resonance dates back to the 18th century. Specifically, in 1826 Felix Savary observed and described by the first time the existence of an oscillatory electric discharge with changing polarity in an experiment with a Leyden jar [1]. Later, in 1885, Nikola Tesla studied and applied this concept in different practical experiments made by him [2], but it was not until 1887 when the term "Resonance" was introduced by the first time in literature [3, 4]. However, this concept has not been applied to power conversion until the decade of 1930s [4], when resonant structures were introduced in radio equipment in order to avoid the high current peaks that appeared in relay switch contacts [4]. This application represented the first kind of resonant power converter. An example of it, called vibrator, was published in 1947 [5] and is shown in Fig. 1.1. Concepts intrinsically associated with resonant converters, such as zero voltage switching (ZVS), zero current switching (ZCS) and soft-switching [6] were also mentioned during those decades, though still not named as such.

The appearance of transistors in the mid-1950s made unnecessary the use of vibrators. As a result, research was paused until 1981. As explained in [4], in April of 1981 R. Goldfarb exposed the use of the transformer magnetizing inductance to "recover the charge on the snubber capacitors" [7]. Dead-time was applied for resonant transitions. The same year, B. Carsten published a paper [8] using an active clamp in a forward converter that utilized both the magnetizing and leakage inductances for soft-switching. These works rekindled the interest of researchers in resonant conversion.

Despite these early publications, interest did not grow until 1990, when an important increase in research could be appreciated. Up to then, the main research efforts focused on PWM converters and hard-switching, as size and efficiency were acceptable for the available technology and the applications. The approach of

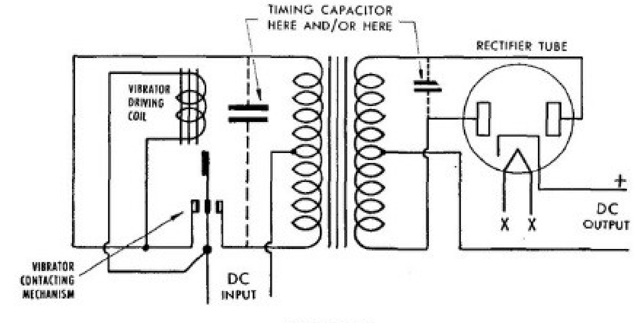

Figure 7

Figure 1.1: Basic vibrator circuit. Extracted from [4].

hard-switching converters to its maximum switching frequency, which limits the minimum size, and the increasing introduction of devices based on AC power supplies renovated the interest on resonant converters.

Application of resonant converters has been focused in areas were high currents or voltages are required. In the 1970s and the 1980s they were used mainly in industrial inductive heating applications for metal melting [9], being introduced in the early 1990s into the medical sector as high-intensity magnetic-field generators [10]. In the last part of that decade they were also applied in telecommunications networks [11], in efficient lightning applications [12–16], and in domestic inductive heating [17, 18]. Nowadays, resonant converters represent the core of future charging solutions such as wireless charge for electric vehicles [19, 20] while they continue to be applied in the fields mentioned above.

1.1 Basics of resonant converters

A resonant power converter, as depicted in Fig. 1.2, is composed of: (a) a switch network, (b) the resonant tank and (c) a rectifier or a load. The switch network can be realized with a half-bridge or a full-bridge topology, whereas the resonant tank can present different configurations based on the position and the number of reactive elements (inductors and capacitors).

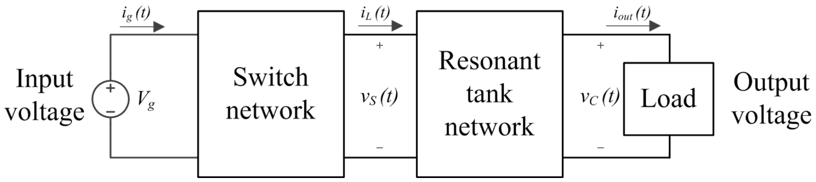

Figure 1.2: General scheme of a resonant converter.

Depending on the circuit configuration, hundreds of different 2nd, 3rd and 4th order resonant tanks exist. Fig. 1.3 shows the five most common resonant tanks applied in resonant power supplies: the series resonant converter (SRC) (Fig. 1.3a), the parallel resonant converter (PRC) (Fig. 1.3b), the series-parallel LCC-type resonant converter (LCC) (Fig. 1.3c), the series-parallel LLC-type resonant converter (LLC) (Fig. 1.3d) and the series-parallel LCLC-type resonant converter (LCLC) (Fig. 1.3e).

This work is focused on analyzing these general structures, which are characterized by their different input-output voltage transfer function $H(s)$ and their input and output impedance transfer functions $Zi(s)$ and $Zo(s)$ respectively. As shown in Fig. 1.4, series resonant converters only allow to reduce the first harmonic of the input voltage, whereas parallel resonant converters allow to increase

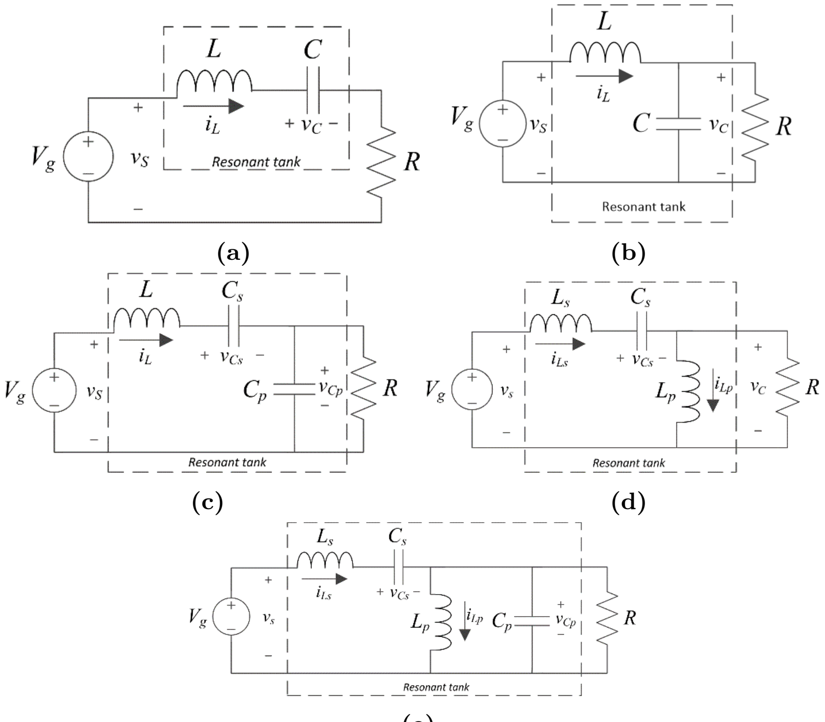

(a) (b) (c) (d) (e)

Figure 1.3: Resonant tank structures for (a) series resonant converter (SRC), (b) parallel resonant converter (PRC), (c) LCC resonant converter, (d) LLC resonant converter and (e) LCLC resonant converter.

or reduce it, depending on the switching frequency.

Regarding third order tanks, the LLC and LCC permit a flexible operation, as their response is based on a combination of the behavior of the series and parallel resonant converters, depending on the switching frequency and the load. Generally, the LLC and the LCC may be seen as a modification of the SRC and the PRC respectively, presenting a similar input-output behavior under particular conditions. The fourth order LCLC tank also presents a combination of series and parallel resonant converters, and it is typically used in applications where a large gain ratio is required.

In general, resonant converters are characterized by their capability of achieving zero voltage switching or zero current switching, reducing the switching losses and being able to switch at higher frequencies when compared with hard-switching converters. This characteristic enables the use of reactive components of reduced values, which is especially important if the converter requires inductors, as they typically limit the size and weight of the resulting converter.

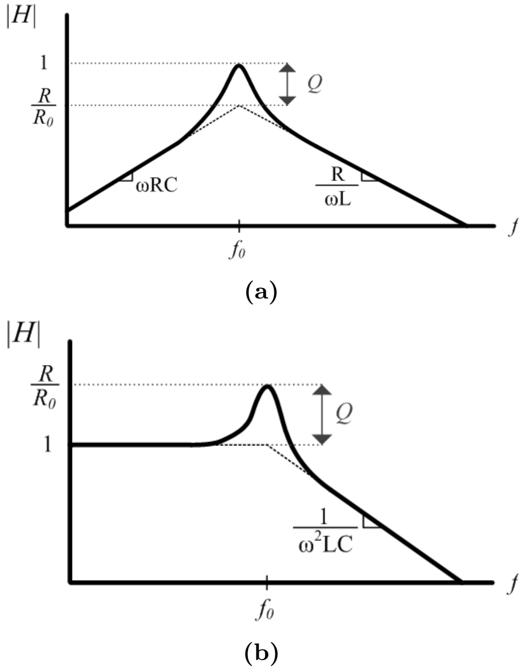

Figure 1.4: Bode plot of the input-output transfer function $H(s)$ of the: (a) SRC, (b) PRC.

ZVS or ZCS are accomplished by phase-shifting voltage and current across the switches, or equivalently, at the input of the resonant tank. Given that the resonant tank is composed of passive reactive components, it is possible to design a tank with a predefined resonant frequency and to set a switching frequency with enough deviation with respect to the resonant frequency that provides ZVS or ZCS.

ZVS is accomplished when the resonant tank input current is lagging behind the resonant tank input voltage and ZCS when the opposite condition is given. Taking as example the circuit shown in Fig. 1.5a it is possible to visualize how ZVS and ZCS are accomplished. In Fig. 1.5b it is shown that if the current is negatively phase-shifted with respect to the voltage, i.e., when the voltage leads the current, there exist a time when the diodes D_2 and D_3 (or its opposites in the next semicycle) are activated while Q_2 and Q_3 drain-source voltages are approximately zero. During that period it is possible to activate the switches at zero voltage (i.e.: ZVS) before the current becomes negative.

ZCS is obtained similarly if the current leads the voltage, as illustrated in Fig. 1.5c. In that situation, before deactivating Q_1 and Q_4, the current is negative and flows through the associated diodes, and it is possible to turn them off at any

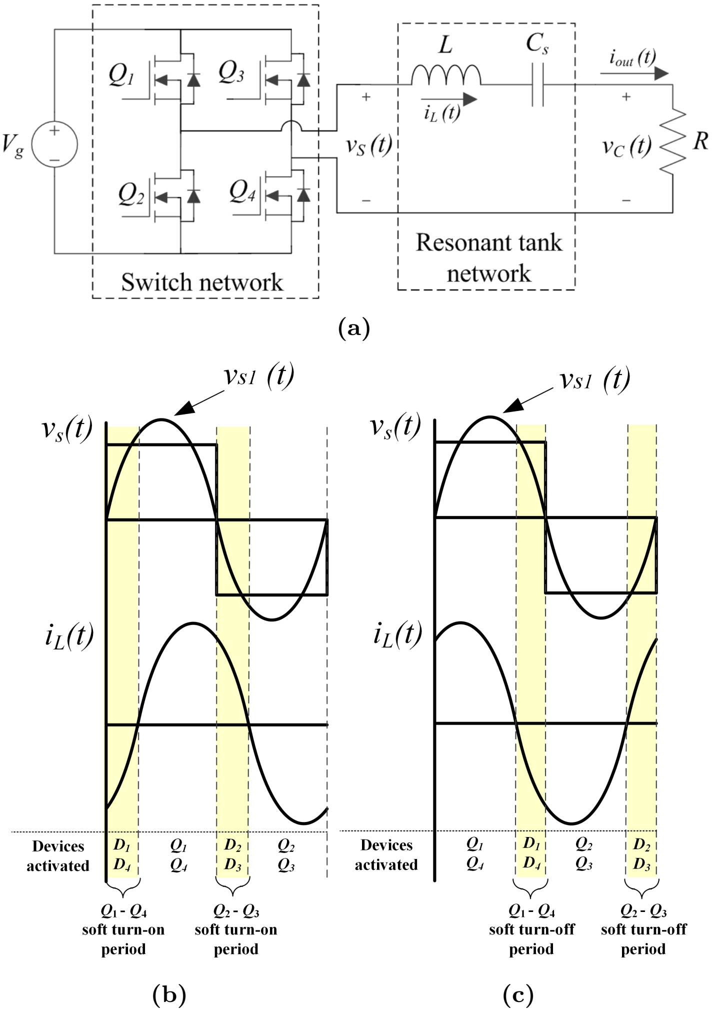

Figure 1.5: (a) Series resonant example, (b) ZVS operation, (c) ZCS operation.

time. On the contrary, the devices to be activated (Q_2 and Q_3) will experience a hard turn-on.

ZVS and ZCS may be obtained with any resonant structure depending on whether the input impedance is inductive or capacitive respectively. In order to illustrate this, Fig. 1.6 shows the Bode plots of the input impedance gain $|Z_i|$ for the SRC, PRC and LCC. In the SRC, ZVS is accomplished at frequencies higher than the resonant frequency. In the PRC, the frontier between ZVS and ZCS depends on the load. In presence of a light load, ZVS and ZCS are accomplished as in the SRC. In presence of a heavy load, there exist an intersection between capacitive and inductive behavior below the resonant frequency f_0, identified as

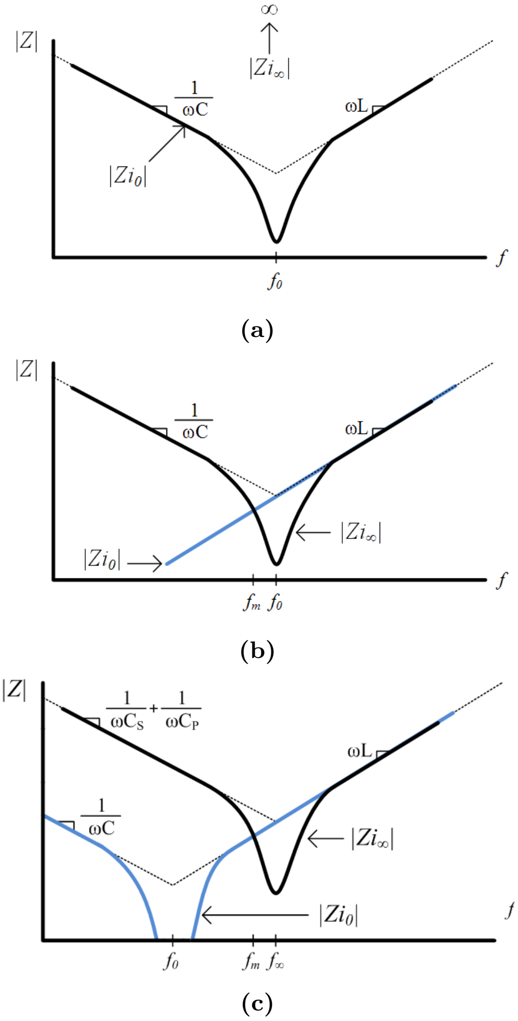

Figure 1.6: Bode plot of the input impedance $|Z_i|$ of: (a) SRC, (b) PRC and (c) LCC.

f_m. In such case, accomplishment of ZVS and ZCS has to be analyzed for specific load and resonant tank design.

Similarly, the complexity of the response obtained in 3rd or higher order converters requires to study the Bode plot of the input impedance in order to discern at which frequencies ZVS or ZCS are obtained. In the case of the LCC, three different regions can be identified. The first one is for frequencies below f_0, which defines the resonant frequency for short-circuited load. In this region ZCS is always accomplished. In the second region, above the resonant frequency for an open-circuit load f_∞, ZVS is always accomplished. In the region between f_0 and

f_∞, both ZVS and ZCS can occur depending on the load and resonant tank design. Further details of ZVS and ZCS accomplishment in the LCC resonant converter can be found in [21, Chapter 18].

Throughout this work, the different resonant tank structures depicted in Fig. 1.3 will be analyzed. For clarification, Table 1.1 presents their input-output transfer functions, whereas Table 1.2 presents their input impedance transfer functions.

Table 1.1: Input-output transfer functions of the SRC, PRC, LCC, LLC and LCLC

Converter	$\lvert H(s)\rvert$
SRC	$\frac{RC_s s}{LC_s s^2+RC_s s+1}$
PRC	$\frac{1}{LC_p s^2+\frac{L}{R}s+1}$
LCC	$\frac{RC_s s}{LRC_s C_p s^3+LC_s s^2+R(C_s+C_p)s+1}$
LLC	$\frac{L_p R C_s s^2}{L_p L_s C_s s^3+RC_s(L_s+L_p)s^2+L_p s+R}$
$LCLC$	$\frac{L_p R C_s s^2}{L_p L_s C_p C_s R s^4+L_p L_s C_s s^3+R(L_s C_s+L_p C_p+L_p C_s)s^2+L_p s+R}$

Table 1.2: Input impedance transfer functions of the SRC, PRC, LCC, LLC and LCLC

Converter	$\lvert Zi(s)\rvert$
SRC	$\frac{LC_s s^2+RC_s s+1}{C_s s}$
PRC	$\frac{LRC_p s^2+Ls+R}{RC_p s+1}$
LCC	$\frac{LRC_p C_s s^3+LC_s s^2+R(C_p+C_s)s+1}{C_s(RC_p s+1)s}$
LLC	$\frac{L_p L_s C_s s^3+RC_s(L_s+L_p)s^2+L_p s+R}{C_s(R+L_p s)s}$
$LCLC$	$\frac{L_p L_s C_p C_s R s^4+L_p L_s C_s s^3+R(L_s C_s+L_p C_p+L_p C_s)s^2+L_p s+R}{C_s(L_p C_p R s^2+L_p s+R)s}$

1.2 Motivation and goals

Due to the complexity of the large signal analysis of resonant converters, previous works have focused mainly on the description of different resonant structures and their characteristics, on the modeling of the converter dynamics based on the fundamental harmonic approximation (FHA) [22–26] or on the study of different resonant structures and the determination of its advantages and disadvantages [27, 28]. In the FHA, the resonant tank is assumed to respond only to the fundamental component of the input voltage $v_s(t)$, as shown in Fig. 1.7.

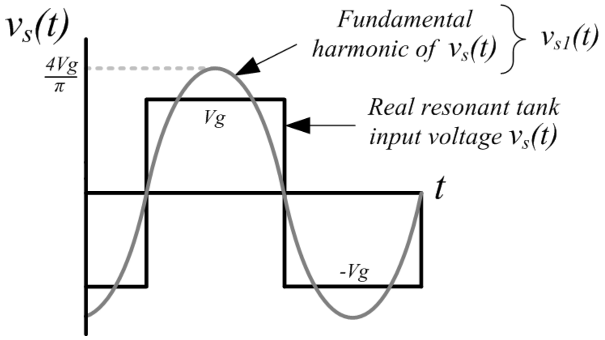

Figure 1.7: Waveforms at the input of the resonant tank in a full-bridge topology.

Previous approaches typically employ frequency modulation for regulation purposes [29–31], such that switches are driven by a controller and a voltage controlled oscillator (VCO) that generates the switching pattern. A general small-signal modeling technique for frequency modulated resonant converters was introduced by Robert W. Erickson in [21,32]. This modeling approach, which is based on the aforementioned FHA, links the envelope of the AC signal with the changes in the switching frequency, describing with exactitude the behavior of frequency modulated resonant converters. This approach is considered to be the conventional modeling and control technique of resonant power converters.

However, resonant converters can also be driven by the oscillating signals generated by the converter itself. Such an approach is known as self-oscillating control of resonant converters [33–35]. In contrast with VCO-based converters, self-oscillating converters do not require any additional oscillator to operate.

Self-oscillating resonant converters are becoming increasingly popular among designers due to their inherent control advantages: they allow a much closer operation to the resonant frequency than conventional frequency-controlled converters while preserving zero-voltage switching, and present very simple realizations.

In spite of the simplicity of the control mechanism, the mathematical description of the self-oscillating mode is relatively complex as it is proved by a number of works reported in the last years. Some of these works have based their procedures on the application of the same FHA principles [36–38]. However, there exist different literature that explains the behavior of these converters by using the describing function [39], by applying frequency-domain analysis based on the use of Hamel locus [35] or by employing state-plane analysis [40, 41] for obtaining the trajectory described by the limit cycle [42–48].

Specifically, the describing function has been used in [39] to predict the steady-state behavior of the converter by separating the system in two parts, i.e. the resonant stage and a non-linear block made up of the input bridge and the non-linear controller. Later, a closed-loop frequency-domain analysis with a relay and the use of the Hamel locus has been presented in [35] to determine the mode of oscillation for a given value of the relay hysteresis width in a LCLC converter. The notion of band-pass signal [49] has been used in [42] under the form of a time-varying phasor describing a sinusoid whose frequency and phase change with time. A large-signal phasor-transform model for a LCC converter has been derived and later linearized assuming self-oscillation, and its information has been employed by a FPGA to appropriately determine the changes of polarity of the series-inductor current. It has been also shown that the power factor control in self-oscillating mode could be combined with an additional control loop to obtain output voltage regulation. The start-up of a series resonant converter using an ON-OFF control based on the changes of polarity of either the inductor current or a linear combination of inductor current and capacitor voltage has been justified in [43] by the increase of the stored energy during the transient state and verified by means of simulation. The previous idea is the basis for the two-loop control of the series resonant converter reported in [44]. There, an internal loop implements an ON-OFF control based on the changes of polarity of a linear combination of the inductor current and its reference, which, in turn, is provided by an outer loop made up of a PI compensator processing the output voltage error. A similar approach is found in [45] in which an external loop establishes the constants of the mentioned linear combination that constitutes the inner loop.

The basic problem underlying the inherent self-oscillating behavior in all the mentioned works is to find the parametric conditions for the existence of the resulting limit cycle together with an accurate prediction of its amplitude and period. In all the previous literature, the analysis has been made for ad-hoc applications, so that a common framework for different situations does not exist. This is due to the fact that the existing reports tackle the problem by assuming first the existence of limit cycle and then establishing both amplitude and frequency of the oscillation by means of the describing function approach [13, 39, 50], by means of generalizations of this technique like the Hamel locus cited before [35] or by using alternative techniques such as Tsypkin's method [12]. Moreover, it is also necessary to ensure the stability of the mechanism generating the self-oscillation, which has not been disclosed so far. Also, in those works where closed-loop control has been used to change the operating point of the self-oscillation, regulation has been achieved without any dynamic model [45, 47].

This work is motivated by the need of a general approach describing the behavior of self-oscillating resonant converters of different order that can be used to systematically find the parametric conditions for the existence of a limit cycle of known amplitude and frequency. In addition, this thesis investigates a small-signal dynamic model that links the effects of self-oscillating control on the switching frequency of the resonant converters with the purpose of voltage amplitude regulation.

The resulting general framework will provide a simple procedure for designing robust and cost-efficient self-oscillating converters, facilitating its inclusion in future commercial solutions where the use of resonant conversion is of interest, such as induction heating [51], LED [52–54] or fluorescent [55–57] lightning solutions, charge of electric [58–60], hybrid [61] or fuel-cell vehicles [62] or wireless charging [63, 64].

1.3 Objectives

The main objectives of this thesis are:

- Define general restrictions to ensure the generation of self-oscillation and its stability.
- Describe a new general procedure to find parametric conditions that result in self-oscillations of known amplitude and frequency.
- Provide a novel FHA-based dynamic model of self-oscillating resonant converters, allowing the synthesis of controllers with tight performances.
- Demonstrate the benefits of self-oscillation in view of its potential industrial applications.

The thesis is organized as follows: Chapter 2 provides the fundamental principles in the operation of self-oscillating resonant converters. In Chapter 3 a general procedure for analyzing the behavior of 2nd order resonant converters under self-oscillation is presented and the value of the restriction to accomplish in such structures is established. In that chapter, simple steps for the design of a 2nd order self-oscillating converter of defined amplitude and period are provided. The resulting procedure is then applied in the design of a practical application based on a self-oscillating PRC. Chapter 4 presents a new model for self-oscillating converters based on FHA and introduces static and dynamic models for 2nd order structures. The resulting model is applied in the design of an output voltage controller for a PRC and its performance is compared with the performance of standard FM controllers designed under similar conditions. An extension to 3rd order resonant converters of the analytical procedure presented in Chapter 3 is covered exhaustively in Chapter 5, with special emphasis in the stability study. As in Chapter 3, the resulting design procedure is applied in the implementation of a practical application based on a LCC converter. Finally, in Chapter 6 the previous procedure is applied in 4th order structures with the aim of deriving simple design guidelines for such structures.

2

CHAPTER 2

PRINCIPLES OF SELF-OSCILLATING RESONANT POWER CONVERTERS

THIS chapter develops the framework that defines the behavior and operation of a self-oscillating resonant converter. The generation of the self-oscillating response is based on the change of sign of a single state-variable or on the change of sign of a combination of state-variables.

Throughout the chapter, the advantages and disadvantages of this approach and also general design rules for obtaining a self-oscillating resonant converter are presented.

2.1 Theoretical framework

As said in Chapter 1, a common framework for the analysis, modeling and control of self-oscillating resonant converters does not exist in the literature. In most cases, previous works have been focused on the study of different switching laws that improve the response or controllability of a desired variable in ad-hoc applications. In those cases, control laws are set-up empirically without previous modeling [45, 47].

The approach presented here gives a simple design guideline, resulting in stable and robust self-oscillating resonant converters.

In this chapter, the self-oscillating converter is described as a variable structure system (VSS) [65], controlled by a function that depends on a single state-variable or on a combination of different state-variables. A specific condition, typically based on the analysis of the change of sign of the selected variable, generates a change in the structure of the system by varying the polarity of the voltage at the input of the resonant tank. If the resonant tank is designed with a low damping ratio ξ, this variation leads to a behavior where the variable under observation changes its sign again, modifying the structure of the system. This repetitive behavior results in a growing output voltage and current entering into a limit cycle and producing a self-oscillating resonant pattern.

It is worth noting that the behavior of self-oscillating converters has no relation with sliding-mode regimes. For clarification of the operation principle, an example made with the parallel resonant converter is depicted below. The power stage of a parallel resonant converter (PRC) and its equivalent circuit based on the first-harmonic approximation are shown in Figs. 2.1a and 2.1b respectively.

In this circuit a small damping ratio $\left(\xi = \frac{\sqrt{LC}}{2R_{eq}C} = \frac{1}{2Q}\right)$ can be obtained if the Q factor $\left(Q = \omega_0 R_{eq} C = \frac{R_{eq}}{\sqrt{\frac{L}{C}}}\right)$ is sufficiently large, this value being directly related to the gain of the resonant tank $\left(H(s) = 1/\left(\frac{s^2}{\omega_0^2} + \frac{s}{Q\omega_0} + 1\right)\right)$ at the resonant frequency.

Fig. 2.2 shows the behavior of the current and voltage in a PRC circuit with low damping ratio and unchanging structure. The response of the circuit for the structure where $S_1 - S_4$ are activated and $S_2 - S_3$ deactivated $(u = 1)$ can be seen in the blue line, whereas the opposite configuration $(u = 0)$ is shown in red. It can be seen that when the input voltage of the resonant tank is positive, the current changes its sign from positive to negative several times before arriving to a steady-state value defined by V_g/R_{eq}. Similarly, when the input voltage is negative, the current oscillates many times before reaching its steady-state value $-V_g/R_{eq}$. Thus, there exist two different focus and a variable that intrinsically

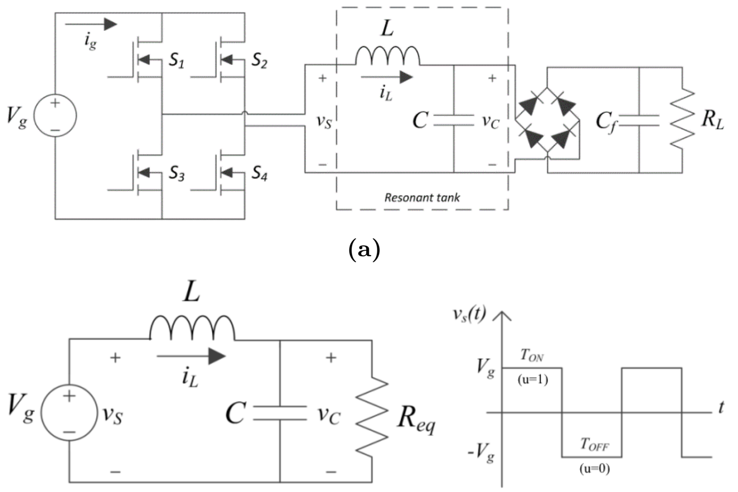

(a)

(b)

Figure 2.1: (a) Power stage of a parallel resonant converter. (b) Equivalent circuit based on the first harmonic approach.

changes its sign. Throughout this thesis, it is assumed that the variation of the structure is conditioned to the existence of these focuses.

If the system changes its structure in agreement with, for example, the change of sign of the current through the inductor $i_L(t)$, it is possible to obtain stable oscillations at the output of the resonant tank produced by the resulting change

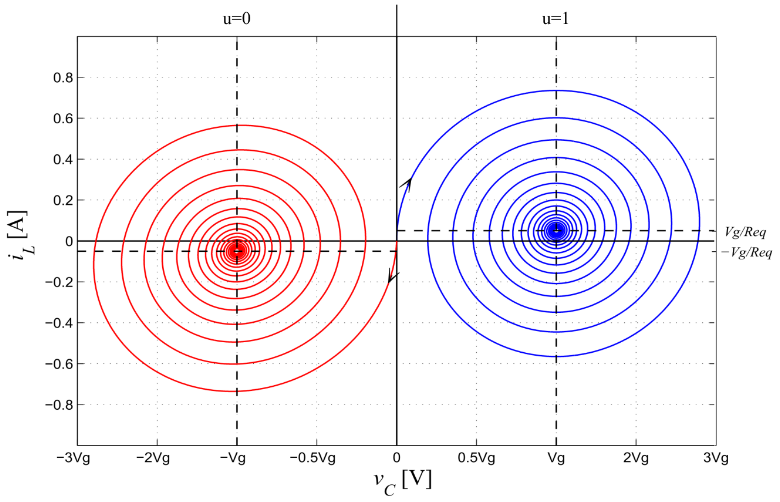

Figure 2.2: PRC phase-plane trajectory assuming constant input voltage: $v_s = V_g$ for $u = 1$, $v_s = -V_g$ for $u = 0$.

of polarity of the tank input voltage $v_S(t)$. In such case, the generation of the limit cycle is synthesized by composing the portions of the resulting oscillation generated between the focus of each structure, producing a growing spiral that eventually becomes an ellipse. The structure control law is stated as $u = sg(i_L)$, where u is the control variable and function $sg(i_L)$ is defined as:

$$sg(i_L) := \begin{cases} 1, & i_L \geq 0 \\ 0, & i_L < 0 \end{cases} \tag{2.1}$$

Fig. 2.3 depicts the response of the PRC under changes of the structure defined by the previous control law. Network topology T_{on}, or equivalently, $u = 1$ ($S_1 - S_4 \Rightarrow ON$ and $S_2 - S_3 \Rightarrow OFF$) holds for $i_L \geq 0$ while network topology T_{off}, or equivalently $u = 0$ ($S_2 - S_3 \Rightarrow ON$ and $S_1 - S_4 \Rightarrow OFF$) holds for $i_L < 0$. It can be seen that, with that behavior, current and voltage grow and arrive to a steady-state amplitude when limit cycle is reached.

In general, any resonant system can auto-start and self-oscillate if the structure of the circuit changes with the sign of a state-variable with a defined focus provided that the system is sufficiently underdamped. These restrictions represent a general necessary rule for obtaining a self-oscillating behavior but not sufficient for assuring the stability of the response. In the case of 2nd order converters, self-oscillation only depends on the design of the resonant tank and the load, as the damping ratio is directly related with the input-output transfer function $H(s)$. Nevertheless, in 3rd and higher order structures additional conditions are required for assuring the self-oscillation. These additional conditions are defined in the upcoming chapters.

Although there exist different eligible state-variables and combinations for having self-oscillation, this work focuses on the use of the sign of the current through the inductor [43] as the basic rule. Fig. 2.4 depicts the operation principle under this control rule. It can be seen that the polarity at the input of the resonant tank changes when the current crosses zero, as a result of the change of structure generated by the switch of the active MOSFET's. In consequence, the sign of the current $i_L(t)$ is equal to the sign of the voltage $v_S(t)$.

Therefore, the resulting circuit presents naturally a behavior of loss-free resistor [66, 67], as the fundamental-harmonic of the input voltage and the input current at the resonant tank are always in phase. Due to that, a unitary power factor and a loss-free resistor behavior are obtained in steady-state in the connection between the input port and the load, which makes it particularly suitable for high-frequency high-efficiency and low EMI applications [68]. In addition, this general approach allows to obtain a resonant converter designed for a defined switching frequency and gain and with inherent auto-startup without the requirement of inserting any additional circuitry. It is simple to implement, as only a current

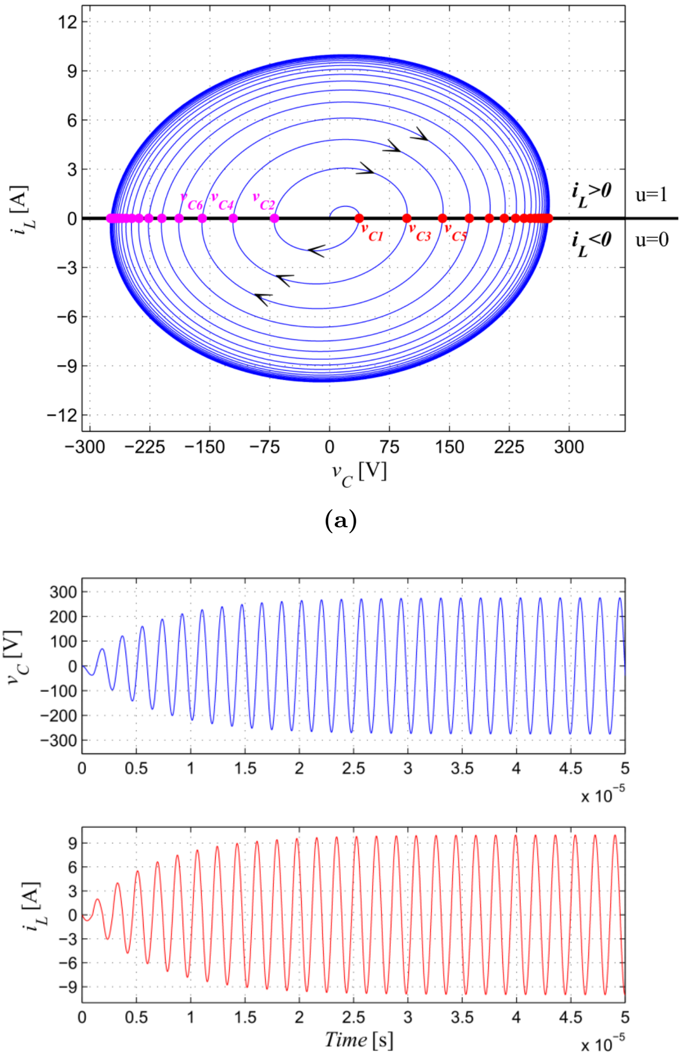

(b)

Figure 2.3: Response of a VSS PRC controlled by $u = sg(i_L)$: (a) Phase-plane trajectory, (b) Time-domain response.

sensor and a comparator are required. Besides, this control method represents a robust solution for fixed load applications, as the system will operate by its own nature at a fixed operation point during all its life-time. Note, however, that with this approach it is not possible to control the voltage at the output. It can be seen that any load variation produces automatically a gain variation and a new voltage and power level at the output.

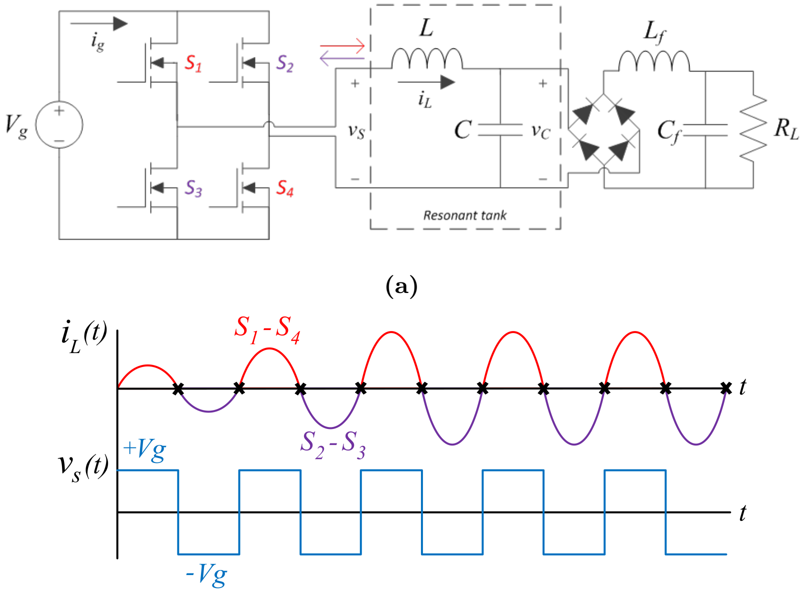

(a)

(b)

Figure 2.4: Operation under VSS approach with $u = sg(i_L)$: (a) Circuit scheme, (b) Switching pattern diagram (x-marks: switching instants).

2.2 Voltage control switching law

In order to regulate the output voltage, a modification of the switching law is required. As an example, the switching instant can be a function of the sign of the current and the amplitude of the output voltage. Under that situation, the system changes its structure some instants before or after the current zero-crossing, varying the switching frequency as a result.

In a second order system, a linear combination of the state-variables i_L and v_C, or their normalized forms j_L and m_C, can be employed to generate the switching instants of the resonant converter. In [46], the switching instants occur when $|s_1 j_L + s_2 m_C| = V_{\text{const}}$ holds, being s_1, s_2 and V_{const} constants.

Equivalently, this new class of VSS-based controller can also be expressed as

$$u = \text{sg}(j_L - k\ m_C). \tag{2.2}$$

This form, which appeared previously in [43–45], has the advantage that it has a straightforward representation in the state-plane and, more importantly, that the value of parameter k is directly related to the angle between $v_{s1}(t)$ and $j_L(t)$.

It is worth to remark that a normalization of the variables is applied in order to analyze the effect of each state-variable weighted in comparison with a common base value, resulting in equally weighted quantities and giving a circular limit cycle in all cases. If normalization is not done, then k is no longer related to the angle between the current and the voltage. In second order systems, such as the SRC and PRC, the normalization is as follows:

$$m_C = \frac{v_C}{V_g} \tag{2.3}$$

$$j_L = \frac{R_0}{V_g} i_L \tag{2.4}$$

where $R_0 = \sqrt{\frac{L}{C}}$ and where V_g is the power source voltage.

In order to clarify the operation principle, Fig. 2.5 shows the behavior of the system under the previous simple switching law based only on the sign of the current $(u = sg(j_L))$ while Fig. 2.6 represents the behavior under the new switching law resulting from the combination of j_L and m_C $(u = \mathrm{sg}(j_L - k\ m_C))$. In this figure, it can be seen that the angle between $m_C(t)$ and $j_L(t)$ is equal to α and that the slope of the switching boundary is $k = \tan(\alpha)$. Hence, from Fig. 2.5c, when $k > 0$ (positive α) the converter operates above the resonant frequency and when $k < 0$ (negative α) it operates below resonance. In other words, variable switching instants controlled by the angle α, or reciprocally its slope k, are introduced, which makes possible to regulate the output voltage by varying the angle as a function of the desired controlled parameter.

An analytic expression of α given by the input impedance phase can be derived in the PRC as follows, with $Q = \omega_0 R_{eq} C = R_{eq}/R_0$ and damping ratio $\xi = \frac{1}{2Q}$:

$$\begin{aligned}
\alpha =& \angle Z_i(s)\big|_{s=j\omega_{\mathrm{sw}}} = \angle\left(-\frac{\left(j\frac{\omega_{\mathrm{sw}}}{\omega_{\mathrm{o}}}\right)^2 + j\frac{\omega_{\mathrm{sw}}}{Q\omega_{\mathrm{o}}} + 1}{jC\omega_{\mathrm{sw}} + \frac{1}{R_{eq}}}\right) = \\
=& \angle\left(-\frac{\left(j\frac{\omega_{\mathrm{sw}}}{\omega_{\mathrm{o}}}\right)^2 + j\frac{\omega_{\mathrm{sw}}}{Q\omega_{\mathrm{o}}} + 1}{jC\omega_{\mathrm{sw}} + \frac{1}{R_{eq}}}\right)\left(\frac{\frac{1}{R_{eq}} - jC\omega_{\mathrm{sw}}}{\frac{1}{R_{eq}} - jC\omega_{\mathrm{sw}}}\right) \\
&= \angle\left(\left(\frac{\omega_{\mathrm{o}}}{Q} - j\omega_{\mathrm{sw}}\right)\left(-\left(j\frac{\omega_{\mathrm{sw}}}{Q\omega_{\mathrm{o}}} + \left(1 - \left(\frac{\omega_{\mathrm{sw}}}{\omega_{\mathrm{o}}}\right)^2\right)\right)\right)\right) = \\
=& \arctan\left(-Q\frac{\omega_{\mathrm{sw}}}{\omega_{\mathrm{o}}}\left(1 - \frac{1}{Q^2} - \left(\frac{\omega_{\mathrm{sw}}}{\omega_{\mathrm{o}}}\right)^2\right)\right).
\end{aligned} \tag{2.5}$$

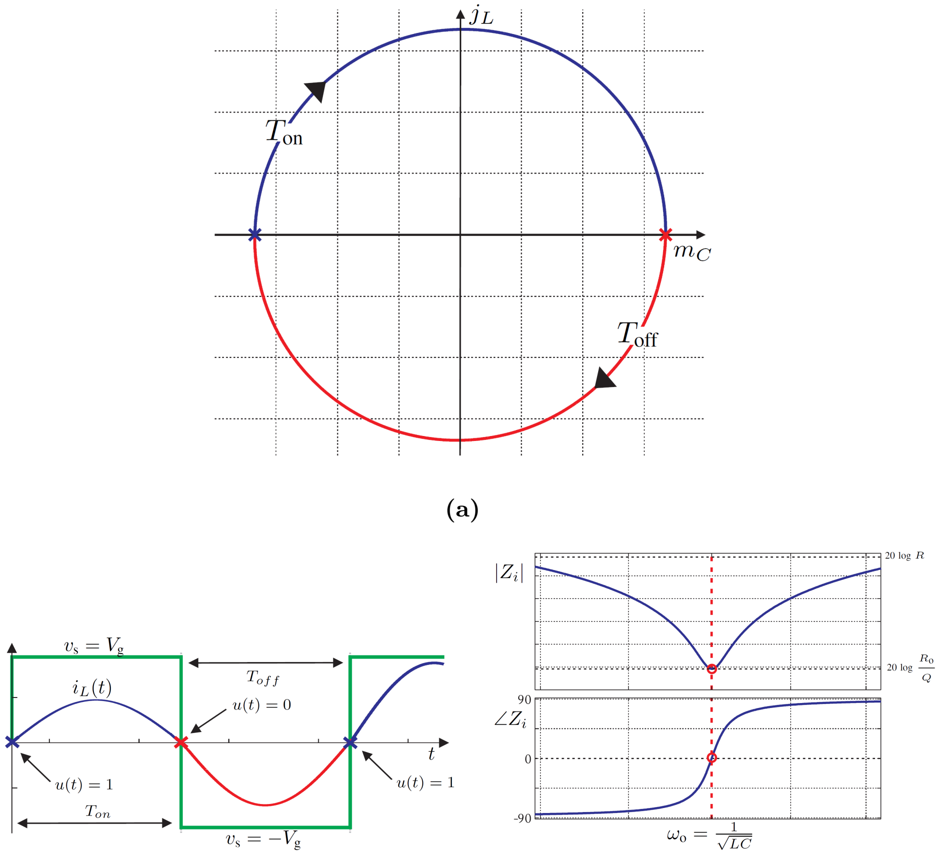

(a)

(b) **(c)**

Figure 2.5: Normalized response of the PRC controlled by $u = sg(j_L)$: (a) phase-plane trajectory (x-marks: switching instants), (b) time-domain waveforms, (c) Bode diagram of $Zi(s) = \frac{v_{S1}(s)}{j_L(s)}$.

This result allows to eliminate the tangent function in k, and to obtain an explicit relationship between the switching frequency ω_{sw} and k.

$$k = \tan(\alpha) = -Q\frac{\omega_{\text{sw}}}{\omega_{\text{o}}}\left(1 - \frac{1}{Q^2} - \left(\frac{\omega_{\text{sw}}}{\omega_{\text{o}}}\right)^2\right). \tag{2.6}$$

Similarly, the relationship between the switching frequency and k can be derived for the SRC, which results in

$$k = \tan(\alpha) = Q\left(\frac{\omega_{\text{sw}}}{\omega_{\text{o}}} - \frac{\omega_{\text{o}}}{\omega_{\text{sw}}}\right) \tag{2.7}$$

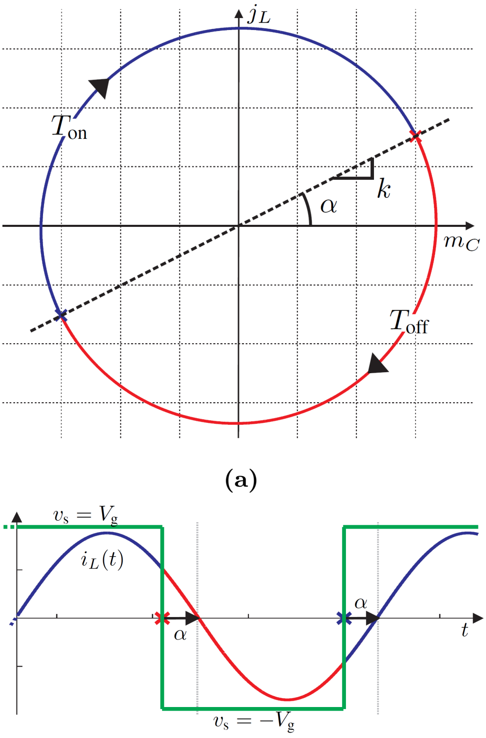

(b)

Figure 2.6: Normalized response of the PRC controlled by $u = sg(j_L - Km_C)$: (a) phase-plane trajectory (x-marks: switching instants), (b) time-domain waveforms.

In general, it is possible to obtain a direct relationship between the switching frequency ω_{sw} and k in other resonant structures by modifying the state-variables in the switching law.

If closed-loop regulation is required, $k(t)$ can be used to control the operation of the converter. In Fig. 2.7, a block diagram of this control law is illustrated. The normalized values of the inductor current and capacitor voltages can be obtained by means of operational amplifiers in case of a constant input voltage. Also a

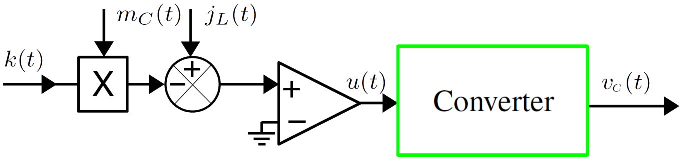

Figure 2.7: Block diagram of the new control based on $u = sg(j_L - k(t)m_C)$.

multiplier is required in order to carry out the multiplication between the state-variable $m_C(t)$ and the control variable $k(t)$.

2.3 Summary

General principles and restrictions for enabling self-oscillation in any resonant converter have been discussed in this chapter and different variable structure switching laws have been proposed. The first switching law is based on changing the polarity of the input voltage as a function of the sign of the current across the inductor, and allows the system to naturally self-oscillate at the resonant frequency. The output depends entirely on the parameters of the resonant tank and the load and therefore the amplitude of the output voltage is not regulated. The second switching law allows to regulate the phase angle between two state-variables while keeping self-oscillation, which results in variable switching frequency. Therefore, this parameter can be controlled in order to regulate the amplitude of the output voltage.

3

CHAPTER 3

SECOND ORDER RESONANT STRUCTURES: ANALYSIS, DESIGN AND APPLICATIONS

In this chapter an analytic procedure for describing the operation of 2nd order resonant structures is presented. The analysis is based on the change of structure as a result of a change of sign of the input inductor current, as defined in the previous chapter. The resulting second order differential equations are solved to construct a piecewise phase-plane trajectory which provides insight into the generation of a stable limit cycle and predicts its amplitude and period. Parametric conditions for the existence of self-oscillation are derived from the analysis, and its validity is verified by experimental results. Finally, a practical application is designed to illustrate the feasibility of the proposed approach in engineering.

3.1 Limit cycle generation

As in the previous chapter, the analysis that follows is exemplified with the PRC, although it can also be extended to the SRC. Fig. 3.3a depicts the power stage of a PRC, whereas Fig. 3.3b presents its equivalent circuit.

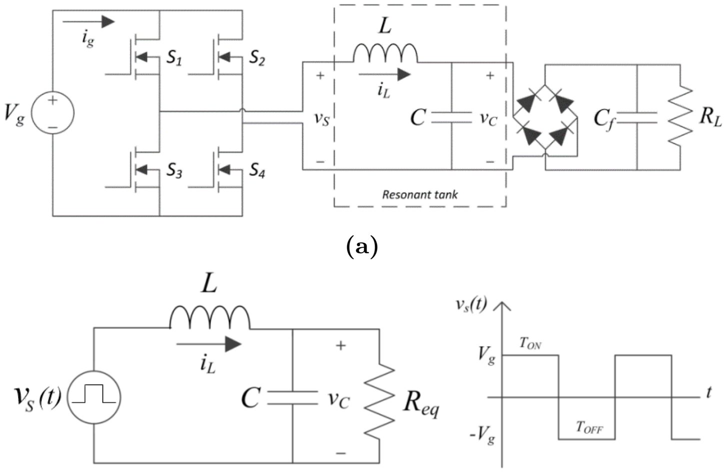

(a)

(b)

Figure 3.1: (a) Power stage of a parallel resonant converter. (b) Equivalent circuit based on the first harmonic approach.

A model based on the first harmonic approximation is used in the equivalent circuit of Fig. 3.3b to represent the effect of the rectifier and load by $R_{eq} = \frac{R_L \pi^2}{8}$ [21]. The differential equation relating input and output voltages is given by

$$\frac{d^2 v_C}{dt^2} + \frac{1}{CR_{eq}} \frac{dv_C}{dt} + \frac{v_C}{LC} = \frac{v_S(t)}{LC} \tag{3.1}$$

where $v_S(t) = V_g$ during T_{on} and $v_S(t) = -V_g$ during T_{off}. Assuming a damping factor ξ such that $0 < \xi < 1$, the solution of (3.1) in T_{on} interval for zero initial conditions [69, 70] can be expressed as follows

$$v_C(t) = e^{-\frac{t}{2R_{eq}C}} \left\{ -V_g \cos \omega_d t - \frac{V_g}{2R_{eq}C\omega_d} \sin \omega_d t \right\} + V_g \tag{3.2}$$

where $\omega_d = \omega_o \sqrt{1 - \xi^2}$, ω_o and ξ being respectively the natural oscillation frequency and the damping factor given by $\omega_o = \frac{1}{\sqrt{LC}}$ and $\xi = \frac{1}{2CR_{eq}\omega_0}$.

Current $i_L(t)$ in the same interval is given by

$$i_L(t) = C \frac{dv_C}{dt} + \frac{v_C}{R_{eq}} \tag{3.3}$$

From (3.2) and (3.3), we derive

$$i_L(t) = e^{-\frac{t}{2R_{eq}C}} \left\{ -\frac{V_g}{R_{eq}} \cos \omega_d t + \frac{1}{\omega_d} \left[\frac{V_g}{L} - \frac{V_g}{2{R_{eq}}^2 C} \right] \sin \omega_d t \right\} + \frac{V_g}{R_{eq}} \tag{3.4}$$

Similar expressions for $v_C(t)$ and $i_L(t)$ can be obtained for T_{off} interval by simply changing V_g by its opposite $-V_g$.

Assuming $v_S(t) = V_g \ \forall \ t$, this would result in a steady-state regime with coordinates $v_C^* = V_g$, $i_L^* = V_g/R_{eq}$, where superscript $(^*)$ denotes steady-state. Reciprocally, $v_S(t) = -V_g \ \forall \ t$ would lead to a symmetrical steady-state point $v_C^* = -V_g$, $i_L^* = -V_g/R_{eq}$, as previously illustrated in Fig. 2.2. Current $i_L(t)$ will cross the border $i_L = 0$ if a high quality factor Q is imposed,

$$Q_{PRC} = \omega_0 R_{eq} C = \frac{R_{eq}}{\sqrt{\frac{L}{C}}} = \frac{1}{2\xi}. \tag{3.5}$$

Then, as described in the previous chapter, it is possible to obtain stable oscillations at the output of the resonant tank by changing the input voltage as a function of the sign of the inductor current i_L. A simulation of a PRC circuit switching under that condition is shown in Fig. 3.2, illustrating the generation of the limit cycle. This example presents a Q value of 14.5.

Similarly, a limit cycle can be obtained in the SRC by applying the same

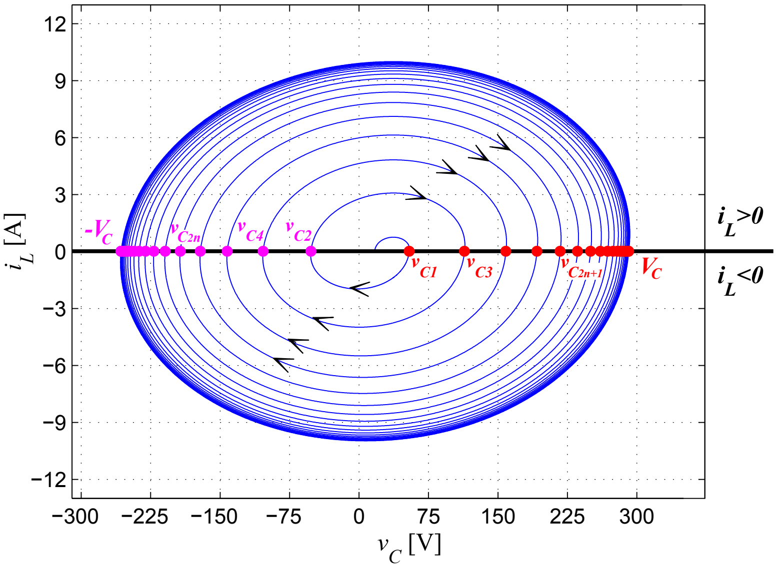

Figure 3.2: VSS made up of the two substructures of the PRC with $C = 10.5$ nF, $L = 8\,\mu$H, $R_{eq} = 400\ \Omega$, $V_g = 20$ V.

control law. Also, in this case a system with a high quality factor Q is required. The value of Q is defined as

$$Q_{SRC} = \frac{R_0}{R_{eq}} = \frac{\sqrt{\frac{L}{C}}}{R_{eq}} \tag{3.6}$$

Thus, an underdamped system can be obtained by selecting sufficiently heavy load. An example for the configuration of Fig. 3.3 is proposed. The design presents an inductor value of 9.1 μH and a capacitor value of 5.68 nF with an output load of $R_{eq} = 5\,\Omega$ and an input voltage of 12 V, leading to a Q_{SRC} value of 8. The limit cycle obtained by numerical simulation is depicted in Fig. 3.4a, showing that the system self-oscillates and arrives to a limit cycle as expected.

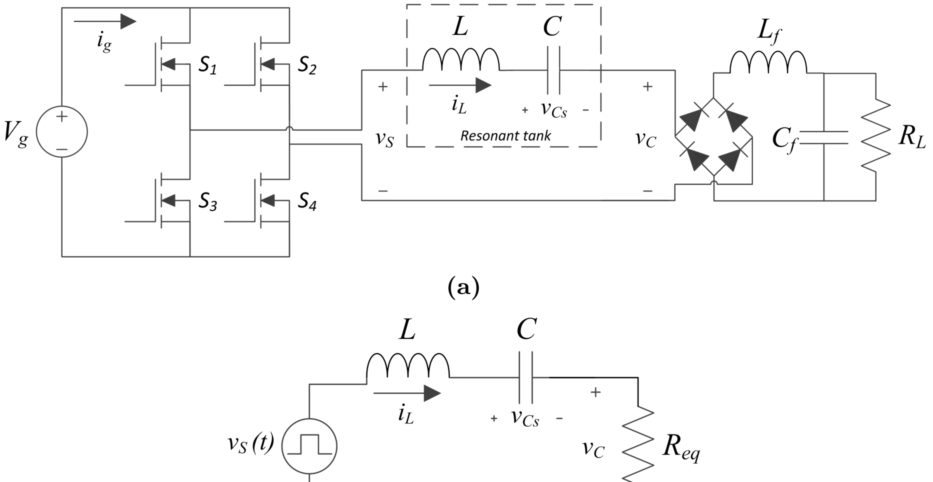

(a)

(b)

Figure 3.3: (a) Power stage of a series resonant converter. (b) Equivalent circuit based on the first harmonic approach.

It is also worth to remark that the input-output transfer function $H(s)$ of a SRC circuit operating at the resonant frequency ω_0 presents always a value of 1, as demonstrated in Equation (3.7). As a result, in self-oscillation the output voltage equals the first harmonic of the resonant tank input voltage. Time-domain waveforms of the previous simulation, depicted in Fig. 3.4b, illustrate this case.

$$\begin{aligned} H(j\omega_0) &= \frac{R_{eq}Cj\omega_0}{-LC\omega_0^2 + R_{eq}Cj\omega_0 + 1} = \\ &= \frac{R_{eq}Cj\omega_0}{-LC\frac{1}{LC} + R_{eq}Cj\omega_0 + 1} = 1 \end{aligned} \tag{3.7}$$

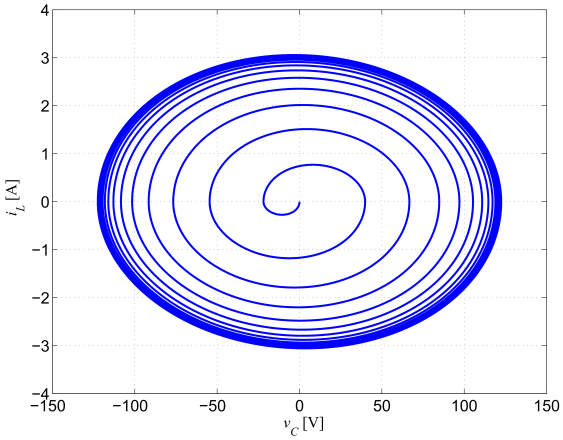

(a)

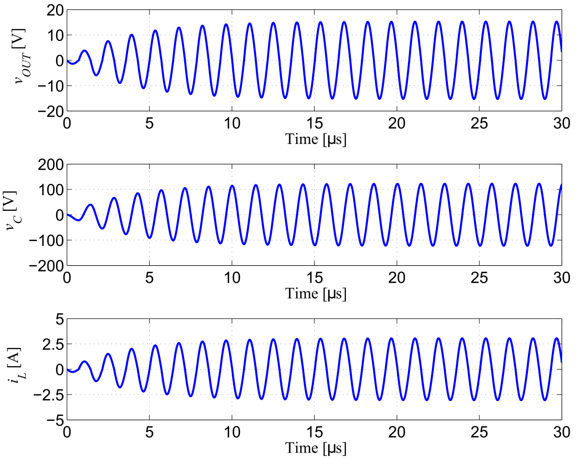

(b)

Figure 3.4: Response of a VSS SRC controlled by $u = sg(i_L)$: (a) Phase-plane trajectory, (b) Time-domain response. $L = 9.1\,\mu$H, $C_s = 5.68$ nF, $R_{eq} = 5\ \Omega$, $V_g = 12$ V.

3.2 Determination of amplitude and period in the limit cycle

Equation (3.2) is now modified to describe the behavior of $v_C(t)$ in the PRC for network topology T_{on} during a generic interval $t_2 < t < t_3$ and initial conditions $v_C(t_2) = -\, v_{C_{2n}}$ and $i_L(t_2) = 0$, and with $\tau = t - t_2$.

$$v_C(\tau) = e^{-\frac{\tau}{2R_{eq}C}} \left\{ (-v_{C_{2n}} - V_g)\cos\omega_d\tau - \frac{(-v_{C_{2n}} + V_g)}{2R_{eq}C\omega_d}\sin\omega_d\tau \right\} + V_g \qquad (3.8)$$

As seen in Fig. 3.2, variable $v_{C_{2n}}$ symbolizes the voltage amplitude at switching instants from negative to positive current value while $v_{C_{2n+1}}$ symbolizes the opposite situation, with n increasing after a complete cycle. Therefore, the voltage at the negative to positive switching instants is described by $[v_{C2}, v_{C4}, v_{C6}, ..., v_{C_{2n}}$, ..., $-V_C]$, whereas the opposite situation is described by $[v_{C1}, v_{C3}, v_{C5}$, ..., $v_{C_{2n+1}}$, ..., $V_C]$. Note than when in capital letters, this notation refers specifically to the value at the limit cycle or, equivalently, in steady-state (e.g.: V_C), whereas in lowercase letters it refers to any generic switching instant (e.g.: $v_{C_{2n}}$).

Expression (3.8) has its maximum value v_{CM} at instant τ_c given by

$$\omega_d\tau_c = \tan^{-1}\left(-\frac{2\xi\sqrt{1-\xi^2}v_{C_{2n}}}{V_g + v_{C_{2n}}(1-2\xi^2)} \right) + \pi \qquad (3.9)$$

$$v_{CM} = e^{-\xi\omega_0\tau_c}\sqrt{V_g^2 + {v_{C_{2n}}}^2 + 2V_g v_{C_{2n}}(1-2\xi^2)} + V_g \qquad (3.10)$$

Under conditions of high Q, it is apparent that $\xi << 1$, or equivalently, $1 - 2\xi^2 \approx 1$ and $\omega_d \approx \omega_o$, so that expressions (3.9) and (3.10) become

$$\omega_0\tau_c \approx \tan^{-1}\left(-\frac{2\xi v_{C_{2n}}}{V_g + v_{C_{2n}}} \right) + \pi \qquad (3.11)$$

$$v_{CM} = e^{-\xi\omega_0\tau_c}(V_g + v_{C_{2n}}) + V_g \qquad (3.12)$$

If the generic interval $t_2 < t < t_3$ corresponds to any T_{on} interval of the growing spiral, then the maximum value v_{CM} is $v_{C_{2n}}$ (see Fig. 3.2), as it corresponds to the switching instant. Hence, it can be defined that

$$v_{C_{2n}} = e^{-\xi\omega_0\tau_c}\left(V_g + v_{C_{2n-1}}\right) + V_g \qquad (3.13)$$

Besides, in the limit cycle, the ratio $\frac{2\xi v_{C_{2n}}}{V_g+v_{C_{2n}}}$ can be approximated by 2ξ, and therefore expression (3.11) becomes

$$\omega_0\tau_c \approx \tan^{-1}(-2\xi)+\pi \approx -2\xi+\pi \approx \pi \tag{3.14}$$

Introducing (3.14) in (3.13) yields

$$V_C = V_g\frac{1+e^{-\xi\pi}}{1-e^{-\xi\pi}} \approx \frac{2V_g}{\pi\xi} \tag{3.15}$$

which is exactly the maximum value of the capacitor voltage in steady-state at resonant frequency considering the first harmonic approximation

$$V_{CM,FHA} = \frac{4}{\pi}V_gQ = \frac{2V_g}{\pi\xi} \tag{3.16}$$

Moreover, from (3.14), the period of the limit cycle will be given by

$$T = 2\tau_c = \frac{2\pi}{\omega_0} \tag{3.17}$$

which is the period that corresponds to the resonant frequency of the converter.

3.3 Establishment of restrictions for self-oscillation

A point of interest for the self-oscillation of resonant converters is to establish a minimum Q such that the system enters into the limit cycle. In the PRC, when the switching boundary is as defined previously $i_L(t)=0$, this is equivalent to finding whether the current trajectory crosses the zero axis for some $t>0$ if $i_L(0)=0$. For an initial capacitor voltage $v_C(0)=-v_{C_{2n}}$, the current trajectory shown in (3.4) can be rewritten as follows

$$i_L(\theta) = e^{-\frac{\theta}{2R_{eq}C\omega_d}}\left\{-\frac{V_g}{R_{eq}}\cos\theta+\frac{1}{\omega_d}\left[\frac{V_g+v_{C_{2n}}}{L}-\frac{V_g}{2{R_{eq}}^2C}\right]\sin\theta\right\}+\frac{V_g}{R_{eq}} \tag{3.18}$$

where the angle $\theta=\omega_d t$ is adopted for convenience. It can be shown that $v_{C_{2n}}=0$ corresponds to the worst case for which the switching boundary may not be crossed if Q is not sufficiently large.

Assuming $e^{-\frac{\theta}{2R_{eq}C\omega_d}} \approx 1$, the first term of the trajectory

$$\frac{V_g}{R_{eq}}-\frac{V_g}{R_{eq}}\cos\theta \tag{3.19}$$

is always positive, whereas the second term

$$\frac{1}{\omega_d}\left[\frac{V_g+v_{C_{2n}}}{L}-\frac{V_g}{2R_{eq}^2C}\right]\sin\theta \tag{3.20}$$

can be rewritten as

$$\left[(V_g+v_{C_{2n}})\frac{1}{R_0\sqrt{1-\xi^2}}-V_g\frac{\xi}{QR_0\sqrt{1-\xi^2}}\right]\sin\theta \tag{3.21}$$

with $R_0=\sqrt{\frac{L}{C}}$.

It can be seen that $\frac{1}{R_0\sqrt{1-\xi^2}} \geq \frac{\xi}{QR_0\sqrt{1-\xi^2}}$ if $\xi \leq 1 \leftrightarrow Q \geq 0.5$, which was already assumed for an underdamped response. Thus, the second term is negative at $\theta=\frac{3\pi}{2}$, being more negative with increasing values of $v_{C_{2n}}$. As a consequence, a minimum value of Q is required in order to ensure reaching the switching boundary in the worst case, which occurs during start-up given that the current presents its lowest value.

Fig. 3.5 shows the start-up trajectory of the current for different values of Q. It can be observed that, for a large Q, the switching boundary is reached at an angle approximately equal to π, the difference between the switching angle θ and π being equal to $\beta=\theta-\pi$.

Linearization of trajectory (3.4) with a first-order Taylor approximation at angle π allows solving the equation for the switching instant β. This first-order Taylor approximation of the damped sinusoidal terms in (3.4) can be expressed as

$$e^{-\frac{\theta}{2R_{eq}C\omega_d}}\cos\theta \approx e^{-\frac{\pi}{2R_{eq}C\omega_d}}\left(\frac{\beta}{2R_{eq}C\omega_d}-1\right) \tag{3.22}$$

$$e^{-\frac{\theta}{2R_{eq}C\omega_d}}\sin\theta \approx -\beta e^{-\frac{\pi}{2R_{eq}C\omega_d}} \tag{3.23}$$

and then, the switching angle can be derived as

$$\beta=\frac{L\omega_d}{R_{eq}}\left(1+e^{-\frac{\pi}{2R_{eq}C\omega_d}}\right) \tag{3.24}$$

This approximation remains valid only for sufficiently small values of β. If a rather arbitrary upper bound of β is chosen, e.g. $\beta={}^{\pi}/_{4}$, the switching angle will then satisfy

$$\frac{L\omega_d}{R_{eq}}\left(1+e^{-\frac{\pi}{2R_{eq}C\omega_d}}\right) \leq \frac{\pi}{4} \tag{3.25}$$

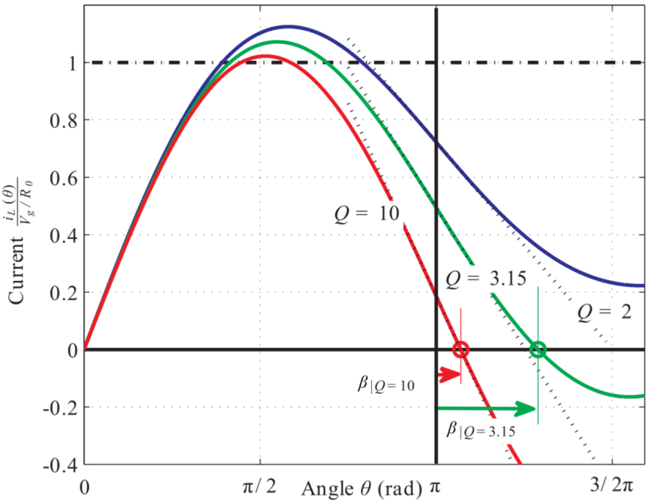

Figure 3.5: Current trajectory of a parallel resonant converter during startup with $i_L(0) = 0$, $v_C = 0$ for three different quality factors $Q = [2, 3.15, 10]$. Steady state current V_g/R (dash-dotted), linearization of the trajectory at $\theta = \pi$ (dotted) and crossing of the switching boundary $i_L(t) = 0$ (circles).

whose exponential term can be linearized to yield

$$\frac{L\omega_d}{R_{eq}}\left(1 + 1 - \frac{\pi}{2R_{eq}C\omega_d}\right) \leq \frac{\pi}{4} \tag{3.26}$$

Since $L > 0$ and $C > 0$, this expression can be simplified to obtain an inequality that depends solely on Q

$$\pi\left(Q^2 - 2\right) - 4\sqrt{4Q^2 - 1} \geq 0 \tag{3.27}$$

which can be reduced to $Q \geq 3.15$.

This result, while approximated, represents a valid and restrictive calculation of the lower bound for Q. Equal or larger values of Q guarantee the self-oscillation and allow the converter to reach the limit cycle described in the previous sections.

3.4 Stability analysis

Proving the stability of limit cycles in power converters often requires a dedicated involved analysis leading sometimes to general analytic results [71] or to a mixture of analytical and numerical demonstrations [72]. In this work a different approach based on the analysis of the exact behavior obtained in Section 3.2 is proposed. As the system is defined by a growing spiral that becomes an ellipse in the limit cycle, it is possible to describe a recurrence between the switching points of the phase-plane, which can be analyzed for the assessment of stability.

From (3.13) and (3.14), it can be found that

$$v_{C_{2n}} = -V_g \left(1 + \frac{V_g + v_{C_{2n-1}}}{V_g} e^{-\xi\pi}\right) \tag{3.28}$$

where n=[1, 2, 3, . . .]

If $v_{C_{2n}}$ is the last negative-to-positive boundary crossing, the next switch will happen at $v_{C_{2n+1}}$, which can be defined by the increase of the spiral as:

$$\begin{aligned} v_{C_{2n+1}} &= V_g \left[1 + \frac{V_g - v_{C_{2n}}}{V_g} e^{-\xi\pi}\right] = \\ &= V_g + \left(V_g - v_{C_{2n}}\right) e^{-\xi\pi} = \\ &= V_g + \left(V_g + V_g \left(1 + \frac{V_g + v_{C_{2n-1}}}{V_g} e^{-\xi\pi}\right)\right) e^{-\xi\pi} = \\ &= V_g + V_g e^{-\xi\pi} + V_g e^{-\xi\pi} + V_g e^{-2\xi\pi} + v_{C_{2n-1}} e^{-2\xi\pi} \end{aligned} \tag{3.29}$$

leading to

$$v_{C_{2n+1}} = V_g(1 + 2e^{-\xi\pi} + e^{-2\xi\pi}) + v_{C_{2n-1}} e^{-2\xi\pi} \tag{3.30}$$

The previous expression can be simplified as follows

$$v_{C_{2n+1}} = V_g\left(1 + e^{-\xi\pi}\right)^2 + v_{C_{2n-1}} e^{-2\xi\pi} \tag{3.31}$$

where ξ is the damping factor defined by $\xi = \sqrt{LC}/(2CR_{eq})$ and $R_{eq} = R_L\pi^2/8$.

It can be observed that (3.31) describes a stable system since the term multiplying $v_{C_{2n-1}}$ is less than unity.

The evolution of the recurrence can be described as follows, defining $G = V_g\left(1 + e^{-\xi\pi}\right)^2$ and $r = e^{-2\xi\pi}$:

$$\begin{aligned}
n = 1 \longrightarrow v_{C3} &= G + v_{C1}r \\
n = 2 \longrightarrow v_{C5} &= G + Gr + v_{C1}r^2 \\
n = 3 \longrightarrow v_{C7} &= G + Gr + Gr^2 + v_{C1}r^3 \\
&. \\
&. \\
&. \\
n \longrightarrow v_{C_{2n+1}} &= G + Gr + Gr^2 + ... + Gr^{n-2} + v_{C1}r^{n-1} \\
&= G(1 + r + r^2 + ... + r^{n-2}) + v_{C1}r^{n-1}
\end{aligned} \tag{3.32}$$

and the stability of the recurrence can be proved by finding the limit of $v_{C_{2n+1}}$ when n tends to ∞

$$\lim_{n\to\infty} v_{C_{2n+1}} \underset{\substack{\uparrow \\ \lim\limits_{n\to\infty} v_{C1}r^{n-1} \underset{\substack{\uparrow \\ r<1}}{=} 0}}{=} \frac{G}{1-r} = \frac{V_g(1+e^{-\xi\pi})^2}{1-e^{-2\xi\pi}} = \frac{V_g(1+e^{-\xi\pi})}{1-e^{-\xi\pi}} \tag{3.33}$$

leading to the same result shown in (3.15).

Fig. 3.6 verifies by simulation the previous theoretical prediction for initial conditions situated at each possible quadrant of the phase-plane. It can be seen that all the trajectories reach the limit cycle irrespective of the their initial conditions.

3.5 Simulation results

In order to validate the previous analysis, a simulation of the PRC with the converter parameters of Table 3.1 and the switching law based on the sign of the inductor current is made.

Table 3.1: Set of parameters of the VSS PRC simulation

Parameter	**Value**
V_g	20 V
L	8 μH
C_p	10.5 nF
R_{eq}	400 Ω

Applying (3.16) and (3.17) it is possible to predict the amplitude and the frequency of the simulated output voltage in steady-state, which can be compared with the simulation results in order to verify its validity:

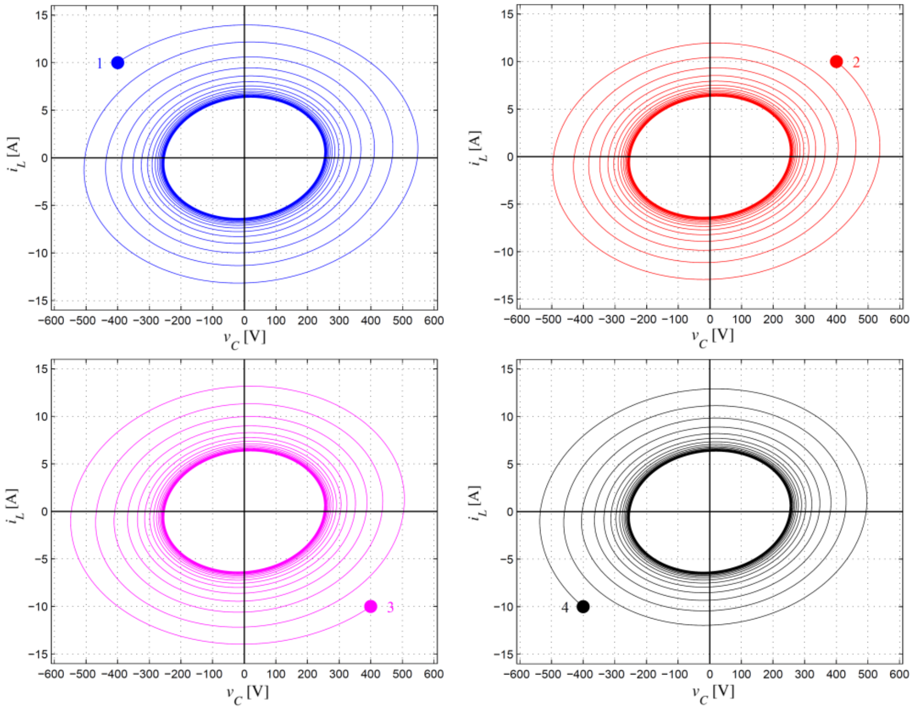

Figure 3.6: Trajectories reaching the limit cycle from different initial conditions: (1) second quadrant (2) first quadrant (3) fourth quadrant (4) third quadrant.

$$Q_{PRC} = \frac{R_{eq}}{\sqrt{\frac{L}{C_p}}} = 14.5 \tag{3.34}$$

$$\xi = \frac{\sqrt{(LC)}}{2C_pR_{eq}} = \frac{1}{2Q} = 0.035 \tag{3.35}$$

$$V_{CM,FHA} = \frac{2V_g}{\pi\xi} = 370\,V \tag{3.36}$$

$$f_{sw} = \frac{1}{T} = \frac{\omega_0}{2\pi} = \frac{\frac{1}{\sqrt{LC_p}}}{2\pi} = 550\,kHz \tag{3.37}$$

Simulation results depicted in Fig 3.7a confirm the generation of the limit cycle in the phase-plane while Fig 3.7b shows the waveforms in time-domain. The results gathered in this figure exhibit a peak output voltage of 369 V and a switching frequency of 549 kHz, verifying the validity of the previous calculations.

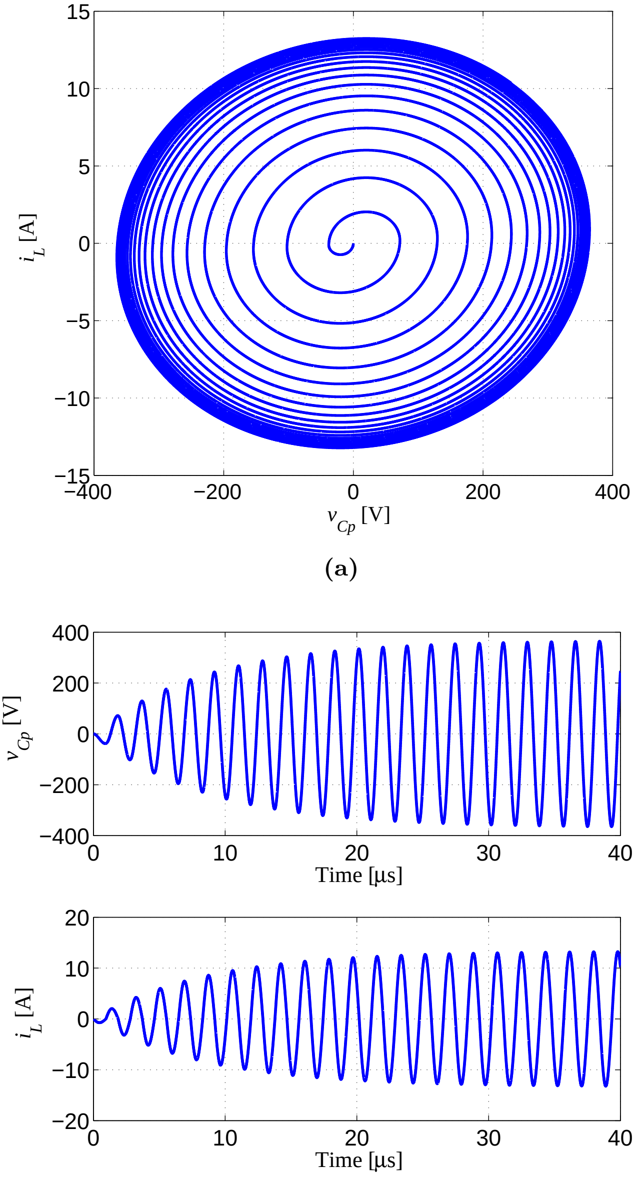

(a)

(b)

Figure 3.7: Response of a self-oscillating VSS PRC with a load of $R_{eq} = 400\Omega$: (a) limit cycle generation, (b) waveforms of v_{Cp} and i_L.

With the aim of verifying the minimum Q boundary of 3.15, a corresponding load ($R_{eq} = 87\,\Omega$) is introduced in the simulation. The results are shown in Fig. 3.8. It can be seen that the system is able to auto-start and self-oscillate with an output peak voltage of 77 V. Lower values of Q preclude the self-oscillation. As an example, the response for a Q value of 2.5 (or equivalently, a load of $R_{eq} = 65\,\Omega$) is depicted in Fig. 3.9. It can be seen that the current does not cross zero at startup since the system is not sufficiently underdamped. As a result, the structure of the converter does not switch, being unable to self-oscillate.

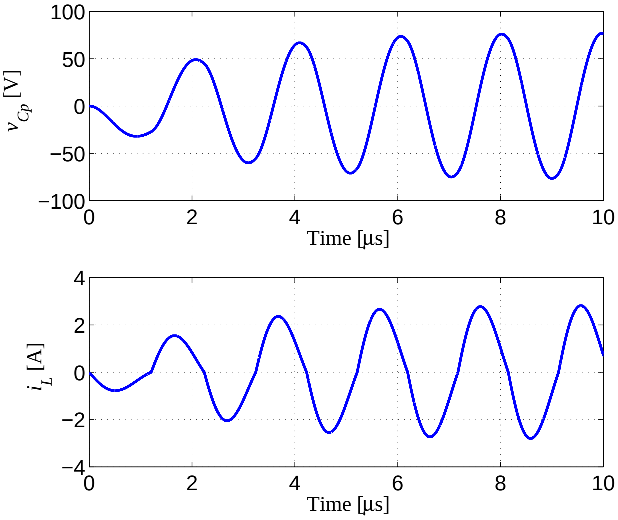

Figure 3.8: Output voltage v_{Cp} and resonant tank input current i_L of a self-oscillating VSS PRC with a load of $R_{eq} = 87\,\Omega$ and a Q value of 3.15.

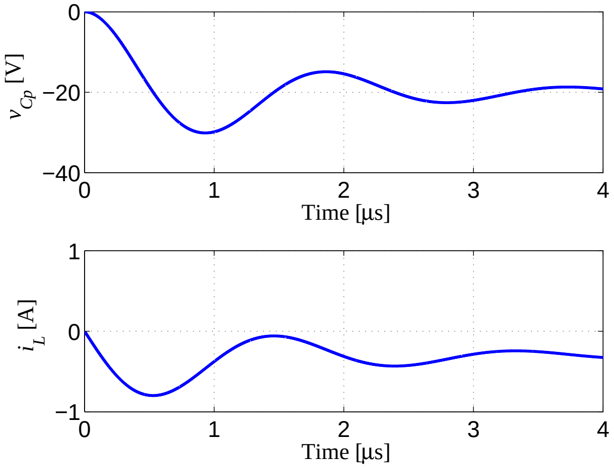

Figure 3.9: Output voltage v_{Cp} and resonant tank input current i_L of a self-oscillating VSS PRC with a load of $R_{eq} = 65\,\Omega$ and a Q value of 2.5.

3.6 Limitation on the implementation: the propagation delay

One of the main limitations that arises in the experimental realization of a self-oscillating resonant converter comes from the inherent propagation delays in the circuit. In the previous section, an ideal circuit without any propagation delay has been simulated, demonstrating the effectiveness of the proposed design. However, components such as gate drivers present a propagation delay shifting the effective switching instant. As a result, they generate a phase-shift between the voltage and the current at the input of the resonant tank, so that the voltage is lagged with respect to the current. In turn, the switching frequency is reduced. The higher the delay, the lower the oscillating frequency is.

With the aim of illustrating the impact of delays in a real implementation, a PRC prototype is designed with the parameters of Table 3.2. Fig. 3.10 shows the circuit scheme of both power stage and VSS controller. The power stage is made up of an H-bridge circuit and a resonant tank. The H-bridge employs 4 MOSFETs, which are activated by a driver stage based on the IC ADUM7234. The resonant tank has been built with a ceramic (C0G) capacitor of 10.7 nF and an air-gap-based AC inductor of 7.3 μH, this implying a Q value of 11.5 for a resonant frequency of 570 kHz and an equivalent load resistance of $R = 300\,\Omega$. The VSS controller employs a LT1116 comparator to establish the change of polarity of the input voltage in agreement with the zero-crossings of the inductor current, which is measured by a current sense transformer (CST) with a transformer ratio 1:8. The output signal of the comparator activates a circuit adding a dead time to avoid short-circuits during transitions. This stage, which is composed by two logic gates, is then connected to the driver circuitry described above. The experimental prototype can be seen in Fig. 3.11.

Fig. 3.12 shows steady-state waveforms of the PRC in self-oscillating mode. The corresponding experimental generation of the limit cycle is illustrated in Fig. 3.13. The results obtained verify, as expected, that the phase-shift between current and voltage is not 90° and that the phase displacement between the inductor current and the first harmonic of the input voltage is not 0° either. The resulting frequency mismatch is of 23 kHz, mainly caused by the existence of a 176 ns delay in the activation of the MOSFET switches with respect to the current zero-crossing. Fig. 3.14 illustrates this fact. The overall delay obtained is the result of the response of the comparator, logic gates and driver stage, which introduce 13 ns, 37 ns and 126 ns respectively.

In conclusion, for guaranteeing an operation of the converter under the expected conditions it is required to select components with very small propagation delay ratios or to introduce a delay compensation network that switches the structure at a defined time before the current crosses zero. The next section shows a practical application of second order resonant converters and explores different compensation networks that mitigate the effects of propagation delays.

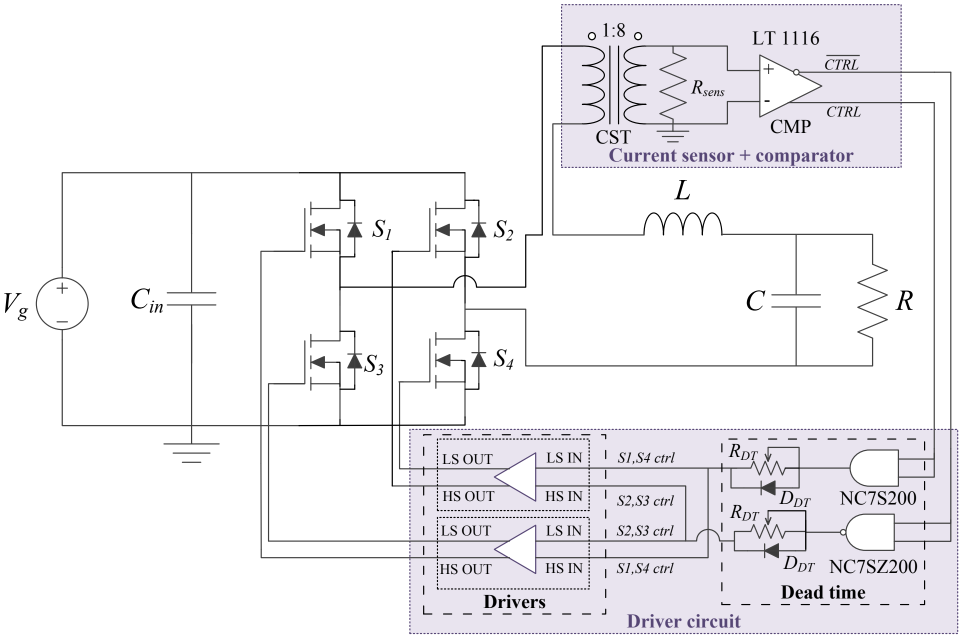

Figure 3.10: Circuit scheme of the parallel resonant converter with the proposed VSS-based controller.

Table 3.2: Set of parameters of the VSS PRC prototype

Parameter	Component	Value
V_g	-	12 V
C_{in}	X7R	11 μF
S_{1-4}	IPB200N15NS3	-
L	Air-core inductor	7.3 μH
C	C0G/NP0	10.7 nF
R	Resistor	300 Ω
CST	Transformer	1:8
R_{sens}	SMD Resistor	5 Ω
R_{DT}	Potentiometer	$<$ 500 Ω
D_{DT}	SDM03U40	-
$Driver$	ADuM7234	-
Q	-	11.5
f_0	-	570 kHz

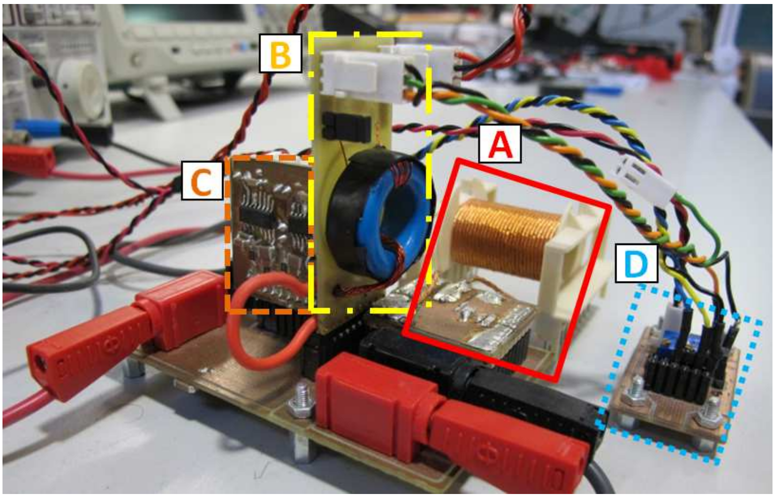

Figure 3.11: Image of the experimental prototype: (a) resonant tank, (b) current sensor and comparator, (c) driver and (d) dead time circuit.

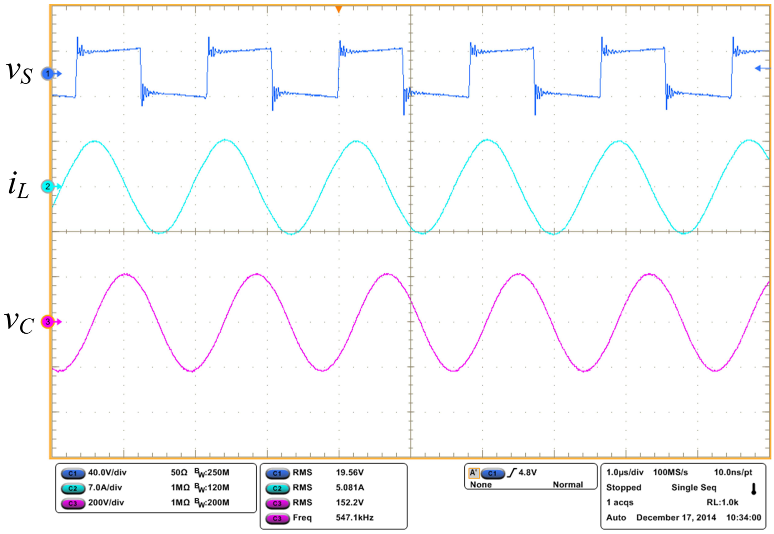

Figure 3.12: Experimental waveforms of the PRC in self-oscillation.

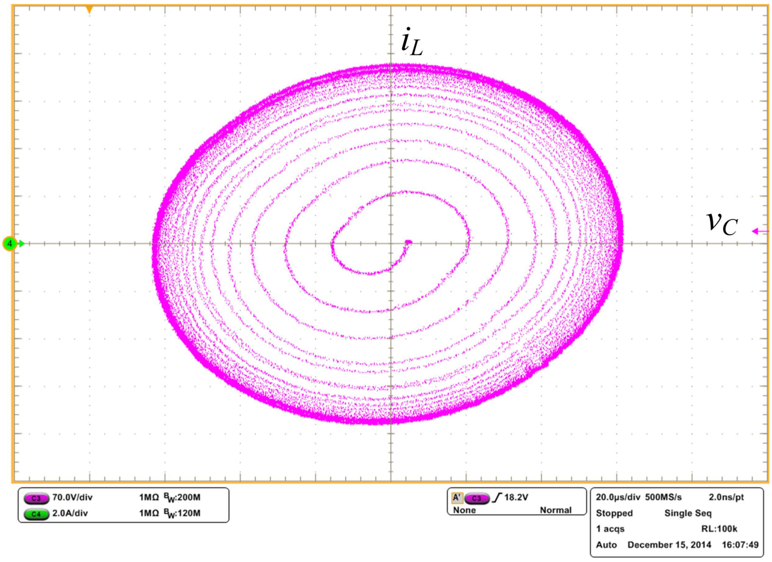

Figure 3.13: Experimental limit cycle generation of the PRC in self-oscillation.

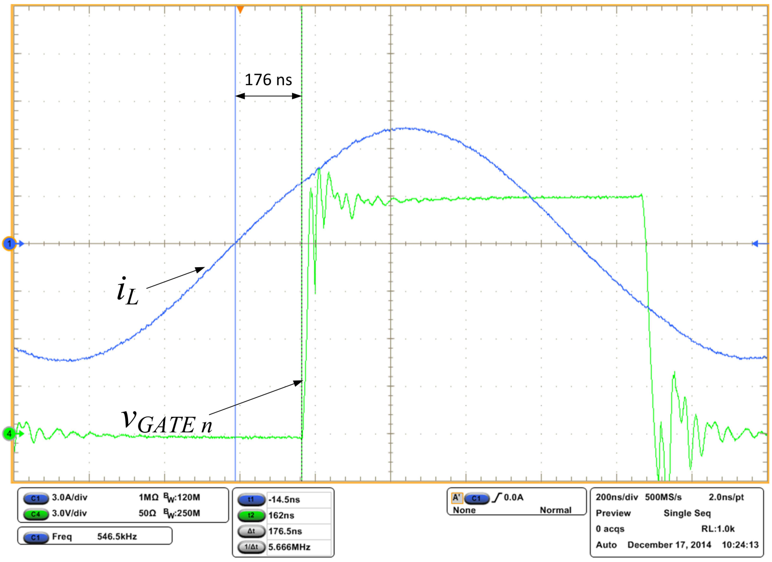

Figure 3.14: Delay between inductor current zero-crossing and activation of the MOSFETs.

3.7 Application: 6.78 MHz GaN FET PRC designed for Wireless Power Transfer

Resonant converters represent the core of high-frequency wireless power transfer (WPT) systems, which offer easy-to-use single and multi-device charging for devices such as smartphones, tablets or small laptops [73, 74]. This application area has been gaining attention and various solution approaches have been addressed in a number of papers [74–82]. Challenges include maintaining soft switching and optimum power transfer in the presence of variations in coupling, resonant tank, and power level.

Due to the novelty of this field of study, no single standard has been established so far. Nevertheless, two main references can be used depending on the type of application: the Qi standard and the AirFuel Alliance standard [78].

Both are supported by major manufacturers and are arising as the reference standards for the design of compatible battery chargers. Despite of that, these standards are not compatible between them, as their specifications are very different.

At this moment a vast majority of new mobile phones complies with the Qi standard while AirFuel Alliance is being introduced in portable power-demanding devices such as phablets, tablets and laptops. This last standard defines a minor classification of the transmitting powers into different categories, the standard requirements being established only up to class 3. Therefore, in this section, the device designed will be a class 3 compliant transmitter. A list of the main characteristics of each standard and the specific restrictions imposed by class 3 is shown below.

Qi standard

- Frequency of operation: 110 kHz nominal (up to 205 kHz)
- Distance: 0-30 mm
- Power: 5 W
- Devices: 1 at a time

Airfuel Alliance standard

- Frequency of operation: 6.78 MHz ± 150 kHz
- Distance: 50 mm

- Power:
    - Class 2 = 10 W (smartphone, phablet)
    - Class 3 = 16 W (tablet)
    - Class 4 = 33 W (small laptop)
    - Class 5 = 50 W (regular laptop)
- Devices: Multiple devices at the same time

Airfuel Alliance Class 3 transmitter restrictions

- Maximum load resistance: 57 Ω
- Maximum AC mean output power: 16 W
- Minimum AC mean output power: 6.5 W
- Maximum AC output voltage (RMS): 38 V

While the specifications of this standard are not freely available to the general public, there exist literature that allows to establish its main design restrictions [20, 74–82]. Note that previous literature cites the AirFuel Alliance with its previous name, the ”Alliance for Wireless Power” or its acronym ”A4WP”.

3.7.1 Converter design

Fig. 3.15 shows the circuit diagram of the converter prototype: it is composed of a full-bridge resonant converter with a parallel resonant tank. The prototype can be configured as an inverter or it can also be configured as a rectifier in order to accomplish DC-DC conversion.

As indicated previously, the switching network will produce a square wave of subintervals T_{on} $(u = 1)$ and T_{off} $(u = 0)$ at the input of the resonant tank by sensing the sign of the current.

The AirFuel Alliance standard specifies an input voltage between 8 and 32 V and a maximum AC peak output power of 32 W for a load of 57 Ω [75]. In the design presented here, an input voltage of 12 V is assumed. An AC output voltage of 42 V peak, or equivalently, 30 V RMS is derived from the power and load values indicated before. The nominal switching frequency is equal to $f_{sw} = 6.78$ MHz, with a tolerance of ± 150 kHz, and the load applied is $R = 57\,\Omega$.

One of the advantages of the proposed self-oscillating design methodology is the simplicity of the steps to follow for obtaining the parameters of the resonant tank. Next, the design steps to obtain the values of the resonant tank components are summarized.

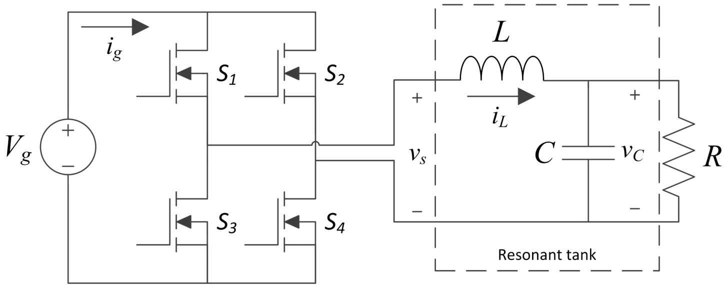

(a)

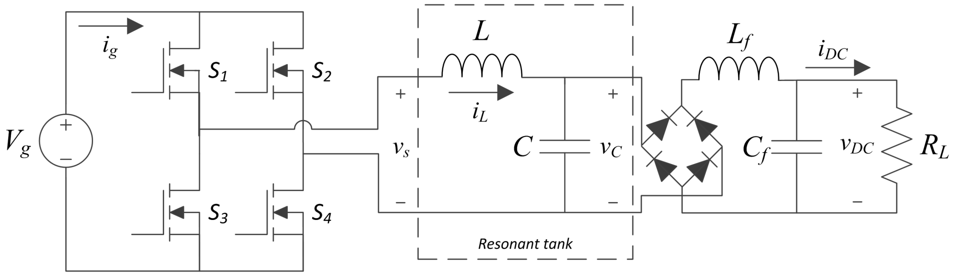

(b)

Figure 3.15: Circuit diagram of: (a) inverter PRC, (b) DC-DC PRC

Self-oscillating PRC resonant tank design steps

1. Define input and output voltage of the application.
2. Define the desired switching frequency ω_0 and the load R. Take into account that higher loads produce higher output power levels and lower loads produce lower output power levels.
3. Calculate Q ($Q|_{\omega_{sw}=\omega_0} = |H(j\omega_0)|$).
4. Evaluate if $Q \geq 3.15$ is accomplished. If not, the system will not be able to self-oscillate and the design has to be discarded.
5. Calculate the value of the capacitor with $C = \frac{Q}{\omega_0 R}$.
6. Calculate the value of the inductance with $L = \frac{1}{\omega_0{}^2 C}$.

A value of Q of 3.5 is obtained with the parameters previously selected, resulting in L and C values of 382 nH and 1.44 nF respectively. Note that the resonant tank parameters have been obtained for the inverter configuration with resistance R.

The following subsections briefly describe the design considerations related to current sensing and the full-bridge realization of the circuit using GaN devices.

3.7.1.1 Current sensor design

This application requires accurate current sensing, given that the generation of the switching pattern entirely depends on the sensed current waveform. The sensing stage requires sufficiently large bandwidth, high-speed, and noise rejection in order to reproduce the current signal at 6.78 MHz. Moreover, parasitics can affect the response of the sensor and may require compensation.

A classification of different sensing techniques, accounting for the fundamental frequency of the waveform, has been presented in [83, Table I]. Two main sensing techniques can be identified as suitable for high-frequency applications: (i) a current sensing transformer [84–86] or (ii) a series resistor sensed over a high-speed differential amplifier [83, 87, 88]. As presented in [85, 86] and [89], current sensing transformers require compensation of the parasitic effects generated between the windings by opposing the magnetic fields with a specific wiring design. In contrast, the shunt resistor sensor does not require any special procedure in order to operate at 6.78 MHz, and in consequence, this is the approach employed in this work. It is worth noting that the differential amplifier must exhibit appropriate gain, bandwidth and common-mode voltage rejection ratio. A high slew-rate THS4151 differential amplifier has been used in this case.

3.7.1.2 Full-bridge inverter design

Due to the high switching frequency and the power level desired for the considered application, switches presenting low gate charge and reduced recovery times are preferred.

Although the state-of-the-art Silicon FETs could reach the desired switching frequency, their parasitic effects would affect the generation of the self-oscillating signal and the overall efficiency. Therefore, GaN FETs (EPC8004, $R_{\mathrm{DS}_{(\mathrm{on})}} = 110\ \mathrm{m}\Omega$, $Q_{\mathrm{G}} = 370$ pC) have been used in this work, minimizing the parasitic effects that may affect the generation of the self-oscillating signal and the overall efficiency. Two LM5113 half-bridge drivers are used for the activation of the switches due to its high-performance characteristics.

3.7.1.3 Summary of selected components

Table 3.3 summarizes the selected components taking into account the restrictions denoted on the previous subsections.

Table 3.3: Summary of components selected in the design stage

Component	Code or Value
L $(Design)$	382 nH
C $(Design)$	1.44 nF
Differential Amplifier	THS4151
eGaN FET	EPC8004
Driver	LM5113

3.7.2 Delay Compensation Network

One of the main limitations of the proposed self-oscillating approach is due to the adverse effects of propagation delays over the synchronization between the sign of the tank input current and the polarity of the tank input voltage, as described in Section 3.6. With the present design, the overall propagation delay predicted is approximately 60 ns, which produces a reduction in the switching frequency of 40%. Hence, a delay compensation network is required in order to eliminate these effects and accomplish the standard requirements.

Two different compensation networks are proposed:

- A phase-leading RL circuit inserted at the input of the current-sensing differential amplifier.
- An adjustable hysteresis applied to the input of the current polarity comparator.

3.7.2.1 Phase-leading RL delay compensation network

This compensation network is based on an analog RL circuit that phase-shifts the voltage signal sensed by the shunt resistor R_{SENS}, as shown in Fig. 3.16. Phase-shift can be adjusted by changing the value of R_D as defined by Eq. (3.38), where τ is the value of delay to be compensated. The output of the sensor is then compared with zero so that the zero-crossings of the compensated waveform activate the corresponding switches.

$$\tau = \frac{L_D}{R_D} \tag{3.38}$$

Advantages of this solution are that it can process high bandwidth waveforms and that it remains invariable with respect to load changes. Nevertheless, this approach introduces losses and the compensation is sensitive to temperature variations and components tolerance. In addition, compensation can not be adjusted automatically, so the RL approach can be considered less practical compared to the hysteresis-based approach discussed next.

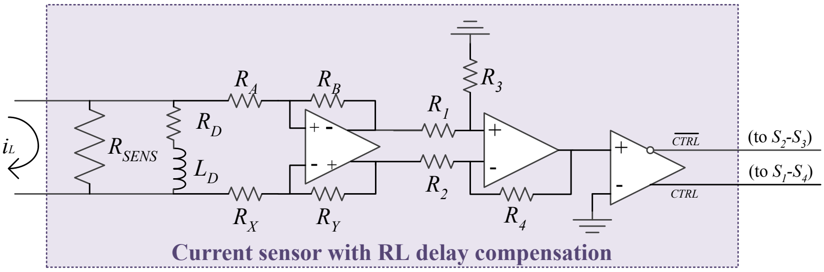

Figure 3.16: Phase-leading RL delay compensation network.

3.7.2.2 Hysteresis-Based delay compensation network

It is also possible to compensate the delay by changing the instant when the switching pattern is generated with an adjustable hysteresis function. This hysteresis allows the user to set a comparison value different than 0, enabling the system to switch at a defined time before the zero-crossing point of the current. As the system exhibits an approximately constant delay, compensation can be successfully achieved by setting a constant hysteresis value. In addition, the hysteresis value can be adjusted to obtain ZVS operation while maintaining the switching frequency very close to the resonant frequency.

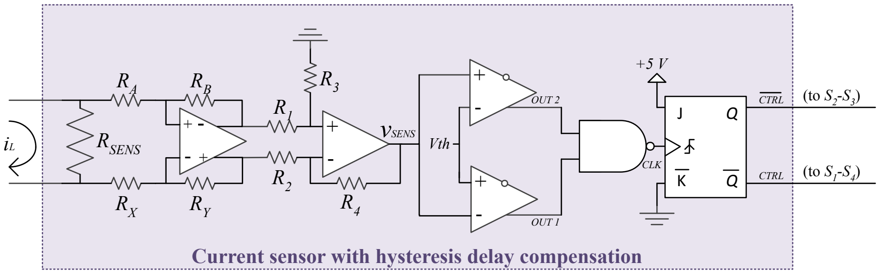

Figure 3.17: Hysteresis delay compensation network.

Fig. 3.17 depicts the block diagram of this compensation network. A rising-edge activated monostable is introduced in order to keep 50 % duty cycle, such that compensation is achieved equally during T_{on} and T_{off}. The comparators are in inverse configuration, such that there exists a period when both are activated, corresponding to the sensed current signal within $+V_{th}$ and $-V_{th}$. The outputs of the comparators are later combined with a NAND or an AND gate, which establishes the clock switching pattern of the monostable. The AND gate can be employed in case of delays below one half of the on/off periods, whereas the NAND gate must be provided in case of delays between one half and the entire period. In the proposed prototype, every on/off period lasts 80 ns, so that the reported delay of 60 ns requires the NAND gate. Fig. 3.18 illustrates the generation of the delay-compensated driving signal with the AND and the NAND gates. The range of operation of the two different circuits is highlighted.

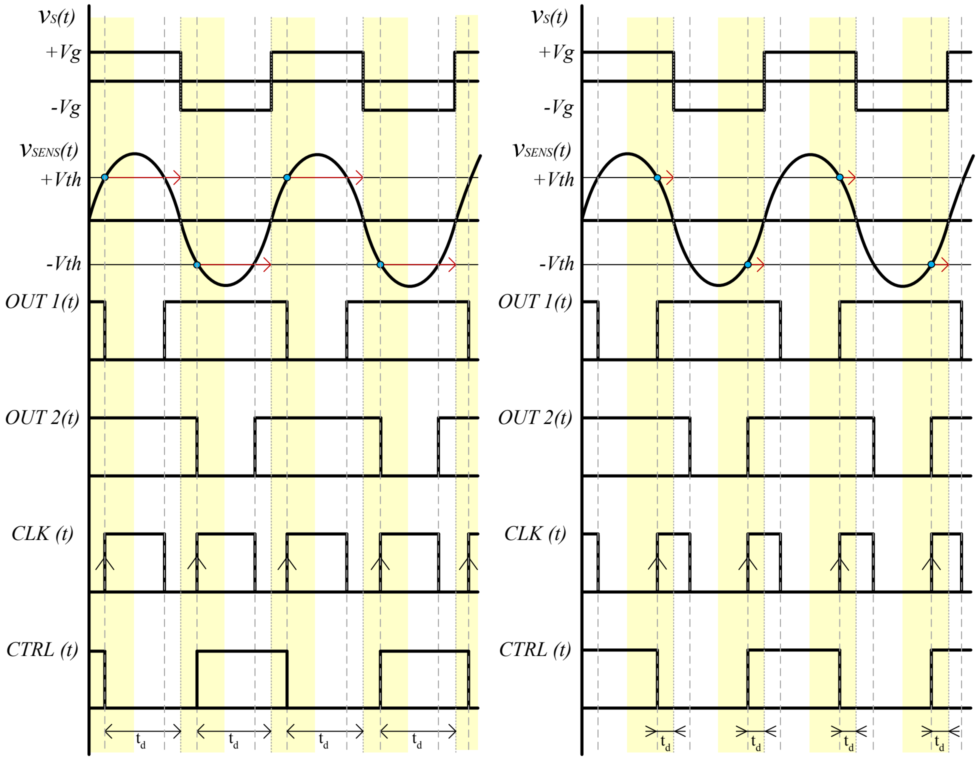

(a) **(b)**

Figure 3.18: Hysteresis-based compensation chronogram: (a) NAND gate, (b) AND gate.

The proposed hysteresis-based circuit has several merits, including low latency, accuracy and the capability of compensating delays longer than half of the switching cycle. However, the circuit also presents some limitations. First, the hysteresis compensation may inhibit the auto-startup of the self-oscillation. The initial trajectory of the input current may not present sufficient amplitude to intersect $+V_{th}/-V_{th}$ values, thus preventing the switching of the monostable and blocking the start-up of the power converter. The issue can be solved by introducing a startup-ramp behavior in the hysteresis level generator. The hysteresis is zero in initial conditions and increases up to the desired steady-state value with a sufficiently gentle slope. In order to maintain a simple implementation, this behavior has been realized with a *RC* low-pass filter. The scheme of the filter circuit is depicted in Fig. 3.19. A potentiometer has been introduced in order to regulate

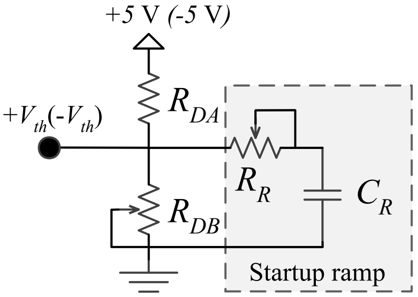

Figure 3.19: Lowpass filter of the hysteresis threshold enabling the self-oscillating start-up.

the ramp slope depending on the current level at the output.

In addition, although the propagation delay is constant, the effectiveness of the hysteresis compensator depends on the resonant frequency and the load. There are no frequency problems involved due to the fixed-frequency nature of the application, but load changes may modify the delay compensation associated to the nominal hysteresis level, given that the delay compensation depends on the current amplitude, and this constrains the operation of the compensation circuit to a limited range of loads. In this sense, it must be noted that heavier loads result in higher input currents, which for the same hysteresis level V_{th} correspond to larger compensations and higher switching frequencies. In the present case, if the maximum load ($R = 57\ \Omega$) is associated to the maximum switching frequency f_{sw} = 6.93 MHz (6.78 + 0.15 MHz), then the range of loads for which the standard is accomplished equals R=[37, 57] Ω.

It is worth to point out that the range of validity depends on the power level of the design and also on the required compensation. The limits are basically established by the length of the zone surrounding the hysteresis level, which depends on the slope of the approximately sinusoidal input current as illustrated in Fig. 3.20. It can be seen in the figure that for those levels in which the slope of the current can be considered linear, changes of current amplitude do not cause large changes in the switching frequency. Thus, the effects of this limitation may be potentially mitigated if the required delay values correspond to the region right before of after the zero crossings, where the influence of the current amplitude is minimal.

Regarding soft-switching, the hysteresis-based compensation network facilitates the accomplishment of ZVS if less than half semi-cycle is compensated (i.e., if the AND gate is used). Opposite to the behavior described above, lighter loads correspond, in this case, to higher switching frequencies, allowing the circuit to resonate closer to the inductive zone of the input impedance, and facilitating

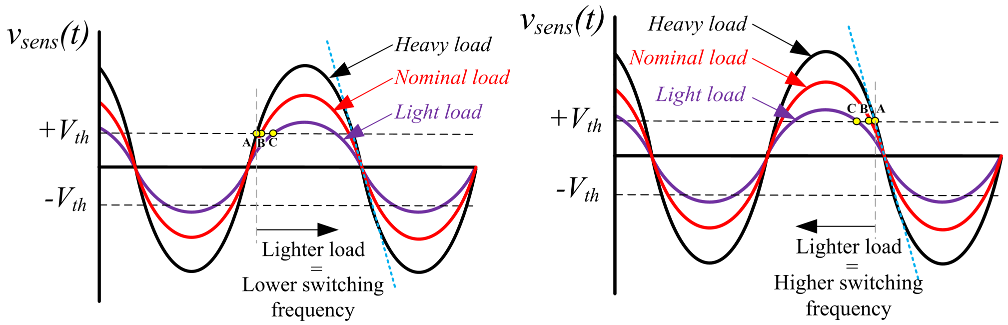

(a) with NAND gate **(b)** with AND gate

Figure 3.20: Effect of load variation over the hysteresis applied. Circles: Switching instants for different loads.

the discharge of the parasitic capacitances in the switches. The differences between the AND and the NAND gate circuits can be more intuitively identified in Fig. 3.20.

3.7.3 Simulation Results

In order to illustrate the operation of the circuit under the desired specifications, a LTSPICE simulation of the resonant converter with the designed hysteresis compensation network is made. V_{th} has been adjusted in the simulation to compensate the delay and a startup ramp of 2 μs has been established for enabling auto-startup.

Fig. 3.21 shows the startup and the steady-state waveforms of the input current, the input voltage and the hysteresis levels, confirming that the switching frequency with the selected delay compensation network is 6.78 MHz.

Although the hysteresis compensation network is more difficult to implement than the *RL* circuit, simulation results have shown that it is able to compensate the delay with lower error due to the independence of the compensation on the components tolerances. Results obtained at nominal load and frequency shows a difference of 4 ns between the two types of compensation, which implies a reduction of the delay of 93.3% in the RL compensation network and 98.3% in the hysteresis solution. As a result the hysteresis compensation network has been selected for this application.

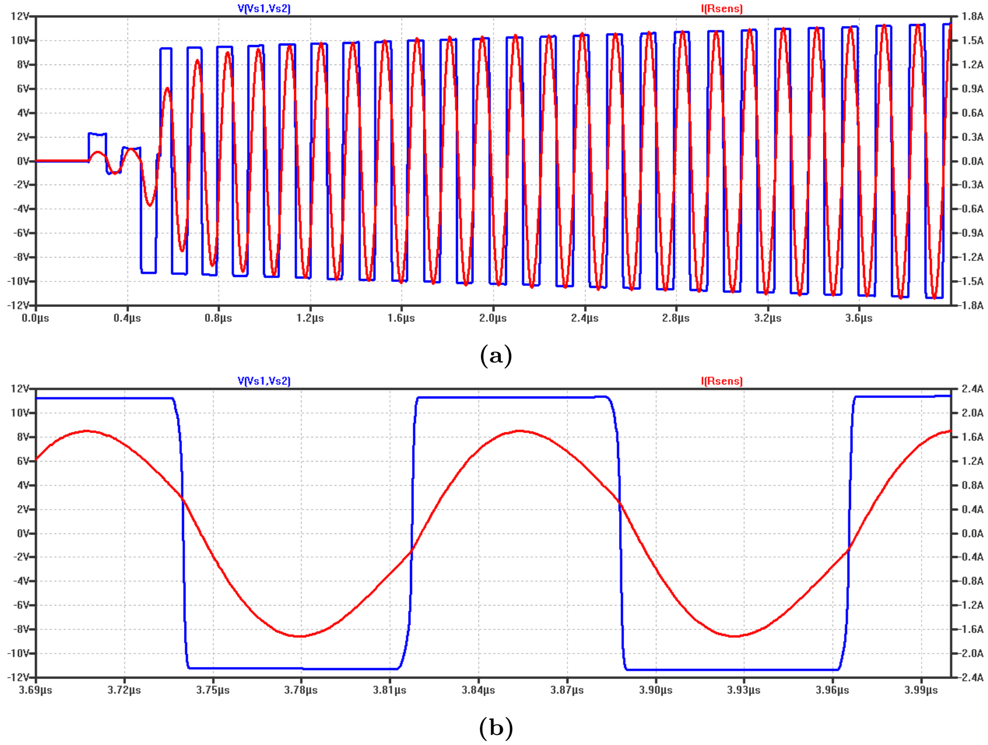

Figure 3.21: Simulation waveforms: (a) Input current and voltage, (b) Zoomed-in waveforms in steady-state. Square wave: resonant tank input voltage (v_s), sinusoidal wave: inductor current (i_L).

3.7.4 Experimental Results

An experimental prototype of the resonant converter with the proposed hysteresis compensation network has been built following the specifications reported above. Resonant inductance and capacitance values have been modified to 300 nH and 1.2 nF respectively in order to account for the parasitic inductance of the circuit.

Fig. 3.22 shows the scheme of the circuit for inverter and rectifier configurations. As depicted, the inverter configuration is obtained if the load is directly connected at the output. Then, the rectifier configuration is obtained if the load is substituted by a full-wave rectifier and a LC filter. In both cases V_{th} is set-up by adjusting an external voltage divider. Table 3.4 summarizes the components employed in the prototype, while Fig. 3.23 shows a picture of the prototype, which has a total size of 78 x 78 x 10 mm (width x length x height) and a weight of 75 grams.

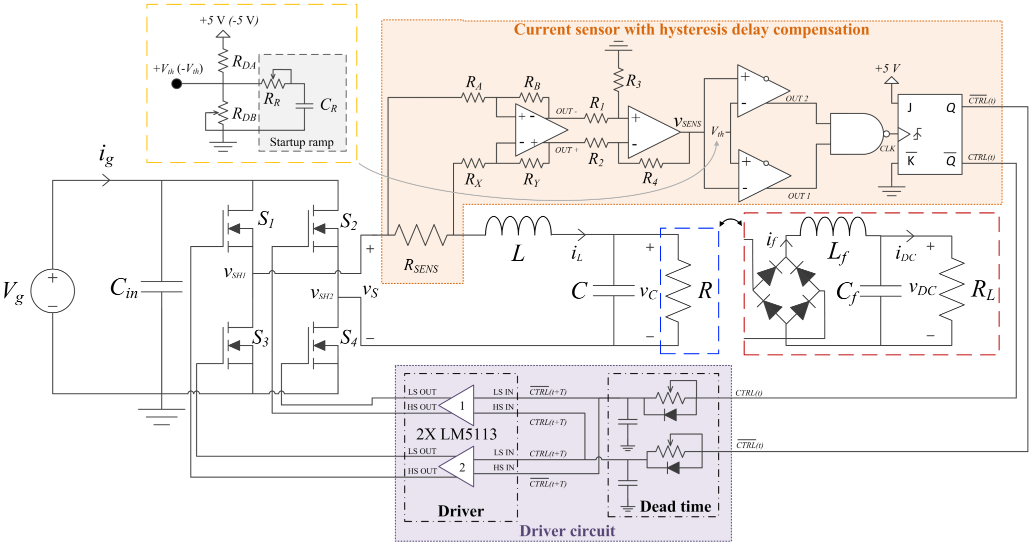

Figure 3.22: Circuit scheme for inverter and rectifier configurations. Inverter configuration: blue box, rectifier configuration: red box. Hysteresis threshold circuit: yellow box.

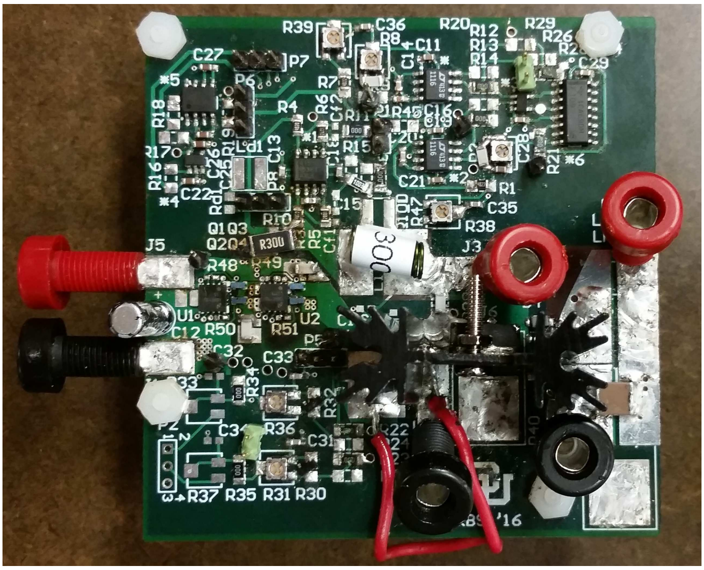

Figure 3.23: Picture of the prototype board.

Table 3.4: Summary of components of the experimental prototype

Component	Code or Value
L (Exp.)	300 nH
C (Exp.)	1.2 nF (C0G)
V_g	12 V
C_{in}	22.1 μF
Differential Amplifier	THS4151
eGaN FET (S_{i})	EPC8004
Driver	LM5113
R_{SENS}	0.3 Ω
R_A,R_X	402 Ω
R_B,R_Y	2010 Ω
R_1,R_2,R_3,R_4	100 kΩ
R_{DA}	4 kΩ
R_{DB},R_R	100 kΩ
C_R	250 pF
NAND gate	NC7S08
JK monostable	SN74F109DR
Comparator	LT1116
Diodes (Rect.)	PMEG10020ELRX
L_f (Rect.)	1 μH
C_f (Rect.)	0.47 μF
R, R_L	57 Ω

3.7.4.1 Inverter configuration

Fig. 3.24 illustrates the experimental behavior of the circuit in steady-state self-oscillating operation with the proposed delay compensation. The converter is able to auto-start and self-oscillate by simply applying power to the input port.

The self-oscillating pattern generates a 12 V square-wave at the input of the resonant tank, which oscillates at a frequency of 6.7 MHz thanks to the delay compensator. At this frequency, an average output power delivery of 16 W for a load $R = 57\ \Omega$ is obtained, with an overall efficiency of 98 %. For comparison, Fig. 3.25 shows the operation of the converter with no delay compensation, illustrating the phase-shift between the input current and the input voltage.

The converter operates near the ZVS mode at the nominal switching frequency. In Fig. 3.24, it can be seen that the square wave exhibits a small oscillation at the end of the negative cycle, which denotes that ZVS is not fully achieved in that case. An additional test, whose result is depicted in Fig. 3.26, shows that ZVS can be achieved if a slightly higher switching frequency, within tolerance limits of the Airfuel standard, is imposed (6.85 MHz).

Finally, it is worth noting that the prototype does not include an specifically designed WPT inductor, i.e.: it can not transfer wireless power at the moment. Nonetheless, accomplishment of the AirFuel Alliance class 3 WPT standard has been verified, as its power stage specifications are fully achieved.

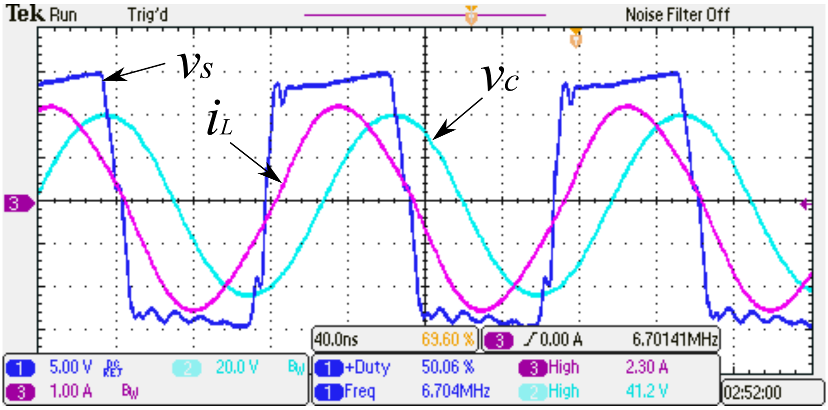

Figure 3.24: Input voltage, input current and capacitor voltage waveforms in nominal conditions.

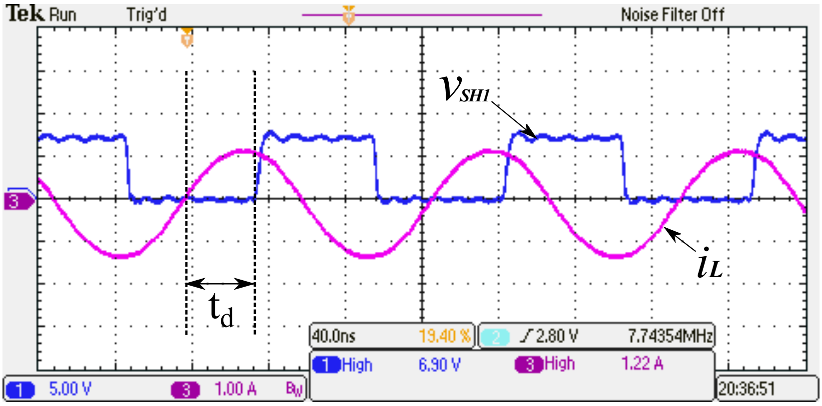

Figure 3.25: Positive input voltage and input current waveforms without delay compensation.

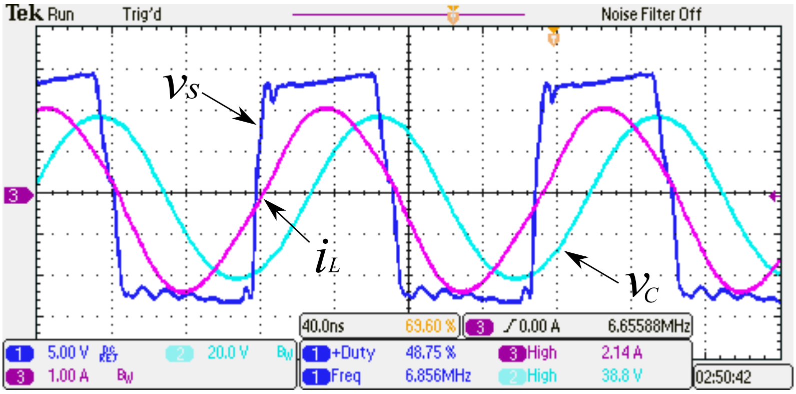

Figure 3.26: Input voltage, input current and capacitor voltage waveforms for a switching frequency of 6.85 MHz.

3.7.4.2 Rectifier configuration

In addition, the applicability of this circuit as a small form factor wired battery charger for mobile phones is validated under its rectifier configuration.

A switching frequency of 6.78 MHz is obtained for an average output power of 6 W with a load $R_L = 57\ \Omega$, as depicted in Fig. 3.27. The results comply with the requirements established by class 3 receiver of AirFuel Alliance standard, which defines an average charging power of 6 W for each individual receiver. It can be observed that the input current and the input voltage are not in phase, which results in an important reduction of the input power. The power efficiency in this prototype is 83 %, which is significantly lower than that of the inverter configuration mainly due to the losses introduced by the diode bridge.

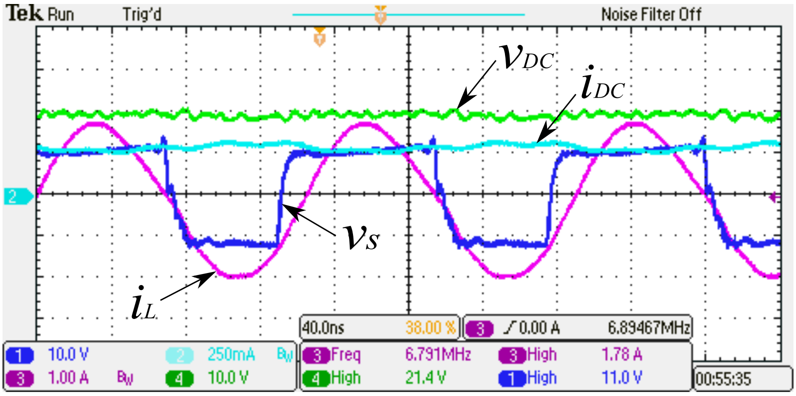

Figure 3.27: Input/output current and voltage waveforms in the rectifier configuration.

3.8 Summary

In this chapter an analytical procedure establishing with exactitude the restrictions for having self-oscillation in 2nd order structures has been presented. The analytical predictions have been validated by simulation and the effect of propagation delays in the experimental implementation of a self-oscillating converter has been discussed. Finally, the design of a practical application has been presented in order to verify the feasibility of the concepts developed in the chapter. Different delay compensation networks have been introduced and their performances verified.

4

Chapter 4

Modeling and control of second order resonant structures

In this chapter, a new modeling and control approach for self-oscillating resonant power converters is described. The desired self-oscillating control is based on the variation of the angle α introduced in Chapter 2 by means of the variation of the associated parameter k. Therefore, static and dynamic k-to-switching frequency models for 2nd order self-oscillating systems are obtained. These models are appended to the existent switching frequency-to-output voltage envelope model introduced in [32], in order to obtain the complete k-to-output behavior. This methodology links the properties of the self-oscillating voltage control proposed in Chapter 2 with the features of the previous conventional frequency modulation (FM) control presented in Chapter 1 [29–31].

The complete model is used for the synthesis of a switching angle controller able to regulate the output voltage of a PRC. The performance of the PRC with the switching angle controller is then compared with the response of the same converter controlled with conventional FM control in order to evidence the benefits of this new approach.

4.1 Static modeling

The self-oscillating control law applied and presented previously in Chapter 2 is based on the variation of the switching instant by means of a variable switching boundary instead of the fixed boundary defined by the sign of the inductor current. The control of the switching instants, then, depends on the angle between both boundaries, as illustrated in Fig. 2.6a. An analytic expression of the angle α for the PRC reproduced in Fig. 4.1 can be obtained as follows:

$$\begin{aligned}
\alpha =&\angle Z_i(s)\big|_{s=j\omega_{\mathrm{sw}}} = \angle\left(-\frac{\left(j\frac{\omega_{\mathrm{sw}}}{\omega_{\mathrm{o}}}\right)^2 + j\frac{\omega_{\mathrm{sw}}}{Q\omega_{\mathrm{o}}}+1}{jC\omega_{\mathrm{sw}}+\frac{1}{R}}\right) = \\
=&\angle\left(-\frac{\left(j\frac{\omega_{\mathrm{sw}}}{\omega_{\mathrm{o}}}\right)^2 + j\frac{\omega_{\mathrm{sw}}}{Q\omega_{\mathrm{o}}}+1}{jC\omega_{\mathrm{sw}}+\frac{1}{R}}\right)\left(\frac{\frac{1}{R}-jC\omega_{\mathrm{sw}}}{\frac{1}{R}-jC\omega_{\mathrm{sw}}}\right) \\
=&\angle\left(\left(\frac{\omega_{\mathrm{o}}}{Q}-j\omega_{\mathrm{sw}}\right)\left(-\left(j\frac{\omega_{\mathrm{sw}}}{Q\omega_{\mathrm{o}}}+\left(1-\left(\frac{\omega_{\mathrm{sw}}}{\omega_{\mathrm{o}}}\right)^2\right)\right)\right)\right) = \\
=&\arctan\left(-Q\frac{\omega_{\mathrm{sw}}}{\omega_{\mathrm{o}}}\left(1-\frac{1}{Q^2}-\left(\frac{\omega_{\mathrm{sw}}}{\omega_{\mathrm{o}}}\right)^2\right)\right).
\end{aligned} \tag{4.1}$$

$$k = \tan(\alpha) = -Q\frac{\omega_{\mathrm{sw}}}{\omega_{\mathrm{o}}}\left(1-\frac{1}{Q^2}-\left(\frac{\omega_{\mathrm{sw}}}{\omega_{\mathrm{o}}}\right)^2\right). \tag{4.2}$$

with $Q = \omega_0 RC = R/R_0$ and damping ratio $\xi = \frac{1}{2Q}$.

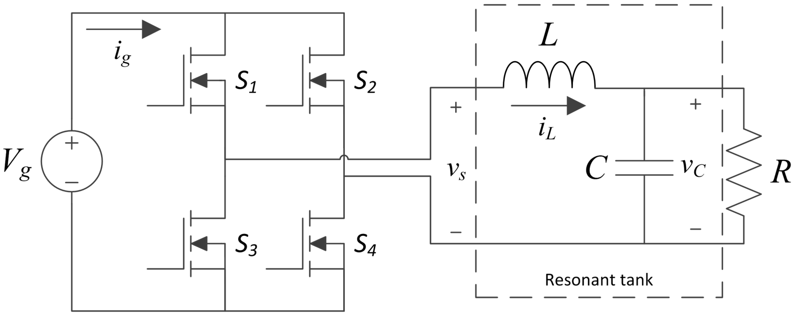

Figure 4.1: Circuit diagram of the PRC.

Assuming that the converter operates near the resonant frequency, the previous expression can be linearized around that point, where $\omega_{\text{sw}} = \omega_{\text{o}} + \hat{\omega}_{\text{sw}}$:

$$\begin{aligned} k(\omega_{\text{o}} + \hat{\omega}_{\text{sw}}) &= \frac{(\omega_{\text{o}} + \hat{\omega}_{\text{sw}})\left(1 - \frac{1}{Q^2} - \frac{{\omega_{\text{o}}}^2}{{\omega_{\text{o}}}^2} - \frac{2\omega_{\text{o}}\hat{\omega}_{\text{sw}}}{{\omega_{\text{o}}}^2} - \frac{\hat{\omega}_{\text{sw}}^2}{{\omega_{\text{o}}}^2}\right)}{\frac{-\omega_{\text{o}}}{Q}} \\ &= \frac{1}{Q} + \left(\frac{2Q}{\omega_{\text{o}}}\hat{\omega}_{\text{sw}} + \hat{\omega}_{\text{sw}}\frac{1}{\omega_{\text{o}}Q}\right) + \left(\frac{Q}{{\omega_{\text{o}}}^2}\hat{\omega}_{\text{sw}}^2 + \frac{2Q}{{\omega_{\text{o}}}^2}\hat{\omega}_{\text{sw}}^2 + \frac{Q}{{\omega_{\text{o}}}^3}\hat{\omega}_{\text{sw}}^3\right) \\ &\simeq \frac{1}{Q} + \hat{\omega}_{\text{sw}}\left(\frac{2Q}{\omega_{\text{o}}} + \frac{1}{\omega_{\text{o}}Q}\right). \end{aligned} \tag{4.3}$$

and considering that $2Q \gg 1/Q$, this equation can be rewritten as:

$$k = \frac{1}{Q} + 2Q\left(\frac{\omega_{\text{sw}}}{\omega_{\text{o}}} - 1\right). \tag{4.4}$$

Fig. 4.2 shows the exact nonlinear function (4.2) and its approximated linear expression (4.4) for a range of values of k, corresponding to α angles between [-75, 75] degrees. The linear approximation is in good agreement with the nonlinear original expression and provides a direct way to relate the value of k and the switching frequency of the converter. Because this is a direct consequence of the linear phase shape around ω_{o}, the valid frequency range of this expression shrinks with larger values of Q. In the example of Fig. 4.2, where values of Q up to 40 are shown, the model can be considered valid for $\alpha \in$ [-75, 75] degrees, providing a wide valid frequency span around resonance.

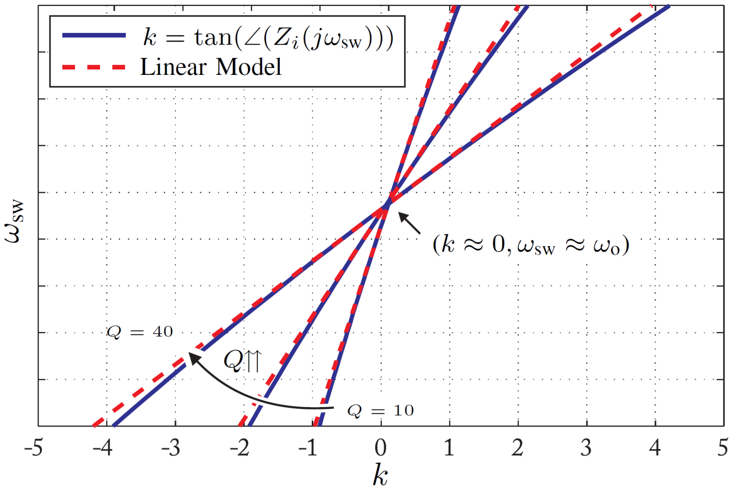

Figure 4.2: Exact switching frequency of the PRC with respect to parameter k for three different values of Q = [10, 20, 40] and its linear approximation.

If k is considered constant, this linear model can be used to obtain the steady-state characteristics of the converter by conventional frequency domain methods. For example, the amplitude of the output voltage in the PRC will be defined only by the design of the resonant tank, the load applied and the parameter k:

$$\begin{aligned} V_C &= \left| H(s)|_{s=j\left(\left(k-\frac{1}{Q}\right)\frac{\omega_\text{o}}{2Q}+\omega_\text{o}\right)} \right| V_\text{s1} \\ &= \left| \left(\frac{1}{LCs^2+\frac{L}{R}s+1} \right) |_{s=j\left(\left(k-\frac{1}{Q}\right)\frac{\omega_\text{o}}{2Q}+\omega_\text{o}\right)} \right| V_\text{s1} \\ &= \left| \frac{1}{1+\left(\left(\left(k-\frac{1}{Q}\right)\frac{\omega_\text{o}}{2Q}+\omega_\text{o}\right)\left(-LC+j\frac{L}{R}\right)\right)} \right| V_\text{s1} \end{aligned} \tag{4.5}$$

where $H(s) = \frac{v_C(s)}{v_\text{s1}(s)}$ is the input to output voltage transfer function of the resonant tank.

The result in (4.4) shows clearly that a simple gain relates k to ω_{sw}. The DC gain established by equation (4.6) is expressed with the variables in incremental form due to the small-signal nature of the model and with time dependence due to its variable nature, i.e.: $k(t) = K + \hat{k}(t)$, $\omega_\text{sw}(t) = \Omega_\text{sw} + \hat{\omega}_\text{sw}(t)$, $\alpha(t) = A + \hat{\alpha}(t)$, and with $v_\text{env}(t) = V_\text{env} + \hat{v}_\text{env}(t)$ being the output voltage envelope and $G_\text{env}(s)$ being the existent switching frequency-to-output voltage envelope transfer function. Further details about the switching frequency-to-output voltage envelope transfer function $G_\text{env}(s)$, developed by R. W. Erickson, can be found in [21, 32, 90–92].

$$\hat{\omega}_\text{sw} = \frac{\omega_\text{o}}{2Q}\hat{k}. \tag{4.6}$$

Fig. 4.3a shows the $\hat{k}$-to-$\hat{\omega}_{sw}$ DC model of a PRC with the self-oscillating voltage control law ($u = sg(j_L - Km_C)$) appended to the switching frequency-to-output voltage envelope transfer function, while Fig. 4.3b depicts the model of a PRC with the standard FM control approach, which depends only on the previous frequency-to-output model. Note that the time dependence of the incremental variables may be omitted in the figure for convenience.

In comparison with standard FM circuits, it is clear that self-oscillating control reduces the uncertainty on DC gain variation due to the dependence of $\hat{\omega}_\text{sw}$ on Q in (4.6) and the dependence of Q on the load. Increasing load variations generate higher Q values that reduce the increments of the DC gain in the frequency-to-output model.

Fig. 4.4a depicts the Bode plots of the control-to-output transfer function of a parallel resonant converter designed with the parameters of Table 4.1. The

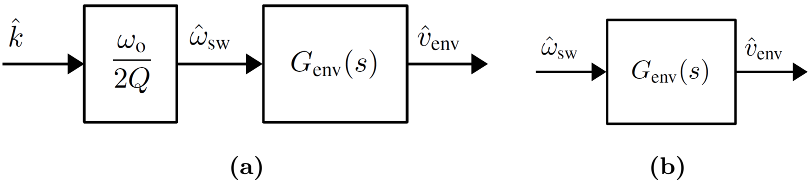

Figure 4.3: Block diagram of the small-signal DC model of the system considering: (a) the self-oscillating control ($u = sg(j_L - k(t)m_C)$), (b) the standard FM controller.

responses of the converter with conventional FM control and self-oscillating control are shown in dashed and solid lines respectively. Three different loads, or in other words, three different quality factors $Q = 11, 15, 30$ are shown for the same switching frequency. While the conventionally controlled converter presents a DC gain variation of approximately 10 dB, self-oscillating control reduces this uncertainty to negligible values. This reduced DC gain variation can be observed in Fig. 4.4b, where changes in the switching frequency are considered in order to compensate for changes in the load, thus maintaining the same output voltage amplitude. Although the load range has been increased, it can be seen that, for this set of parameters, self-oscillating control reduces the uncertainty of the DC gain by a factor of approximately 1/2.

Table 4.1: Parameters of the parallel resonant converter design example

Parameter	Value
V_g	12 V
V_{env}	160 V
L	8.3 μH
C	10.5 nF
$f_o = \frac{\omega_o}{2\pi}$	540 kHz

Extension to the SRC

Following the same procedure presented in (4.1), (4.2), (4.3) and (4.4), it is possible to derive an analytic expression of α for the series resonant converter using the corresponding $\angle Z_i(s)|_{s=j\omega_{sw}}$ and noting that in the SRC $Q = \frac{R_o}{R}$.

The resulting nonlinear expression is

$$k = \tan(\alpha) = Q\left(\frac{\omega_{sw}}{\omega_o} - \frac{\omega_o}{\omega_{sw}}\right), \tag{4.7}$$

whose linear approximation is similar to the one found for the PRC:

$$k = 2Q\left(\frac{\omega_{sw}}{\omega_o} - 1\right) \tag{4.8}$$

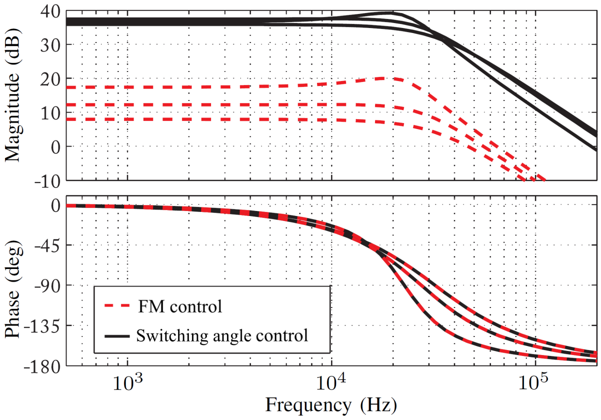

(a)

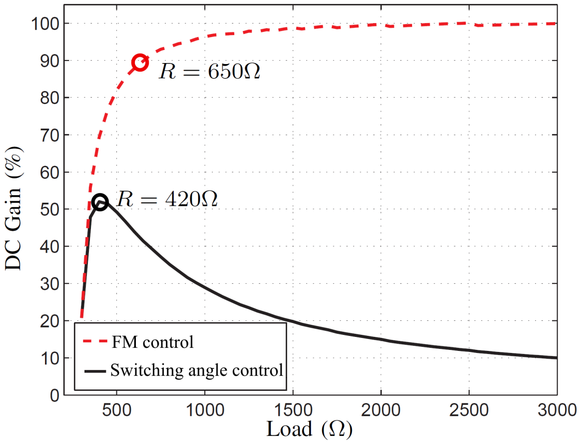

(b)

Figure 4.4: Effects of self-oscillating control on DC Gain: (a) Bode plots of $G_{\text{env}}(s)$ and $\frac{\omega_o}{2Q}G_{\text{env}}(s)$ for different quality factors $Q = 11, 15, 30$. (b) DC Gain versus load R, considering appropriate switching frequency changes for constant input/output gain.

The same DC gain is obtained for the small-signal model of the SRC, so that the concepts introduced previously are equally applicable.

4.2 Dynamic modeling

The model in Fig. 4.3a does not consider the transient response of the switching frequency when a change in $k(t)$ is experimented. Therefore, it is required to derive a dynamic model that describes the behavior of the circuit under such circumstances.

As depicted in Fig. 4.5, the proposed switching angle control presents two main dynamic features. First, after a change in $\hat{k}(t)$, there exist a shift of the switching frequency during the next half-period. In addition, the settling time of $\hat{\omega}_{\text{sw}}(t)$ is determined by the time constant of the state variables and the quiescent operating point K. The high-frequency dynamics is caused by the reduction of the period of the next semicycle after a change on $\hat{k}(t)$, as shown in Fig. 4.5a. As a result, the overall time of the cycle is shorter and, in consequence, the frequency is higher. The low-frequency dynamics is generated by the inherent settling time associated to the change of phase-shift produced by the $\hat{k}(t)$ variation. This effect can be observed in Fig. 4.5b, where both time-domain transients are depicted. $\hat{\omega}_{sw1}(t)$ is the small-signal variation of the switching frequency produced by the high-frequency transient and $\hat{\omega}_{sw2}(t)$ is the variation produced by the low-frequency transient.

Assuming linearity, it is possible to study the influence of both types of variation on the switching frequency separately and to formulate the output of the switching angle control as a combination of two transfer functions appended to the previous frequency to output voltage envelope transfer function.

4.2.1 High-frequency response

In general, $\Delta\hat{k}$ will be small with respect to K if the system is designed correctly. This is because small frequency variations generate large output voltage variations due to the high Q factor. Under this condition, $\Delta\hat{\omega}_1$ can be approximated by a proportional relationship between the switching frequency in steady-state (when it describes an angle approximately equal to π) and the switching frequency during the first half period (when it describes an angle equal to $\pi-\Delta\hat{\alpha}$).

$$\Delta\hat{\omega}_1 = \frac{\Omega_{\text{sw}}}{\pi}\Delta\hat{\alpha}, \tag{4.9}$$

where the angle $\Delta\hat{\alpha}$ is defined as

$$\begin{aligned} \Delta\hat{\alpha} &= \arctan(K+\Delta\hat{k}) - \arctan(K) \\ &= \arctan\left(\frac{\Delta\hat{k}}{K^2+K\Delta\hat{k}+1}\right) \end{aligned} \tag{4.10}$$

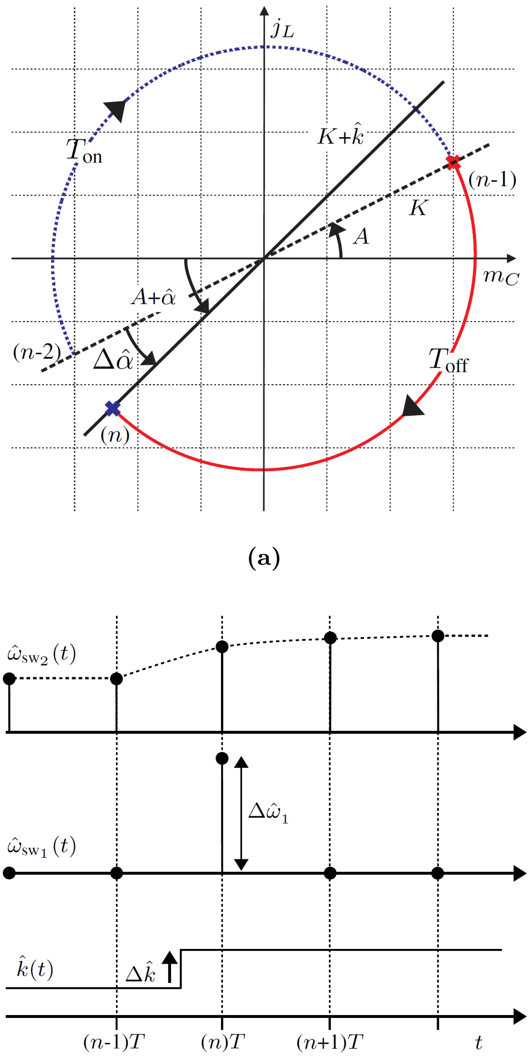

(a)

(b)

Figure 4.5: Changes in the switching frequency due to a time-varying $k(t) = K+\hat{k}(t)$. (a) State-plane normalized trajectory of a PRC after a change in $\hat{k}$. (b) Time-domain waveforms.

Considering $\Delta\hat{k} \simeq 0$ due to the small value of the variation, $\Delta\hat{\alpha}$ could be approximated as

$$\Delta\hat{\alpha} \simeq \frac{\Delta\hat{k}}{K^2+1} \tag{4.11}$$

with $\Delta\hat{k} = \hat{k}(n) - \hat{k}(n-1)$ and $\Delta\hat{\alpha} = \hat{\alpha}(n) - \hat{\alpha}(n-1)$.

Using (4.9) and (4.11), a discrete-time model can be derived as follows

$$\hat{\omega}_{\mathrm{sw}_1}(n) = \frac{\Omega_{\mathrm{sw}}}{\pi}\frac{1}{K^2+1}\left(\hat{k}(n) - \hat{k}(n-1)\right), \tag{4.12}$$

or equivalently

$$\frac{\hat{\omega}_{\mathrm{sw}_1}(z)}{\hat{k}(z)} = \frac{\Omega_{\mathrm{sw}}}{\pi}\frac{1}{K^2+1}(1-z^{-1}). \tag{4.13}$$

This model can be appended to a sampler and a zero-order holder, in order to account for the inherent sampling, and transformed into a continuous-time transfer function using the equivalence $z^{-1} = e^{-sT}$and a first-order Padé approximation.

The transfer function that models the switching frequency shift can then be written as

$$\frac{\hat{\omega}_{\mathrm{sw}_1}(s)}{\hat{k}(s)} = \frac{\Omega_{\mathrm{sw}}}{\pi}\frac{1}{K^2+1}\frac{sT}{\left(1+s\frac{T}{2}\right)} \tag{4.14}$$

4.2.2 Low-frequency response

It is required to establish a relationship between $\hat{k}$ and output voltage variations in order to explain in detail the origin of the low-frequency response. Fig. 4.6 shows the time-domain waveforms of j_L, m_C and $j_L - Km_C$, for two different, but constant, values of k. In the first case ($K = 0$), $j_L - Km_C$ is equal to j_L and the switching signal only depends on the sign of the inductor current, not on its amplitude. As a consequence, the settling time of j_L does not affect the switching instants and τ is equal to zero. As K increases, the dependence of the switching instants on the amplitudes of the inductor current and the capacitor voltage grows, given that $\mathrm{sg}(j_L - Km_C)$ depends on such amplitudes. Due to that, the dynamics associated with the variation of these amplitudes affect the overall response of the controller.

The low frequency dynamics between $\hat{k}(t)$ and $\hat{\omega}_{\mathrm{sw}}(t)$ can also be modeled by the same discrete-time domain methods described above. In this case, the model is assumed to be a first order low-pass filter for simplicity. The response of a first order low-pass filter is defined by

$$x(k) = \frac{\tau}{T+\tau}x(K-1) + K\frac{T}{T+\tau}u(k) \tag{4.15}$$

Applying equation (4.15) in the system analyzed results in

$$\widehat{\omega}_{sw2}(n) = \frac{\tau}{T+\tau}\widehat{\omega}_{sw2}(K-1) + \frac{\omega_0}{2Q}\frac{T}{T+\tau}\widehat{k}(n) \tag{4.16}$$

or equivalently

$$\frac{\widehat{\omega}_{sw2}(n)}{\widehat{k}(n)} = \frac{\frac{\omega_0}{2Q}T}{T+\tau-\tau z^{-1}} \tag{4.17}$$

where $\hat{\omega}_{\mathrm{sw}_2}(n)$ is the low-frequency response, as shown in Fig. 4.5b, and τ is a time constant that depends on the time constant of the resonant tank.

Following the same procedure of the previous section and after the transformation from discrete time domain, the continuous time domain response model is obtained:

$$\frac{\hat{\omega}_{\mathrm{sw}_2}(s)}{\hat{k}(s)} = \frac{\omega_{\mathrm{o}}}{2Q}\frac{1}{1+\tau s+s\frac{T}{2}}, \tag{4.18}$$

Factor $s\frac{T}{2}$ is included due to the existent sampling time after discretization and application of the bilinear transformation.

In the PRC, the inductor current and capacitor voltage settle with a time constant τ of the following form [69]:

$$\tau = 2RC \tag{4.19}$$

Consequently, the settling time of $\hat{\omega}_{\mathrm{sw}}$ approaches $2RC$ when K grows due to its dependence on the amplitude of the variables and is characterized by the dominant dynamics of this system. Therefore, it can be assumed that the time constant τ grows following a sinusoidal function of the state variables, such that a general

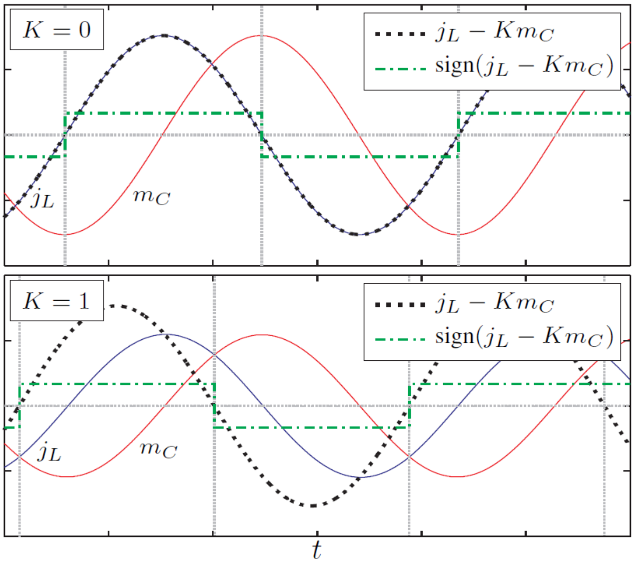

Figure 4.6: Time-domain waveforms of the PRC for two different values of $K\,[0, 1]$.

model can be written as:

$$\tau = 2RC\sin(\arctan(|K|)) = 2RC\frac{|K|}{\sqrt{1+K^2}}. \tag{4.20}$$

This model provides a direct way to relate the value of K and the settling time of the switching frequency and establishes the dependence of the settling time on the amplitude of the variables. Fig. 4.7 depicts this dependence relationship, showing the percentage values of τ with respect to $2RC$ for a range of values of K corresponding to angles between [0, 85] degrees. Note that the absolute value of K is used in order to avoid negative time constants when $K < 0$.

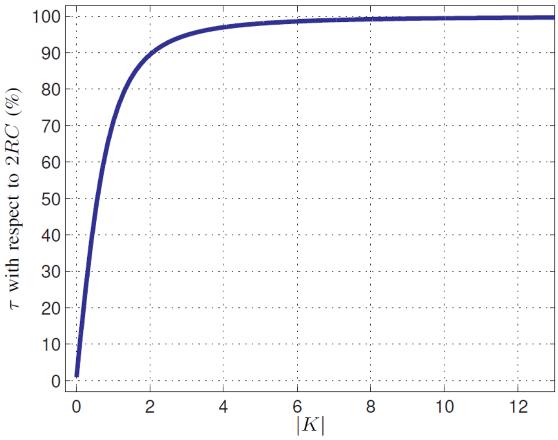

Figure 4.7: Settling time τ as a function of $|K|$.

4.3 Complete model

Both high-frequency and low-frequency dynamic models are appended to the DC gain model obtained previously and the existent frequency-to-output transfer function in order to obtain the complete model. The block diagram of the complete small-signal model between the control variable $\hat{k}$ and the output $\hat{v}_{\text{env}}$ is depicted in Fig. 4.8. While this result has been derived with the PRC in mind, it is worth noticing that it is also valid for the SRC.

In order to validate the model, Bode plots of the control-to-output transfer functions for two frequencies below resonance f_{sw} = [525 kHz, 500 kHz] are shown in Fig. 4.9. The values of the parameters used to plot the Bode diagram are those indicated previously in Table 4.1: $L = 8.3$ μH and $C = 10.5$ nF.

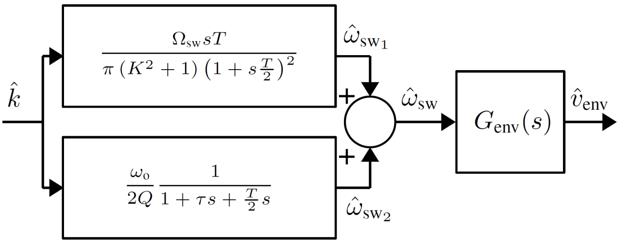

Figure 4.8: Block diagram of the complete small-signal model.

Table 4.2: Operating point values

Q	f_{sw}	K
11.8	525 kHz	-0.5
11.8	500 kHz	-1.4
17.8	525 kHz	-0.8
17.8	500 kHz	-2.2

Fig. 4.9a shows the analytic small-signal model response (solid line) against a simulation of the switched circuit (circle marks) for $Q = 11.8$ ($R = 330\,\Omega$), whereas Fig. 4.9b shows the same results for $Q = 17.8\,(R = 500\,\Omega)$. The resulting values of K are enumerated in Table 4.2. It can be seen that the model is in good agreement with the simulation results and that it remains valid up to frequencies below 200 kHz. In addition, the switching angle control cancels the effects of the double pole below the switching frequency that appears in the control-to-output transfer function with conventional frequency modulation. As a consequence, with the switching angle control, the phase is well above 180° for the range of frequencies that can be of interest for feedback, and the system dynamics are similar to those of a first order system [46]. These aspects suggest that closed-loop regulation by means of a switching angle controller can outperform standard frequency modulation controllers due to larger feedback bandwidth and improved robustness.

Additionally, experimental results were taken under equal design conditions to verify the previous simulations and the overall modeling approach. The experimental circuit scheme, shown in Fig. 4.10, is made up of an H-bridge circuit, employing four MOSFETs (IPB200N15N3 G), and a resonant tank composed of a ceramic capacitor and an air-gap-based inductor whose corresponding values are given in Table 4.1. A LT1116 comparator is employed in order to establish the change of polarity of the control signal and a 1:8 current transformer for current sensing purposes. Voltage and current normalization are made with an LT1362CS operational amplifier, while multiplication is made with a AD734 multiplier. Op-

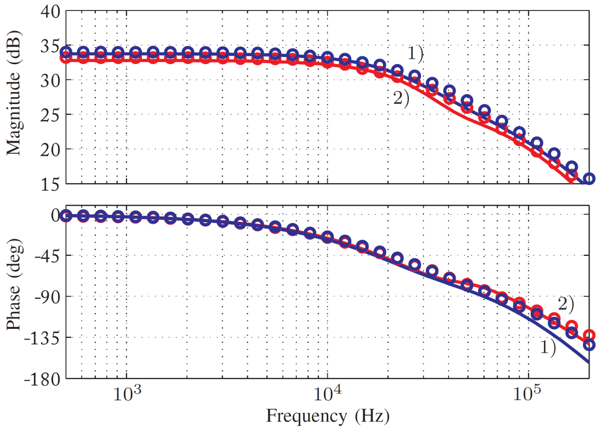

(a) $Q = 11.8$ (R = 330 Ω)

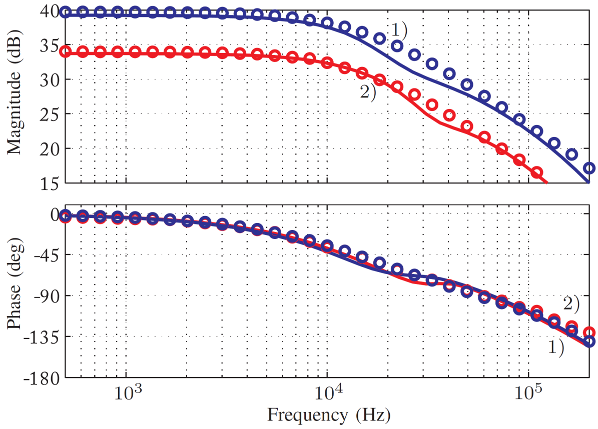

(b) $Q = 17.8$ (R = 500 Ω)

Figure 4.9: Response of the proposed model and a simulation for two different switching frequencies: 1) 525 kHz. 2) 500 kHz. Solid-line: analytic model. Circle marks: simulation results.

eration below resonance ($k < 0$) is imposed. Fig. 4.11 depicts four measurements of the frequency response, matching those shown in the simulations. The measurements have been carried out with a Venable FRA-3120 network analyzer and a small ac signal $\hat{k}$ is added to the DC value of the input K in open loop and the envelope of the output voltage is measured as the output.

It can be observed a good agreement between the solid lines (analytic model) and the experimental measurements (x marks), validating the model obtained and the modeling technique applied. Although there exist minor discrepancies in phase responses above 50 kHz, these differences are not usually a problem for

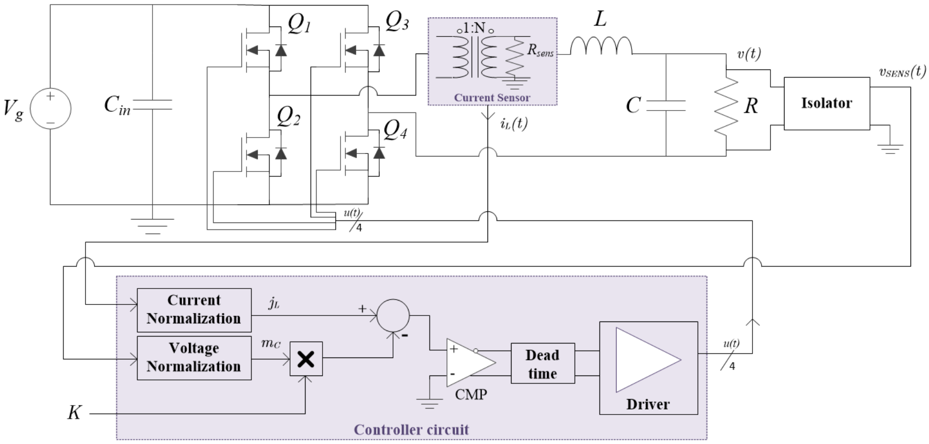

Figure 4.10: Parallel resonant converter with a switching control law based on $u = sg(j_L - Km_C)$.

closed-loop control, given that effective bandwidths are typically lower and that phase responses are always above -180°.

4.4 Control

A switching angle controller is derived from the previous complete model in order to regulate the output voltage. Its structure and response is compared throughout this section with standard FM approaches. A block diagram of the proposed regulated converter and the classic FM approach are shown in Figs. 4.12a and 4.12b respectively. It is worth to point out that the output voltage envelope sensing is carried out by means of a peak detector and that the FM realization requires a voltage-controlled oscillator (VCO). All the synthesized controllers follow a PI structure consisting of an integrator for zero steady-state error, a phase leading zero for appropriate phase margin, and an additional high frequency pole for noise immunity.

In order to unify the design criteria, all the controllers must satisfy a minimum phase margin ϕ_{M} of 45° and a gain margin G_{M} above 10 dB. Moreover, the power stage of the converter where these controllers will be eventually applied is similar to the one in the previous section. A nominal load of 420 Ω, a worst-case load of 650 Ω and a desired output voltage envelope V_{env} of 160 V are established, giving the parameters of the operating points of the controllers summarized in Table 4.3.

It is worth to point out that a nominal load of 420 Ω is selected in order to compare the response of the switching angle controller in the worst-case scenario, given that for this load it presents the maximum DC gain value (see Fig. 4.4b).

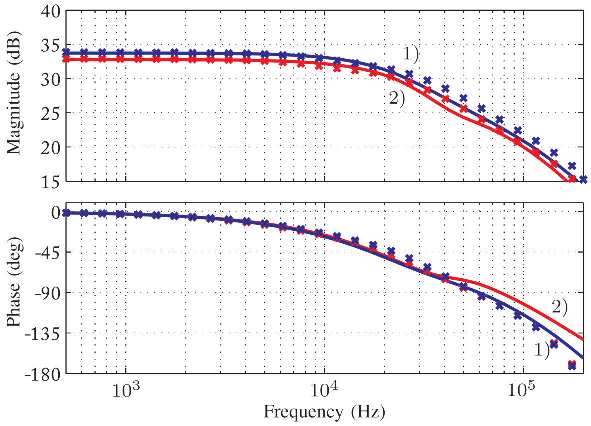

(a) $Q = 11.8$ (R = 330 Ω)

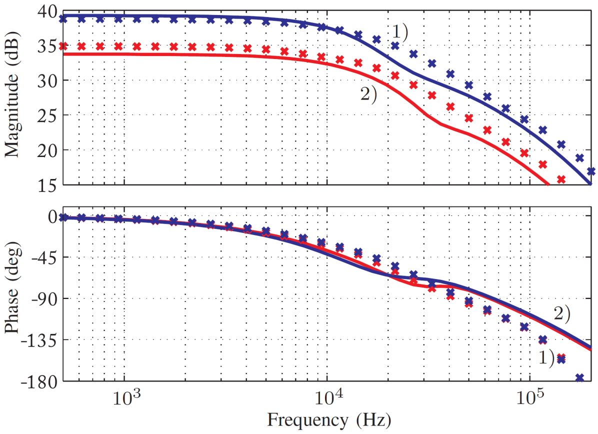

(b) $Q = 17.8$ (R = 500 Ω)

Figure 4.11: Response of the proposed model and experimental results for two different switching frequencies: 1) 525 kHz. 2) 500 kHz. Solid-line: analytical model. X marks: experimental measurements.

Table 4.3: Controller operating point values

R	V_{env}	Q	K	f_{sw}
420 Ω	160 V	15.2	-2.1	520 kHz
650 Ω	160 V	21.3	-3.2	515 kHz

Additionally, a worst-case load of $R = 650\ \Omega$ is selected taking into account that for that value the DC gain of the frequency-to-output transfer function is near its maximum value (see Fig. 4.4b).

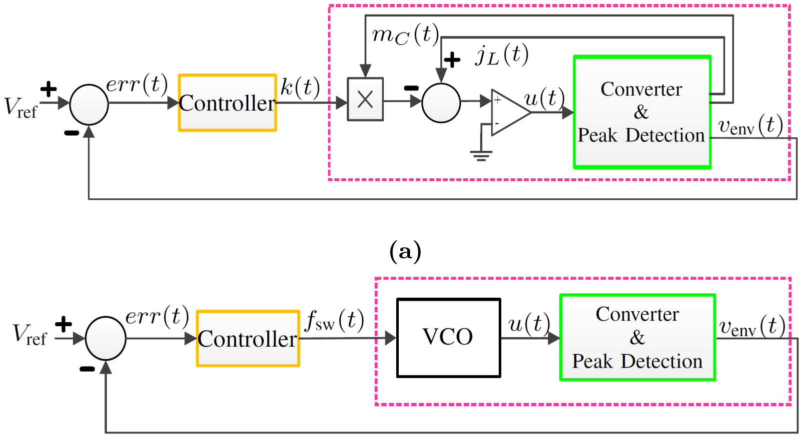

(b)

Figure 4.12: Closed-loop block diagram of the resonant converter with: (a) switching angle controller, (b) FM controller.

4.4.1 Design of controller for self-oscillating converter

The previous k-to-output model obtained for the PRC converter presents four poles and two zeros at low frequency range, and certain high frequency components. As depicted in Fig. 4.13, two of these poles are naturally compensated by the two zeros that exist in the nearest frequencies, so that the design of the controller is focused on compensating the remaining poles.

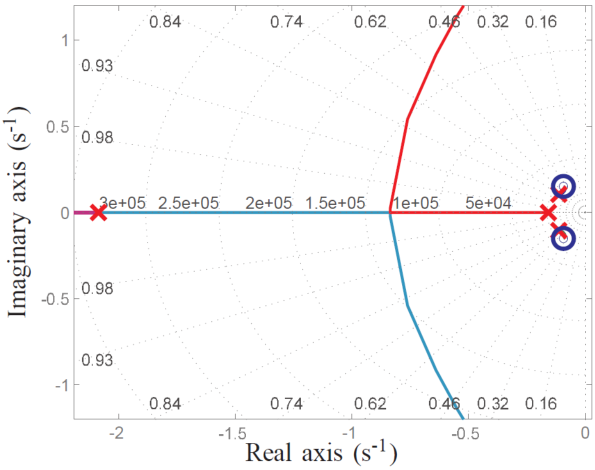

Figure 4.13: Pole-zero diagram of the complete k-to-output model.

Due to the reduced-order dynamics of the self-oscillating system, it is not necessary to implement a complex controller for obtaining benefits with respect to standard systems. As introduced before, a simple PI controller with an additional pole is designed. Equation (4.21) defines its transfer function.

$$G_{\mathrm{c,\,SO}(s)} = 3300\frac{1+6.9\cdot 10^{-6}s}{s(1+2.8\cdot 10^{-6}s)} = 8132\frac{s+145\cdot 10^{3}}{s(s+357\cdot 10^{3})} \tag{4.21}$$

Fig. 4.14 shows the loop gain of the PRC converter with the $G_{\mathrm{c,\,SO}(s)}$ controller, considering the nominal load of $R = 420\ \Omega$. A phase margin of 45° together with a gain margin of 17 dB can be easily achieved with a crossover frequency of approximately 25 kHz. Note that in this work this controller is named switching angle controller or $G_{\mathrm{c,\,SO}(s)}$.

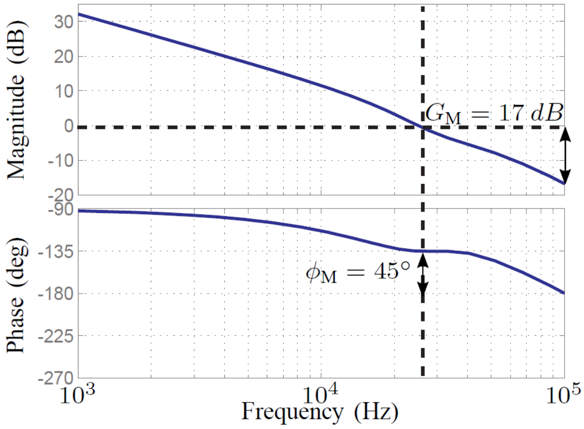

Figure 4.14: Bode plot of the loop gain in the switching angle controller designed.

4.4.2 Comparison between controllers for self-oscillating and FM converters

Two different FM controllers are designed applying the frequency-to-output transfer function $G_{env}(s)$ for comparison purposes. The first is designed for the nominal load for the fastest regulation and the second one is designed for the worst-case load to be robust against large load variations. In order to compare under equal conditions all their performances, the design criteria applied in the FM cases are the same than in the switching angle controller, and similar PI structures with an additional pole are applied.

4.4.2.1 Design of controllers for conventional FM converters

Nominal-load design

For the nominal-load situation ($R = 420\ \Omega$), a PI controller with an additional pole is designed. Equation (4.22) defines the obtained transfer function of the controller:

$$G_{\mathrm{c,FM1}}(s) = 1520\frac{1+8.5\cdot 10^{-6}s}{s(1+2.5\cdot 10^{-6}s)}. \tag{4.22}$$

A Bode plot of the loop gain with this controller is depicted in Fig. 4.15. A phase margin of 45° and a gain margin of exactly 10 dB are provided with a crossover frequency of approximately 20 kHz.

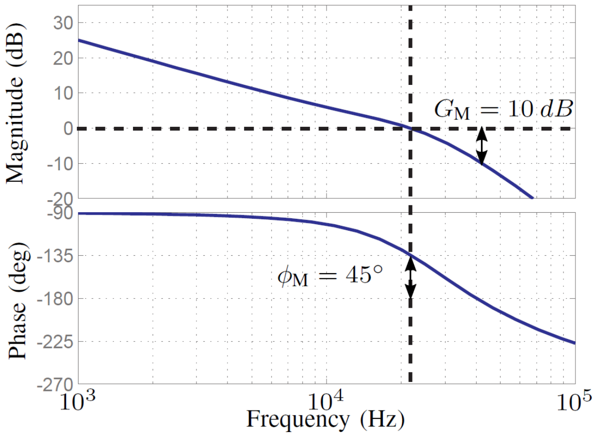

Figure 4.15: Bode plot of the loop gain in the FM controller designed for the nominal load.

Maximum-load design

Similarly as in the previous case, the second controller is designed considering the worst-case load of $R = 650\ \Omega$.

It is found that the crossover frequency required for satisfying a minimum phase margin of 45° and a gain margin of 10 dB is lower than in the previous cases: $f_c = 5$ kHz (Fig. 4.16). Besides, the use of a zero for improved phase margin provides a relatively small amelioration due to the influence of the resonant complex pole in $G_{\mathrm{env}}(s)$ at high frequencies, and for that reason it is eliminated.

These aspects result in a simpler and more conservative controller which presents the following transfer function:

$$G_{\mathrm{c,FM2}}(s) = 426\frac{1}{s(1+3\cdot 10^{-5}s)}. \tag{4.23}$$

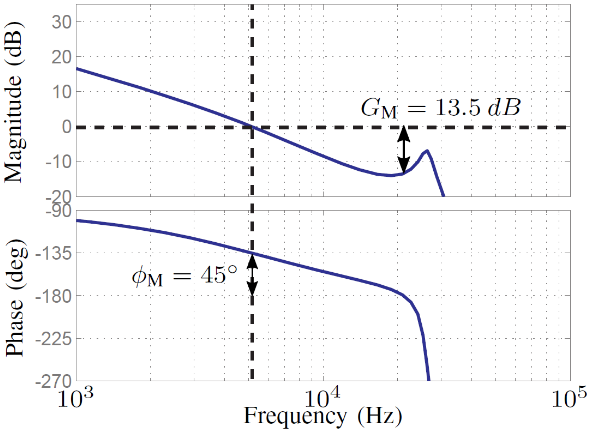

Figure 4.16: Bode plot of the loop gain in the FM controller designed for the worst-case load.

4.4.2.2 Simulation results

In order to verify the properties of the previous controllers, summarized in Table 4.4, load and input voltage transients are simulated and their responses are illustrated in Figs. 4.17 and 4.18. The objective is to obtain a regulated AC peak output voltage of $V_{\mathrm{env}} = 160$ V from an input of $V_{\mathrm{g}} = 12$ V.

Table 4.4: Controller specifications

Controller	*Type*	*R design*	G_M (dB)	ϕ_{M}(°)	f_c
Switching angle ($G_{\mathrm{c,SO}}$)	PI + HF pole	420 Ω	17 dB	45°	25 kHz
Nominal-load FM ($G_{\mathrm{c,FM1}}$)	PI + HF pole	420 Ω	10 dB	45.5°	22 kHz
Maximum-load FM ($G_{\mathrm{c,FM2}}$)	PI	650 Ω	13.5 dB	45°	5 kHz

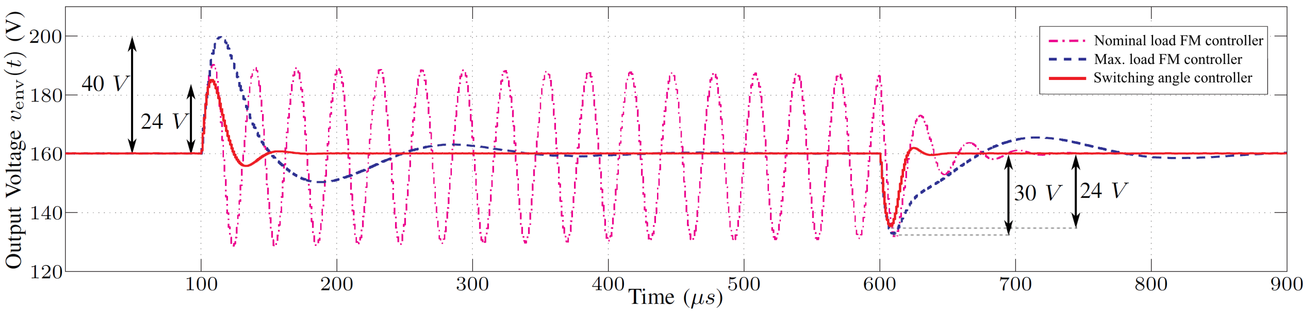

Figure 4.17: Response of each controller for a 420 Ω → 650 Ω → 420 Ω load transient with nominal input voltage. Solid-line: Switching angle controller. Dashed line: Nominal load FM controller. Dashed dotted line: Maximum load FM controller.

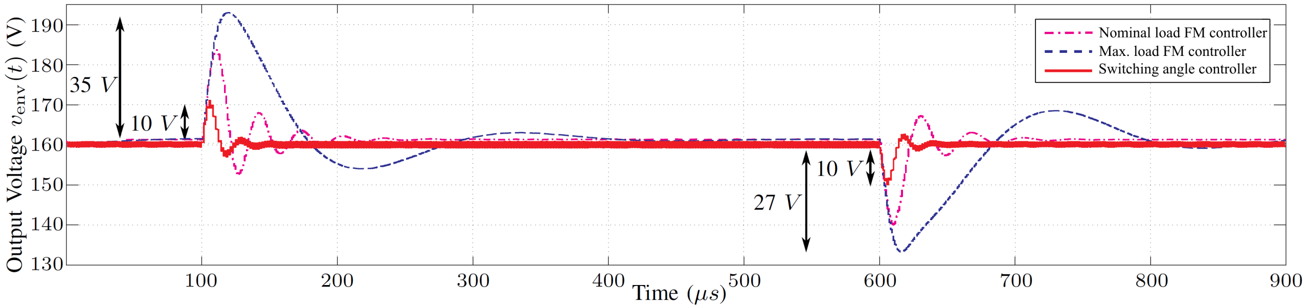

Figure 4.18: Response of each controller for a 12 V → 14 V → 12 V input voltage transient with nominal load (420 Ω). Solid-line: Switching angle controller. Dashed line: Nominal load FM controller. Dashed dotted line: Maximum load FM controller.

First, the three different controllers have been tested in presence of load disturbances. Fig. 4.17 shows a detail of the voltage regulation waveforms when the load changes from its nominal value $R = 420\ \Omega$ to the worst-case $R = 650\ \Omega$ at t = 100 μs and goes back to $R = 420\ \Omega$ at t = 600 μs. It can be seen that while the switching angle controller $G_{\mathrm{c,\,SO}}(s)$ (solid line) rejects the disturbance with a voltage deviation of 24 V and a settling time below 50 μs, the FM controller $G_{\mathrm{c,FM1}}(s)$ (dashed-line) becomes unstable and can not regulate the output voltage for this range of loads. The conservative controller $G_{\mathrm{c,FM2}}(s)$ (dash-dotted line) leads to a stable response in both operating points, but at the expense of worse disturbance rejection properties. The output voltage deviation and settling time obtained with it are about 40 V and 250 μs respectively.

Then, the same controllers have been tested in presence of input voltage disturbances. In Fig. 4.18, the input voltage V_{g} switches back and forth between 12 V and 14 V. Under that situation, the FM controllers $G_{\mathrm{c,FM1}}(s)$ and $G_{\mathrm{c,FM2}}(s)$ present voltage shifts above 20 and 30 V respectively, while the switching angle controller $G_{\mathrm{c,\,SO}}(s)$ presents a spike of only 10 V. Besides, this controller yields a well damped waveform with a settling time lower than 50 μs, in contrast with the poor responses of the conventional controllers.

4.4.3 Experimental results

Previous results are validated experimentally with the aim of contrasting the effectiveness of the model that has been derived and the control that has been synthesized.

A 100 W experimental prototype of a PRC has been built following the specifications established in Table 4.1. The power stage is the same as in Section 4.3 and its detailed scheme can be seen in Fig. 4.19.

Frequency Response Verification

A measurement of the response of the system for the new loads and frequencies applied on the control design (520 kHz/420 Ω and 515 kHz/650 Ω) is carried out in Fig. 4.20.

A good agreement can be observed between the solid lines (analytic model) and the experimental measurements (x marks). As in Section 4.3, although there exist minor discrepancies in phase responses above 50 kHz, these differences do not affect the performance of the designed closed-loop control. Its effective bandwidth is lower than $\frac{1}{10}$ of the switching frequency and the phase responses in all situations are always above -180 °.

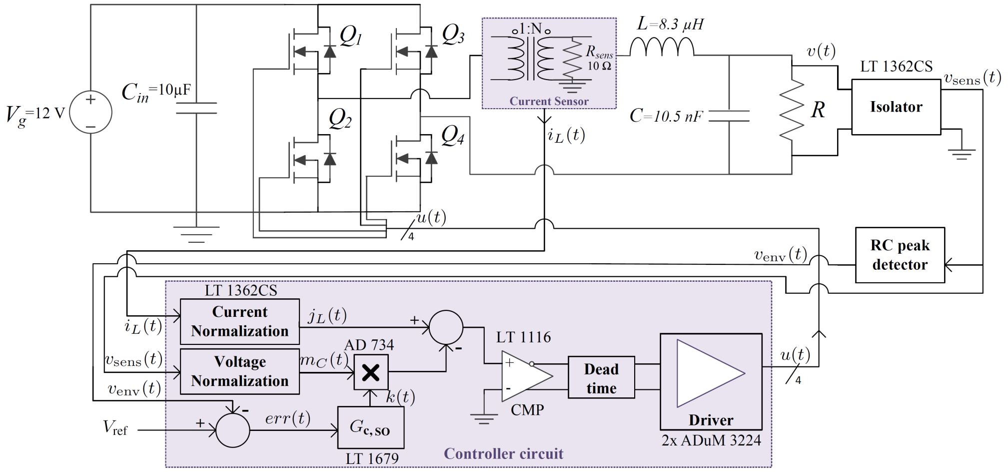

Figure 4.19: Scheme of a parallel resonant converter with the proposed switching angle controller.

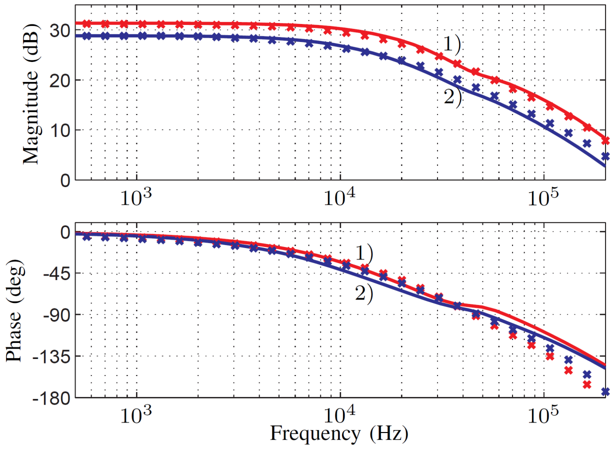

Figure 4.20: Comparison between the proposed model and experimental results for two different switching frequencies and loads: 1) 520 kHz/420 Ω, 2) 515 kHz/650 Ω. Solid-line: analytical model. X marks: experimental measurements.

Closed-loop responses

In Figs. 4.21 and 4.22, waveforms under load and input line variation are shown respectively. Again, the AC output voltage envelope is $V_{\text{env}} = 160$ V and the input voltage is $V_{\text{g}} = 12$ V. The AC voltage has been enlarged and its envelope outlined for easy comparison with the simulation results. Transients have been carried out by means of a standard relay controlled by an external signal generator.

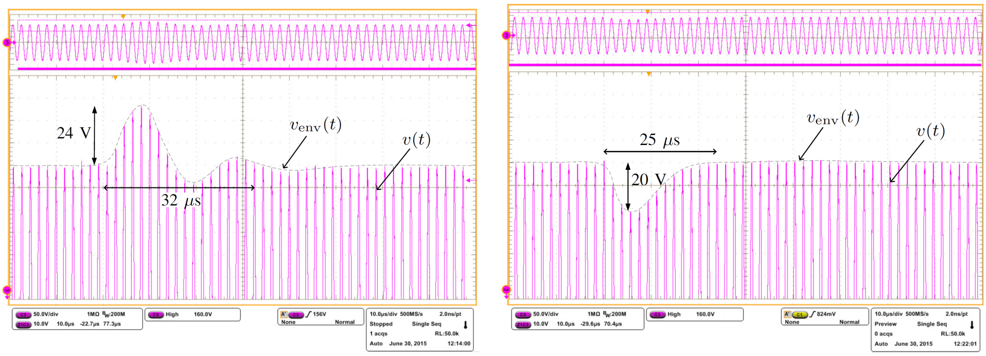

(a) $R = 420\ \Omega \rightarrow 650\ \Omega$ **(b)** $R = 650\ \Omega \rightarrow 420\ \Omega$

Figure 4.21: Output voltage measurement under load variations (V_{g}= 12 V).

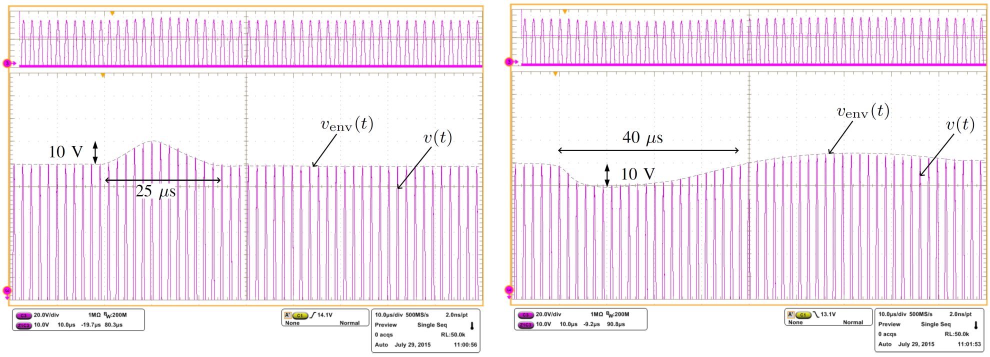

(a) $V_{\mathrm{g}} = 12\ \mathrm{V} \rightarrow 14\ \mathrm{V}$ **(b)** $V_{\mathrm{g}} = 14\ \mathrm{V} \rightarrow 12\ \mathrm{V}$

Figure 4.22: Output voltage measurement under input voltage variations (R= 420 Ω).

An excellent agreement can be observed between the solid lines of Figs. 4.17 and 4.18, and the waveforms in Figs. 4.21 and 4.22. This verifies the correctness of the analytic derivations and the good performance of the proposed control approach. Therefore, the switching angle controller offers better rejection ratios and reduced settling times than its FM counterparts and is able to keep the output voltage stable under a wider range of loads.

Start-up responses

Fig. 4.23 shows the output voltage start-up responses under no load conditions, static load of 420 Ω and static load of 650 Ω.

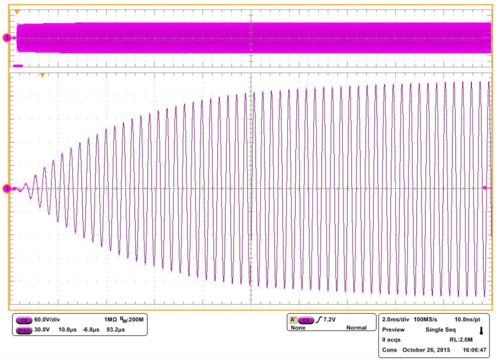

(a) No load conditions

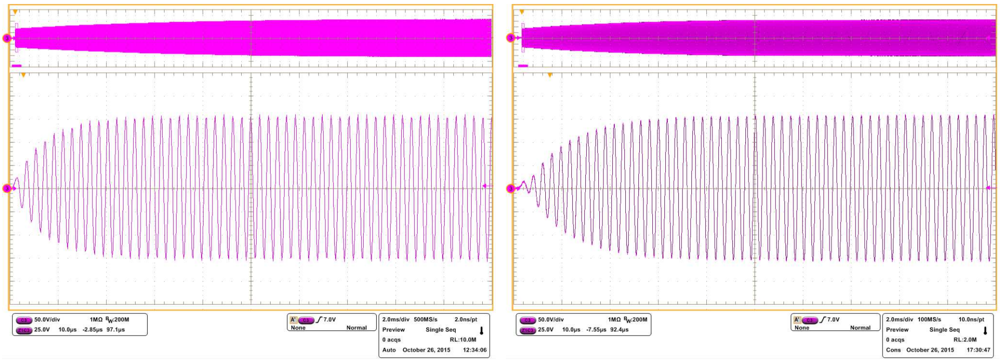

(b) $R = 420\ \Omega$ **(c)** $R = 650\ \Omega$

Figure 4.23: Startup waveforms of the output voltage for different loads. Top waveform (contracted): 60 V/div, 2 ms/div. Bottom waveform (enlarged): 30 V/div, 10 μs/div.

In Fig. 4.23a it is demonstrated that the converter can start and operate without any load at the output, guaranteeing that any temporary loss of the load will not damage the circuit. Moreover, in the case of 420 Ω and 650 Ω loads, it is shown a fast start-up response of 20 μs and 30 μs respectively, where the output voltage reach 50% of the nominal value (160 V). After that, a dynamic slow-response appears until the desired output voltage is reached, with a duration of 10 ms and 9 ms respectively. As predicted by the proposed model, larger loads correspond to lower DC gains of the control-to-output transfer function and, consequently, to narrower control bandwidths and increased settling times.

It is worth to remark that the switching angle controller allows the soft-start of the circuit without need of including any additional devices, specific starting circuit or startup control laws.

4.5 Summary

In this chapter a new modeling technique for self-oscillating resonant converters has been presented. Specific static and dynamic models for the PRC and the SRC have been obtained and described in detail, leading to a novel complete model for 2nd order self-oscillating resonant converters. Afterwards, an output voltage controller for the PRC has been synthesized with the complete model and verified by simulation and experimentally. The switching angle controller regulates the output voltage by varying the parameter k of the voltage control switching law presented in Chapter 2 ($u = sg(j_L - k(t)m_C)$). Besides, the response obtained with this new switching angle controller has been compared with the behavior of two different standard FM controllers, demonstrating the benefits of the proposed approach.

5

CHAPTER 5

THIRD ORDER RESONANT STRUCTURES: ANALYSIS, DESIGN AND APPLICATIONS

In this chapter, the generation of a three-dimensional limit cycle in 3rd order resonant converters is analyzed. In the proposed approach, the three state-variables are associated in two phase-planes, and each individual plane is analyzed separately. Then, the resulting expressions are combined in order to obtain a description of the behavior of all the state-variables.

With that methodology, the restrictions for the existence of self-oscillation are determined with exactitude in a 3rd order circuit and the unconditional stability of the system is demonstrated.

As a result, a simple design procedure for 3rd order self-oscillating converters is introduced, which leads to a desired self-oscillating response. A practical application based on a self-oscillating LCC converter is designed following the previous procedure and its performance is verified by simulation and experimentally.

5.1 Determination of amplitude and period in the limit cycle

The analysis that follows is exemplified with the LCC resonant converter, although it can be extended to the LLC. The power stage of a LCC converter and its corresponding equivalent circuit are shown in Figs. 5.1a and 5.1b respectively. Transfer functions $H(s)$ and $Y(s)$ relating respectively input to output voltage and inductor current to input voltage (input admittance) are defined as

$$H(s) = \frac{v_{Cp}(s)}{v_s(s)} = \frac{{}^{s}/_{LC_p}}{s^3 + \frac{s^2}{RC_p} + \frac{C_s+C_p}{LC_sC_p}s + \frac{1}{LC_sC_pR}} \tag{5.1}$$

$$Y(s) = \frac{1}{Z_i(s)} = \frac{i_L(s)}{v_s(s)} = \frac{\frac{1}{LC_pR}s(C_pR\,s+1)}{s^3 + \frac{s^2}{RC_p} + \frac{C_s+C_p}{LC_sC_p}s + \frac{1}{LC_sC_pR}} \tag{5.2}$$

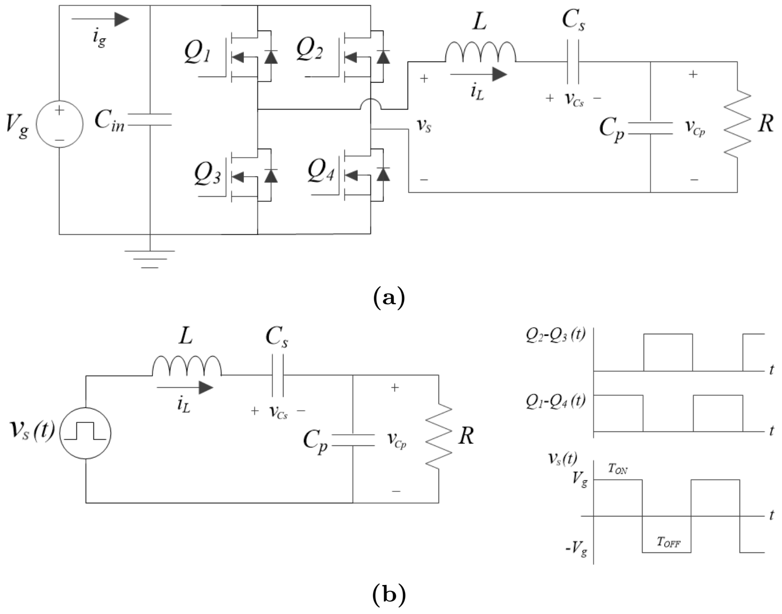

(a)

(b)

Figure 5.1: (a) Power stage of the LCC resonant converter. (b) Equivalent circuit.

In order to describe analytically the generation of a three-dimensional spiral that eventually converges into a limit cycle, three hypotheses on the poles of the system will be assumed, their justification being given in the following subsections.

Hypothesis 1: It is assumed that the poles of the system consist of one negative real pole and two complex conjugates poles with negative real part due to the

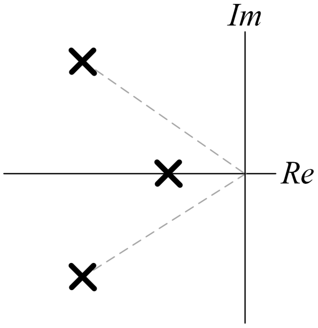

Figure 5.2: Pole-zero diagram of the LCC expected by hypothesis 1.

passive nature of the circuit, as depicted in Fig. 5.2.

Under this assumption, (5.3) holds. Unknown parameters include α, ξ and ω_0.

$$s^3 + \frac{s^2}{RC_p} + \frac{C_s + C_p}{LC_sC_p}s + \frac{1}{LC_sC_pR} = (s+\alpha)(s^2 + 2\xi\omega_0 s + \omega_0^2) \qquad (5.3)$$

5.1.1 Analysis in a generic T_{on} interval

Two different focuses can be obtained in a LCC resonant converter depending on the structure of the system: a positive one, defined by $(i_L*, v_{Cs}*, v_{Cp}*) = [0, V_g, 0]$ for $v_s = V_g$, and a negative one, defined by $(i_L*, v_{Cs}*, v_{Cp}*) = [0, -V_g, 0]$ for $v_s = -V_g$. Thus, if the simple control law presented in Chapter 2 ($u = sg(i_L)$) is applied, a three-dimensional spiral that becomes an ellipse at the limit cycle can be obtained. Fig. 5.3 shows the generation of a limit cycle under such conditions.

In this analysis, the projection in two planes of the three-dimensional trajectory in Fig. 5.3 will be analyzed separately and the resulting equations will be combined later in order to obtain a description of the amplitude and period of the limit cycle. An example of the associated plane formed by the inductor current and the parallel capacitor voltage is depicted in Fig. 5.4. As it can be seen, variable $v_{Cp_{2n}}$ symbolizes the voltage amplitude at switching instants from negative to positive current in this phase-plane, while variable $v_{Cs_{2n}}$ symbolizes the same situation in the phase-plane $i_L - v_{Cs}$. Similarly, variables $v_{Cp_{2n+1}}$ and $v_{Cs_{2n+1}}$ symbolize the opposite situation in each corresponding phase-plane, with n increasing after a complete cycle (n=1,2,3,...). Note that in the limit cycle the notation is in capital letters and without dependency on n (i.e., V_{Cp} and V_{Cs}).

Assuming that the converter is in the T_{on} interval with initial conditions $v_{Cs}(t_K) = -v_{Cs_{2n}}$, $i_L(t_K) = 0$, $v_{Cp}(t_K) = -v_{Cp_{2n}}$, where t_K is the initial instant of such interval, then the input voltage will be $v_{in}(t) = V_g$. Since the free-response

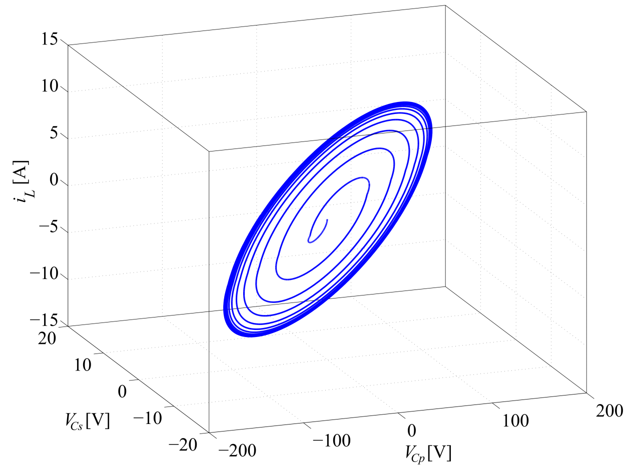

Figure 5.3: Three-dimensional trajectory representation of the LCC converter.

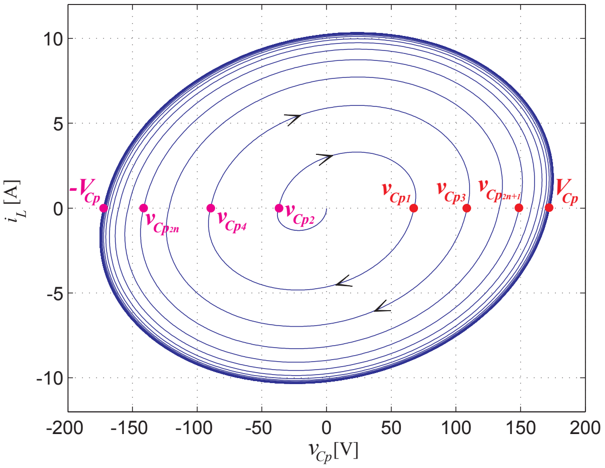

Figure 5.4: Trajectory representation of the LCC converter in the phase-plane $i_L - v_{Cp}$.

of the circuit is given by $Ae^{-\alpha t}+Be^{-\xi\,\omega_0\,t}\sin\,\omega_d\tau+Ce^{-\xi\,\omega_0\,\tau}\cos\omega_d t$, the expression of the series capacitor voltage will be

$$v_{Cs}(\tau) = Ae^{-\alpha\tau} + Be^{-\xi\,\omega_0\,\tau}\sin\,\omega_d\tau + Ce^{-\xi\,\omega_0\,\tau}\cos\omega_d\tau + V_g \qquad (5.4)$$

where $\omega_d = \omega_0\sqrt{1-\xi^2}$, $\tau = t - t_K$ and A, B, C are constants corresponding to the solution of the homogeneous differential equation of the system.

On the other hand, since $v_L(t) = L\, di_L/dt$ and $i_L(t) = C_s\, dv_{Cs}/dt$, the inductor current and voltage will be expressed as

$$\begin{aligned} i_L(\tau) &= -C_s A\alpha e^{-\alpha\tau} - C_s e^{-\xi\omega_0\tau}(B\xi\omega_0 + C\omega_d)\ \sin\,\omega_d\tau + \\ &+ C_s e^{-\xi\omega_0\tau}(B\omega_d - C\xi\omega_0)\cos\omega_d\tau \end{aligned} \tag{5.5}$$

$$\begin{aligned} v_L(\tau) &= LC_sA\alpha^2 e^{-\alpha\tau} + (-2LC_s\, B\,\xi\,\omega_0\,\omega_d + LC_sC\xi^2\omega_0^2 - \\ &- LCC_s\omega_d^2)e^{-\xi\omega_0\tau}\cos\omega_d\tau + (LC_sB\xi^2\omega_0^2 - LC_sB\omega_d^2 + \\ &+ 2LC_sC\xi\omega_d\omega_0)e^{-\xi\omega_0\tau}\ \sin\,\omega_d\tau \end{aligned} \tag{5.6}$$

Moreover, parallel capacitor voltage is the difference between the voltages previously described:

$$v_{Cp}(t) = V_g - v_{Cs}(t) - v_L(t) \tag{5.7}$$

Besides, at the beginning of the interval (i.e. $t = t_K$), or equivalently at $\tau = 0$, it can be written that

$$\frac{dv_{Cs}(0)}{dt} = \frac{i_L(0)}{C_s} = 0 \tag{5.8}$$

In addition, if expression (5.6) is particularized at initial instant ($\tau = 0$) it is found that

$$\begin{aligned} v_L(0) &= LC_sA\alpha^2 - 2LC_sB\xi\omega_0\omega d + LC_sC\xi^2\omega_0^2 - LCC_s\omega_d^2 = \\ &= V_g + v_{Cs_{2n}} + v_{Cp_{2n}} \end{aligned} \tag{5.9}$$

Since ${\omega_d}^2 = {\omega_0}^2(1-\xi^2)$, (5.9) becomes

$$A\alpha^2 - 2B\xi\omega_0\omega_d + C\omega_0^2(2\xi^2 - 1) = \frac{V_g + v_{Cs_{2n}} + v_{Cp_{2n}}}{LC_s} \tag{5.10}$$

Moreover, particularizing expression (5.4) at $\tau = 0$ and introducing relationship (5.8) result in

$$v_{Cs}(0) = A + C + V_g = -v_{Cs_{2n}} \tag{5.11}$$

$$\frac{dv_{Cs}(0)}{dt} = \frac{i_L(0)}{C_s} = 0 = -A\alpha + B\omega_d - C\xi\omega_0 \tag{5.12}$$

Finally, expressions (5.10), (5.11) and (5.12) can be compacted as follows:

$$\begin{pmatrix} 1 & 0 & 1 \\ -\alpha & \omega_d & -\xi\,\omega_0 \\ \alpha^2 & -2\xi\,\omega_0\,\omega_d & \omega_0^2\,(2\xi^2-1) \end{pmatrix} \begin{pmatrix} A \\ B \\ C \end{pmatrix} = \begin{pmatrix} -V_g - v_{Cs_{2n}} \\ 0 \\ \frac{V_g + v_{Cs_{2n}} + v_{Cp_{2n}}}{LC_s} \end{pmatrix} \tag{5.13}$$

Solving (5.13) for A, B and C, yields

$$A = \frac{1}{\Delta}\left((V_g + v_{Cs_{2n}})\,\omega_0^2 - \frac{V_g + v_{Cs_{2n}} + v_{Cp_{2n}}}{LC_s}\right), \tag{5.14}$$

$$B = \frac{1}{\omega_d\Delta}\left(\begin{array}{l} \frac{V_g + v_{Cs_{2n}} + v_{Cp_{2n}}}{LC_s}(\xi\omega_0 - \alpha) + \\ + (V_g + v_{Cs_{2n}})\omega_0\alpha(\xi\alpha - 2\xi^2\omega_0 + \omega_0) \end{array}\right), \tag{5.15}$$

$$C = \frac{1}{\Delta}\left(\frac{V_g + v_{Cs_{2n}} + v_{Cp_{2n}}}{LC_s} - (V_g + v_{Cs_{2n}})(2\xi\omega_0\alpha - \alpha^2)\right), \tag{5.16}$$

where $\Delta = \omega_0^2\,(2\xi^2-1) - 2\xi^2\,{\omega_0}^2\,\omega_d + 2\xi\,\omega_0\,\omega_d\alpha - \omega_d\alpha^2 = \omega_d\left[2\xi\omega_0\alpha - \alpha^2 - {\omega_0}^2\right]$.

Besides, T_{on} interval will end at instant τ_0 for which $i_L(\tau_0) = 0$. Substituting it in equation (5.5) leads to:

$$\begin{aligned} A\alpha e^{-\alpha\tau_0} &= e^{-\xi\omega_0\tau_0}\left((B\xi\omega_0 + C\omega_d)\,\sin\,\omega_d\tau_0 + \right. \\ &\left. + (B\omega_d - C\xi\omega_0)\cos\omega_d\tau_0\right) \end{aligned} \tag{5.17}$$

A second hypothesis is now considered in order to find the value of τ_0 satisfying equation (5.17).

Hypothesis 2: It is assumed that the time constant associated to α is much larger than the time constant associated to $\xi\omega_0$, i.e., α is the dominant pole of the system, as depicted in Fig. 5.5.

This hypothesis implies that the term $Ae^{-\alpha\tau}$ will be practically constant along the generic T_{on} interval, and therefore its time derivative will be approximately zero in such interval. Note that this fact is equivalent to impose $\alpha = 0$ in (5.9) - (5.17). Hence, (5.17) can be expressed as follows:

$$e^{-\xi\omega_0\tau_0}\left((B\xi\omega_0 + C\omega_d)\sin\,\omega_d\tau_0 + (B\omega_d - C\xi\omega_0)\cos\omega_d\tau_0\right) = 0 \tag{5.18}$$

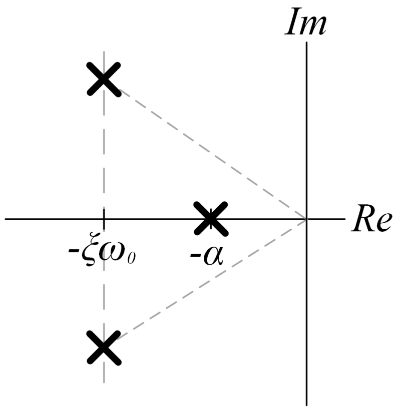

Figure 5.5: Pole-zero diagram of the LCC resulting from the application of hypothesis 2.

whose solution is

$$\omega_d \tau_0 = \arctan\left(\frac{C\xi\omega_0 - B\omega_d}{B\xi\omega_0 + C\omega_d}\right) + \pi \tag{5.19}$$

In addition, imposing $\alpha = 0$ in (5.15) and (5.16) results in

$$B\omega_d \mid_{\alpha=0} = \frac{-(V_g + v_{Cs_{2n}} + v_{Cp_{2n}})(\xi\omega_0)}{LC_s\omega_0^2} \tag{5.20}$$

$$B\xi\omega_d \mid_{\alpha=0} = \frac{-(V_g + v_{Cs_{2n}} + v_{Cp_{2n}})(\xi\omega_0)\xi^2}{LC_s\omega_0^2} \tag{5.21}$$

$$C \mid_{\alpha=0} = \frac{-V_g + v_{Cs_{2n}} + v_{Cp_{2n}}}{LC_s\omega_0^2} \tag{5.22}$$

$$C\omega_d \mid_{\alpha=0} = \frac{-V_g + v_{Cs_{2n}} + v_{Cp_{2n}}}{LC_s\omega_0^2}\omega_d \tag{5.23}$$

Therefore, replacement of (5.20) - (5.23) in equation (5.19) leads to

$$\omega_d \tau_0 = \arctan\left(\frac{0}{\frac{-(V_g+v_{Cs_{2n}}+v_{Cp_{2n}})\xi^2}{LC_s\omega_d} + \frac{-V_g+v_{Cs_{2n}}+v_{Cp_{2n}}}{LC_s\omega_0^2}\omega_d}\right) + \pi = \pi \tag{5.24}$$

such that τ_0 can be written as

$$\tau_0 = \frac{\pi}{\omega_d} \tag{5.25}$$

5.1.2 Signal amplitude in the limit cycle

Note that at this point, a generic T_{on} interval of the system has been analyzed. Now, the analysis assumes steady-state conditions, such that the initial and final values of the variables can be established considering symmetric trajectories forming the ellipse of the limit cycle. Then, variables $v_{Cs_{2n}}$ and $v_{Cp_{2n}}$ are substituted by V_{Cp} and V_{Cs} denoting their steady-state value.

Assuming that τ_0 is the duration of T_{on} interval in the limit cycle, it is possible to establish that $v_{Cs}(\tau_0) = V_{Cs}$ due to the symmetry of the limit cycle associated to the phase-plane i_L - v_{Cs}, and in consequence, (5.4) can be defined as

$$v_{Cs}(\tau_0)|_{\alpha=0} = Ae^{-\alpha\tau_0}|_{\alpha=0} + B|_{\alpha=0}e^{-\xi\pi}\sin\pi + C|_{\alpha=0}e^{-\xi\pi}\cos\pi + V_g = V_{Cs} \tag{5.26}$$

and from this previous expression, noting that sin $\pi = 0$,

$$A|_{\alpha=0} - C|_{\alpha=0}e^{-\xi\pi} + V_g = V_{Cs} \tag{5.27}$$

Applying $\alpha = 0$ in (5.14) allows to obtain

$$A|_{\alpha=0} = -(V_g + V_{Cs}) + \frac{V_g + V_{Cs} + V_{Cp}}{LC_s\omega_0^2} \tag{5.28}$$

and substituting the values of A and C given by expressions (5.28) and (5.22) in (5.27) leads to

$$-(V_g + V_{Cs}) + \frac{V_g + V_{Cs} + V_{Cp}}{LC_s\omega_0^2} + \frac{V_{Cs} + V_{Cp}}{LC_s\omega_0^2}e^{-\xi\pi} + V_g = V_{Cs} \tag{5.29}$$

which can be simplified as

$$V_g\left(\frac{1 + e^{-\xi\pi}}{LC_s\omega_0^2}\right) = V_{Cs}\left(\frac{2LC_s\omega_0^2 - 1 - e^{-\xi\pi}}{LC_s\omega_0^2}\right) - V_{Cp}\left(\frac{1 + e^{-\xi\pi}}{LC_s\omega_0^2}\right) \tag{5.30}$$

Finally, from (5.30) the following relationship between the input voltage V_g and the voltages of the series and parallel capacitors V_{Cs2n} and V_{Cp2n} is obtained:

$$V_g(1 + e^{-\xi\pi}) = V_{Cs}(2LC_s\omega_0^2 - 1 - e^{-\xi\pi}) - V_{Cp}(1 + e^{-\xi\pi}) \tag{5.31}$$

Similarly, if the limit cycle corresponding to the phase plane $i_L - v_{Cp}$ is considered, the following condition will be satisfied,

$$v_{Cp}(\tau_0) = V_{Cp} \tag{5.32}$$

where V_{Cp} can be substituted by (5.7), leading to

$$v_{Cp}(\tau_0) = V_g - v_{Cs}(\tau_0) - v_L(\tau_0) = V_g - V_{Cs} - v_L(\tau_0) \tag{5.33}$$

Following equation (5.6) and applying $\omega_d\tau_0 = \pi$, v_L can be expressed as

$$v_L(\tau_0)|_{\alpha=0} = 2LC_s\xi\omega_0\omega_d B|_{\alpha=0}e^{-\xi\pi} + LC_s C|_{\alpha=0}e^{-\xi\pi}(\omega_d^2 - \xi^2\omega_0^2) \tag{5.34}$$

In order to describe the system as a function of α, ξ and ω_0, a third hypothesis is introduced.

Hypothesis 3: A very small damping factor is assumed, namely $\xi << 1$, which allows to consider that the natural oscillation frequency ω_0 and the damped natural oscillation frequency ω_d are approximately equal.

Under this assumption, and introducing (5.34) into (5.33) and (5.33) into (5.32), a final expression relating the input voltage V_g and the voltages of the series and parallel capacitors V_{Cs} and V_{Cp} for the phase-plane $i_L - v_{Cp}$ is obtained:

$$V_g(1 + e^{-\xi\pi}) = V_{Cs}(1 - e^{-\xi\pi}) + V_{Cp}(1 - e^{-\xi\pi}) \tag{5.35}$$

Therefore, equations (5.31) and (5.35) can be expressed in matrix form as follows:

$$\begin{pmatrix} 2LC_s\omega_0^2 - 1 - e^{-\xi\pi} & -1 - e^{-\xi\pi} \\ 1 - e^{-\xi\pi} & 1 - e^{-\xi\pi} \end{pmatrix} \begin{pmatrix} V_{Cs} \\ V_{Cp} \end{pmatrix} = \begin{pmatrix} V_g(1 + e^{-\xi\pi}) \\ V_g(1 + e^{-\xi\pi}) \end{pmatrix} \tag{5.36}$$

Solving (5.36) for V_{Cs} and V_{Cp} yields the capacitor voltage amplitudes in the limit cycle:

$$V_{Cs} = \frac{V_g(1 + e^{-\xi\pi})}{LC_s\omega_0^2(1 - e^{-\xi\pi})} \tag{5.37}$$

$$V_{Cp} = \frac{V_g(1 + e^{-\xi\pi})(LC_s\omega_0^2 - 1)}{LC_s\omega_0^2(1 - e^{-\xi\pi})} = V_{Cs}(LC_s\omega_0^2 - 1) \tag{5.38}$$

Now, identifying ω_0 and ξ in terms of the converter parameters is mandatory in order to establish a design procedure.

5.1.3 Determination of the oscillation frequency in the limit cycle

The difference of magnitude between the time constants associated to α and $\xi\omega_0$ has allowed to establish the duration τ_0 of a generic T_{on} interval. The subsequent particularization in the case of the limit cycle permits to conclude that the period of the limit cycle is $2\tau_0$ due to the cycle symmetry, and that the angular oscillation frequency is the damped natural oscillation ω_d. Besides, the hypothesis of small damping factor has led to equate the damped natural oscillation frequency with the natural oscillation frequency ω_0.

Now, the frequency for which the input impedance exhibits a resistive behavior is determined in order to express the limit cycle oscillation frequency in terms of the circuit parameters.

From (5.2), the expression of the input impedance is derived as:

$$Z_{in}(s) = \frac{1}{Y(s)} = \frac{LRC_pC_ss^3 + LC_ss^2 + R(C_s + C_p)s + 1}{C_s(1 + RC_ps)s} \tag{5.39}$$

and particularizing (5.39) in $s = j\omega_0$ yields to

$$\begin{aligned} Z_{in}(j\omega_0) &= \frac{-jLRC_pC_s\omega_0{}^3 - LC_s\omega_0{}^2 + jR(C_s + C_p)\omega_0 + 1}{jC_s(1 + jRC_p\omega_0)\omega_0} = \\ &= \frac{1 - LC_s\omega_0^2}{jC_s\omega_0\,(1 + jRC_p\omega_0)} \end{aligned} \tag{5.40}$$

Assuming that natural oscillation frequency ω_0 is given by

$$\omega_0 = \sqrt{\frac{C_s + C_p}{LC_sC_p}} \tag{5.41}$$

expression (5.40) becomes

$$\begin{aligned} Z_{in}(j\omega_0) &= \frac{1 - \frac{C_p + C_s}{C_s}}{jC_s\omega_0\,(1 + jRC_p\omega_0)} = \\ &= \frac{-1}{jC_p\omega_0(1 + jRC_p\omega_0)} \end{aligned} \tag{5.42}$$

Therefore, if the parameters R, C_p and ω_0 fulfill the following condition

$$RC_p\omega_0 >> 1\,, \tag{5.43}$$

where $RC_p\omega_0$ is the Q value of the parallel capacitor, the input impedance will be resistive, leading to the following expression:

$$Z_{in}(j\omega_0) = \frac{1}{R{C_p}^2{\omega_0}^2} \tag{5.44}$$

Similarly, introducing condition (5.43) in (5.1) yields to

$$H(j\omega_0) = -jRC_p\omega_0 \tag{5.45}$$

Under these conditions, if the input voltage is approximated by its first harmonic, i.e.$v_s(t) \approx v_{s1}(t) = V_m \cos\omega_0 t$, where $V_m = 4V_g/\pi$, the expressions of inductor current and parallel capacitor voltage will be given by

$$i_L(t) = V_m \frac{RC_p(C_s+C_p)}{LC_s} \cos\omega_0 t \tag{5.46}$$

$$v_{Cp}(t) = V_m\, \omega_0 C_p\, R \,\sin\, \omega_0 t \tag{5.47}$$

From (5.46) and (5.47) it can be concluded that the LCC behavior under these conditions is similar to that of the PRC at the resonant frequency. Moreover, condition (5.43) allows to consider that the capacitors are connected in series, so that their respective voltages are proportional, i.e., they are in phase. Thus, taking into account the relationship established in (5.38), it is found that

$$\frac{V_{Cs}}{V_{Cp}} = \frac{1}{LC_s\omega_0^2 - 1} = \frac{1}{\frac{C_s+C_p}{C_p} - 1} = \frac{C_p}{C_s} \tag{5.48}$$

or equivalently

$$v_{Cs}(t) = \frac{C_p}{C_s} v_{Cp}(t) = V_m\omega_0 \frac{{C_p}^2}{C_s} R \,\sin\, \omega_0 t \tag{5.49}$$

It can be also verified that the maximum value of expression (5.49) coincides with (5.38), which verifies the validity of the previous expressions.

5.1.4 Establishment of damping ratio ξ

Identification of the coefficients of the third order polynomial in (5.3) results in the following set of equations:

$$\frac{1}{RC_p} = 2\xi\omega_0 + \alpha \tag{5.50}$$

$$\frac{C_s + C_p}{LC_sC_p} = \omega_0^2 + 2\xi\omega_0\alpha \tag{5.51}$$

$$\frac{1}{LRC_sC_p} = \alpha\omega_0^2 \tag{5.52}$$

Simultaneous fulfillment of (5.41) and (5.51) implies that the constraint $\omega_0 >> 2\xi\alpha$ must be satisfied. Hence, α can be derived from (5.52) as

$$\alpha = \frac{1}{R(C_s + C_p)} \tag{5.53}$$

Introducing (5.53) into (5.50) leads to

$$2\xi\omega_0 = \frac{C_s}{C_p}\frac{1}{R(C_s + C_p)} = K_C\alpha \tag{5.54}$$

where $K_C = \frac{C_s}{C_p}$, so that

$$\xi\omega_0 = \frac{K_C\alpha}{2} \tag{5.55}$$

As it can be seen in expression (5.55), the accomplishment of the pole separation hypothesis only depends on parameter K_C. Therefore, the selection of a high K_C ratio in the design stage is only required in order to accomplish hypothesis 2, guaranteeing that the subsequent predictions on amplitude and frequency of the limit cycle will be valid. A minimum K_C of 8 is established, since this value implies a time constant associated to α 4 times higher than the time constant associated to $\xi\omega_0$. Lower values of K_C does not guarantee the accomplishment of the restriction, as the effect of α can not be neglected.

Finally, the damping factor can be expressed in terms of K_C as,

$$\xi = \frac{K_C}{2(K_C + 1)RC_p}\sqrt{\frac{K_CLC_p}{K_C + 1}}. \tag{5.56}$$

5.1.5 Simulation results

In order to verify the previous calculations, a simulation of a LCC converter has been carried out. The converter has the following parameters: $V_g = 24$ V, $L = 16\,\mu$H, $C_s = 500$ nF, $C_p = 50$ nF, $R = 100\,\Omega$. Fig. 5.6 displays the time domain waveforms, while Fig. 5.7 depicts the limit cycle generation in the planes $i_L - v_{Cs}$ and $i_L - v_{Cp}$. These results are in perfect agreement with the theoretical predictions, confirming the validity of the previous analysis. It is worth mentioning that the roots of the characteristic polynomial (5.3) for the previous set of parameters are located in -18200 and $-90,9 \times 10^3 \pm j\,1167,7 \times 10^3$ rad/s, which is in perfect agreement with the values predicted by expressions (5.41), (5.53) and (5.56). Besides, from the observation of the waveforms of Fig. 5.6, it can be deduced that the oscillation frequency is $f_0 = 187$ kHz, i.e. $\omega_0 = 11.7 \times 10^5$ rad/s, which is exactly the value predicted by expression (5.41). The maximum values of voltages $v_{Cs}(t)$ and $v_{Cp}(t)$ in Fig. 5.6 are $V_{Cs} = 18$ V and $V_{Cp} = 180$ V, which coincides with the values predicted by (5.37) and (5.38) as well as with those provided by (5.47) and (5.49) respectively. Note that voltages in both capacitors are proportional, as predicted by the analysis presented in Section 5.1.3.

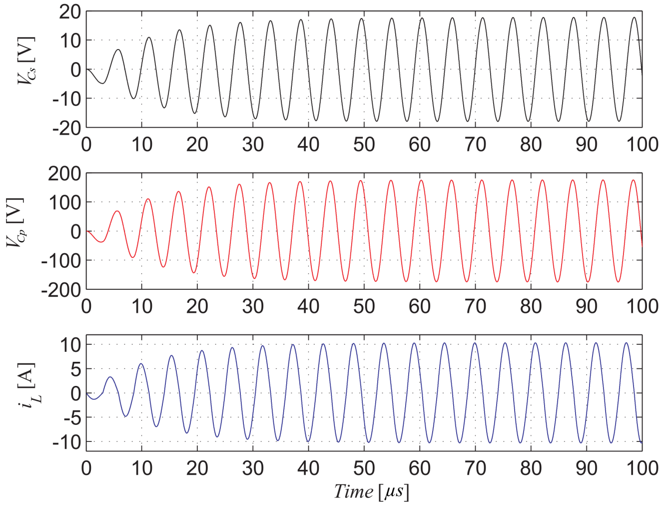

Figure 5.6: Simulated time-domain waveforms of the inductor current and capacitor voltages in the self-oscillating LCC described in Section 5.1.5.

5.1.6 Experimental validation

With the aim of validating the previous calculations, an experimental prototype of the LCC resonant converter has been implemented taking into account the set of parameters employed in the previous simulations and the control law $u = sg(i_L)$.

Fig. 5.8 shows the scheme of the implemented prototype. The power stage consists of an H-bridge connected to a resonant tank. The bridge uses 4 MOSFETs (IPB200N15N3) activated by a stage based on driver UCC27211. The steady-state waveforms of current and output voltage of the LCC resonant converter in self-oscillating operation are shown in Fig. 5.9a. The circuit exhibits an oscillation

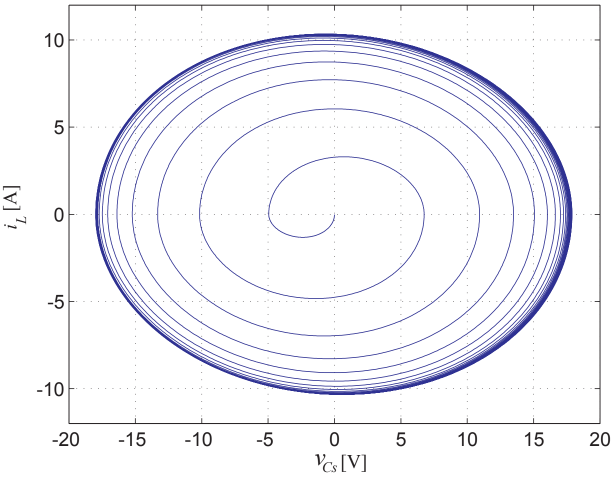

(a)

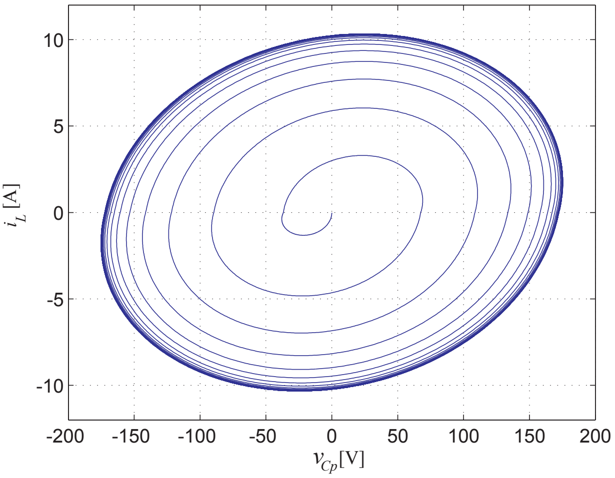

(b)

Figure 5.7: Simulation of the limit cycle generation in a self-oscillating LCC resonant converter: (a) phase-plane $i_L - v_{Cs}$, (b) phase-plane $i_L - v_{Cp}$.

frequency of 180 kHz generating an output voltage of 175 V and supplying 130 W to the load with an efficiency of 86%. Fig. 5.9b illustrates the corresponding generation of the limit cycle. It can be observed that Figs. 5.9a and 5.9b agree with the simulation results depicted in Figs. 5.6 and 5.7b. A comparison between the predicted and experimental values can be seen in Table 5.1, showing a good agreement between them. The propagation delay has been mitigated by selecting a high-speed driver, resulting in 70 ns delay, and a relatively low switching frequency.

Table 5.1: Comparison between expected values and experimental results obtained at steady-state in Section 5.1.6

Parameter	Theoretical value	Experimental value
f_0	186.2 kHz	180 kHz
$v_{Cp,peak}$	180 V	175 V
$i_{L,peak}$	10.5 A	10.5 A

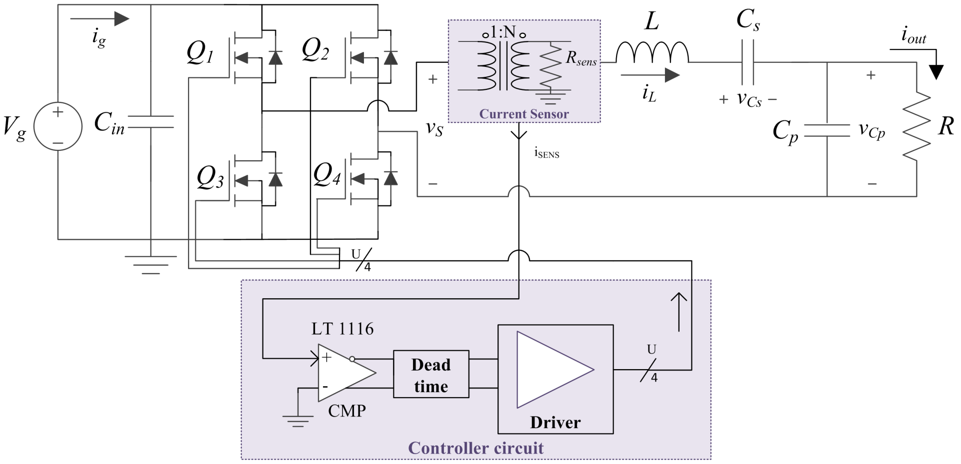

Figure 5.8: Experimental self-oscillating LCC converter.

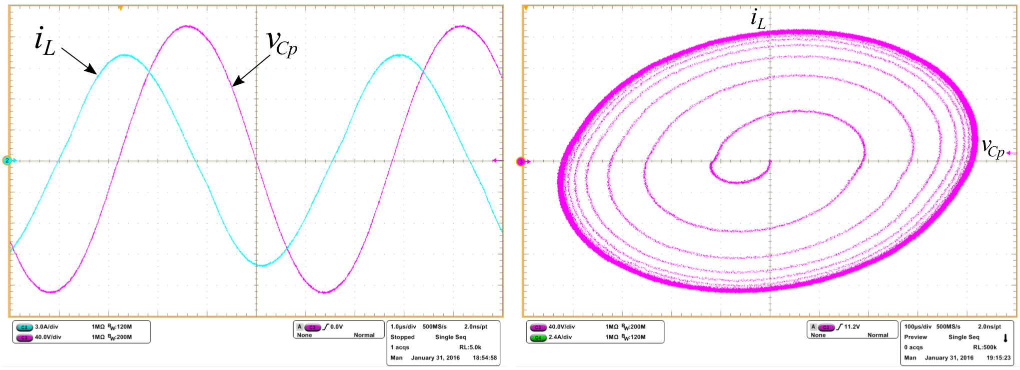

(a)

(b)

Figure 5.9: Experimental results of the self-oscillating LCC: (a) time-domain waveforms i_L and v_P, (b) limit cycle generation in the phase-plane $i_L - v_P$.

5.2 Stability analysis

In the previous section, the frequency and amplitude of the limit cycle have been obtained. However, the convergence of the spiral into an elliptical limit cycle has to be ensured or, equivalently, the parametric conditions for such convergence have to be found. With this purpose, the generation mechanism is described now by means of a discrete-time model established by the zero current crossings in each phase plane.

Taking into account the analysis made in Section 5.1.1 and the description of the system provided by equations (5.22), (5.27) and (5.28), a generic T_{off} interval in the phase-plane $i_L - v_{Cs}$ of Fig. 5.7a can be described as

$$v_{Cs_{2n}} = v_{Cs_{2n-1}} + \frac{-V_g - v_{Cs_{2n-1}} - v_{Cp_{2n-1}}}{LC_s\omega_0^2} + \frac{-V_g - v_{Cs_{2n-1}} - v_{Cp_{2n-1}}}{LC_s\omega_0^2}e^{-\xi\pi} \tag{5.57}$$

$$v_{Cs_{2n}} = -V_g\frac{1+e^{-\xi\pi}}{LC_s\omega_0^2} + v_{Cs_{2n-1}}\left(1 - \frac{1+e^{-\xi\pi}}{LC_s\omega_0^2}\right) - v_{Cp_{2n-1}}\frac{1+e^{-\xi\pi}}{LC_s\omega_0^2} \tag{5.58}$$

Equivalently, a generic T_{off} interval in the phase-plane $i_L - v_{Cp}$ of Fig. 5.7b can be described as

$$v_{Cp_{2n}} = -V_g(1+e^{-\xi\pi}) + v_{Cs_{2n-1}}(1-e^{-\xi\pi}) - v_{Cp_{2n-1}}e^{-\xi\pi} \tag{5.59}$$

Moreover, the following T_{on} interval in each situation will be characterized by the next equations:

$$v_{Cs_{2n+1}} = V_g\frac{1+e^{-\xi\pi}}{LC_s\omega_0^2} + v_{Cp_{2n}}\left(1 - \frac{1+e^{-\xi\pi}}{LC_s\omega_0^2}\right) - v_{Cp_{2n}}\frac{1+e^{-\xi\pi}}{LC_s\omega_0^2} \tag{5.60}$$

$$v_{Cp_{2n+1}} = V_g(1+e^{-\xi\pi}) + v_{Cp_{2n}}(1-e^{-\xi\pi}) - v_{Cp_{2n}}e^{-\xi\pi} \tag{5.61}$$

Introducing (5.58) and (5.59) in (5.60) and (5.61), the subsequent discrete-time model can be obtained after simplification:

$$\begin{pmatrix} v_{Cs_{2n+1}} \\ v_{Cp_{2n+1}} \end{pmatrix} = \begin{pmatrix} \phi_{11} & \phi_{12} \\ \phi_{21} & \phi_{22} \end{pmatrix} \begin{pmatrix} v_{Cs_{2n}} \\ v_{Cp_{2n}} \end{pmatrix} + \begin{pmatrix} \Gamma_1 \\ \Gamma_2 \end{pmatrix} V_g \tag{5.62}$$

with

$$\begin{aligned}\phi_{11} &= \left(1-\frac{1+e^{-\xi\pi}}{LC_s\omega_o^2}\right)^2-\frac{1-e^{-2\xi\pi}}{LC_s\omega_o^2}= \\ &= \frac{{K_C}^2-1-K_C+2e^{-2\xi\pi}+K_c e^{-2\xi\pi}-2K_c e^{-\xi\pi}}{(1+K_C)^2}\end{aligned} \tag{5.63}$$

$$\begin{aligned}\phi_{12} &= \frac{1+e^{-\xi\pi}}{LC_s\omega_0^2}\left(e^{-\xi\pi}-1+\frac{1+e^{-\xi\pi}}{LC_s\omega_0^2}\right)= \\ &= \frac{\Big(1+e^{-\xi\pi}\Big)+\Big((K_C+2)e^{-\xi\pi}-K_C\Big)}{(1+K_C)^2}\end{aligned} \tag{5.64}$$

$$\begin{aligned}\phi_{21} &= \Big(1+e^{-\xi\pi}\Big)\left(1-\frac{1+e^{-\xi\pi}}{LC_s\omega_o^2}-e^{-\xi\pi}\right)= \\ &= \frac{1+e^{-\xi\pi}}{1+K_C}\Big(K_C-(2+K_C)e^{-\xi\pi}\Big)\end{aligned} \tag{5.65}$$

$$\begin{aligned}\phi_{22} &= e^{-2\xi\pi}-\left(\frac{1-e^{-2\xi\pi}}{LC_s\omega_o^2}\right)= \\ &= \frac{(K_C+2)e^{-2\xi\pi}-1}{1+K_C}\end{aligned} \tag{5.66}$$

$$\Gamma_1 = \frac{\Big(1+e^{-\xi\pi}\Big)^2}{LC_s\omega_0^2}\left(1+\frac{1}{LC_s\omega_0^2}\right) \tag{5.67}$$

$$\Gamma_2 = \Big(1+e^{-\xi\pi}\Big)\left(1-\frac{1-e^{-\xi\pi}}{LC_s\omega_0^2}+e^{-\xi\pi}\right) \tag{5.68}$$

Then, the trajectory will be stable if the eigenvalues of the discrete-time system in (5.62) are located within the unit circle. The corresponding characteristic polynomial is given by $X(\lambda)=\lambda^2+b\lambda+c$, whose coefficients are:

$$b=-\phi_{11}-\phi_{22}=\frac{-{K_C}^2+2+2K_C+2K_C e^{-\xi\pi}-(K_C+2)^2e^{-2\xi\pi}}{(1+K_C)^2} \tag{5.69}$$

$$c = \phi_{11}\phi_{22} - \phi_{12}\phi_{21} = \frac{\left(1 - K_C e^{-\xi\pi}\right)^2}{\left(1 + K_C\right)^2} \tag{5.70}$$

Jury's criterion [93] is applied to the 2nd order algebraic equation $X(\lambda)$ in order to determine if the eigenvalues are located within the unit circle. This criterion establishes that the eigenvalues will be inside the unit circle if the following conditions are fulfilled:

1. $X(1) > 0 \Rightarrow 1 + b + c > 0 \Rightarrow 1 > e^{-2\xi\pi}$
2. $X(-1) > 0 \Rightarrow 1 - b + c > 0 \Rightarrow {K_C}^2(1 + e^{-2\xi\pi}) + 2(1 + K_C)e^{-2\xi\pi} > 2K_C e^{-\xi\pi}$
3. $|c| < 1 \Rightarrow \left|1 - K_C e^{-\xi\pi}\right| < 1 + K_C$

Condition 1

Condition 1 will be fulfilled if $1 + b + c > 0$ is accomplished. Introducing (5.69) and (5.70), the following expression holds

$$\begin{gathered}
1 + \frac{-{K_C}^2 + 2 + 2K_c + 2K_c e^{-\xi\pi} - (K_C + 2)^2 e^{-2\xi\pi}}{(1 + K_C)^2} + \frac{1 - 2K_c e^{-\xi\pi} + {K_C}^2 e^{-2\xi\pi}}{(1 + K_C)^2} > 0 \Rightarrow \\
\Rightarrow 1 + {K_C}^2 + 2K_c - K_C^2 + 3 + 2K_c > (4 + 4K_c)e^{-2\xi\pi} \Rightarrow \\
\Rightarrow \boxed{1 > e^{-2\xi\pi}}
\end{gathered} \tag{5.71}$$

It can be observed that this condition is always satisfied, since $2\xi\pi > 0$.

Condition 2

Condition 2 implies the accomplishment of the inequality $1 - b + c > 0$, which leads to

$$\begin{gathered}
1 + \frac{{K_C}^2 - 2 - 2K_c - 2K_c e^{-\xi\pi} + (K_C + 2)^2 e^{-2\xi\pi} + 1 - 2K_c e^{-\xi\pi} + K_C^2 e^{-2\xi\pi}}{(1 + K_C)^2} > 0 \Rightarrow \\
\Rightarrow \boxed{{K_C}^2(1 + e^{-2\xi\pi}) + 2(1 + K_C)e^{-2\xi\pi} > 2K_c e^{-\xi\pi}}
\end{gathered} \tag{5.72}$$

Making the change of variable $e^{-\xi\pi} = x$, the inequality (5.72) leads to $g(x) > 0$ where

$$\begin{aligned} g(x) =&{K_C}^2(1+x^2)+2(1+K_C)x^2-2K_Cx= \\ &=\left({K_C}^2+2(1+K_C)\right)x^2-2K_cx+{K_C}^2 \end{aligned} \tag{5.73}$$

Note that $g(x)$ has a minimum at $x=\frac{K_C}{{K_C}^2+2(1+K_C)}$ since

$$\frac{dg(x)}{dx}=2\left({K_C}^2+2(1+K_C)\right)x-2K_c=0 \tag{5.74}$$

$$\frac{d^2g(x)}{dx^2}=2\left({K_C}^2+2(1+K_C)\right)>0 \tag{5.75}$$

The value of the minimum is given by

$$g(x)_{min}=-\frac{{K_C}^2}{{K_C}^2+2(1+K_C)}+{K_C}^2>0\,, \tag{5.76}$$

since ${K_C}^2+2K_C+1>0$. Thus, condition 2 is also fulfilled regardless of the parameters of the circuit.

Condition 3

Condition 3 is fulfilled if $|c|<1$ is accomplished. From (5.70), condition 3 results in $\left|1-K_Ce^{-\xi\pi}\right|<1+K_C$, which is always satisfied.

Therefore, it can be concluded that the generation of the spiral in the LCC self-oscillating resonant converter is always stable.

Similarly, it can be demonstrated that imposing $V_{Cs}\left(k+1\right)=V_{Cs}\left(k\right)$ and $V_{Cp}\left(k+1\right)=V_{Cp}\left(k\right)$ in (5.62) yields to expressions (5.37) and (5.38), corroborating the validity of the model.

5.3 Application: LCC self-oscillating ballast for IEFL lamps

During the last decade, efficient lightning solutions have been intensively researched due to their impact on worldwide energy consumption and the need of reducing the overall energy waste in the world. In this section, a ballast for driving one of the new lightning solutions that appeared in the market, the Induction Electrodeless Fluorescent Lamp (IEFL), is designed.

The IEFL is based on a general fluorescent lamp with the peculiarity that the gas filled vacuum tube is energized by a magnetic field generated with an external inductor. It does not have electrodes directly connecting the gas of the lamp with the electric circuit. In the IEFL, the magnetic field generated in the external inductor produces a gas discharge inside the bulb, allowing its ignition and obtaining finally a light flux.

The elimination of the electrodes extends the lamp's life between 5-7 times in comparison with an standard fluorescent lamps. As stated in [94], "induction has ultra long life, most often twice as long as LED, 5-13 times longer than metal halide and high-pressure sodium lamps, and 5-7 times longer than standard fluorescent lamps". In addition, this technology reproduces the colors of natural sunlight closer than any other, facilitating the adaptation of the human eye to the artificial light.

Despite its recent introduction on the market, induction lightning concept is not new. First application was made by Nikola Tesla in 1891 [95], when he lit 200 lamps without wires. However, the lack of manufacturing techniques impeded its massive production until the last decade.

Due to the growing interest of the industry in this technology, major manufacturers such as Philips and Osram have presented their own solutions for obtaining affordable lamps compliant with all the safety regulations. Philips induction lamps operate at a frequency of 2.6 MHz and present rounded bulb shapes, similar to a standard bulb but with an inductor in the center of the lamp. Osram lights operate at a frequency of 250 kHz and present rectangular shapes. Benefits of Philips technique are a higher coupling coefficient and improved light extraction while Osram presents reduced EMI emissions and higher luminous efficacy [96].

The ballast implemented in this chapter employs the Osram development due to its benefits. Osram commercializes a range of IEFL lamps from 70 W to 150 W. The ballast is designed for the highest power level available, 150 W, in order to validate the effectiveness of self-oscillating technique in high-power applications.

Existent ballast designs in the literature [97–100] are typically based on LCC resonant converters due to their higher input impedance and higher voltage gain with respect to 2nd order converters. Therefore, a self-oscillating LCC resonant tank is selected for the ballast design.

5.3.1 Operation of the circuit

Generally a fluorescent lamp presents two different behaviors depending on its lightning state. The first one is characteristic of the startup, as the electrons inside the gas bulb need to be energized in order to produce light. That process, called ignition, presents high impedance values and requires high input voltages and powers. After startup, the lamp emits light, entering into the second state, known as steady-state. In that situation the impedance is stable and lower than before, and only the dynamics produced by the heating of the lamp will produce small variations of its value. Thus, the gain of the ballast has to vary accordingly to each state in order to operate the lamp correctly.

The circuit design is based on the switching control law $u = sg(i_L)$ for simplicity of the design and cost-efficiency. Therefore, the frequency depends only on the circuit parameters, in contrast with most of existing contributions based on frequency modulation [100]. Consequently, variations of the load will generate a modification of the gain in the approach here proposed.

As stated in Chapter 1, load variations will produce different results in 3rd order structures from those in 2nd order. While 2nd order structures increase or reduce their gain over a fixed resonant frequency, 3rd order structures also vary the resonant frequency between two boundaries. These boundaries are defined by the frequency at no-load conditions, which is obtained short-circuiting the output, and the frequency at infinite load, which is obtained in open-circuit conditions. In [21] both resonant frequencies are identified as f_0 and f_∞ respectively. The same notation has been adopted here:

$$f_0 = \frac{1}{2\pi\sqrt{LC_s}} \tag{5.77}$$

$$f_\infty = \frac{1}{2\pi\sqrt{L(C_s \| C_p)}} \tag{5.78}$$

An example of this behavior is illustrated in Figs. 5.10 and 5.11, where Bode plots of transfer functions $H(s)$ and $Zi(s)$ for different loads are depicted. The resonant tank parameters of the example are: $L = 33\,\mu$H, $C_s = 130$ nF and $C_p = 13$ nF. With that parameters, $f_0 = 76.8$ kHz and $f_\infty = 255$ kHz. In Fig. 5.11 the input impedance for zero and infinite loads, defined as $Z_{i0}(s)$ and $Z_{i\infty}(s)$, are depicted in discontinuous red and blue lines respectively. Both situations define the boundaries of the possible impedance variation. In addition, in Fig. 5.10 the behavior of the LCC is observed. It can be seen that if the switching frequency is near f_0 the circuit behaves like a SRC, while if the switching frequency is near f_∞ it behaves like a PRC.

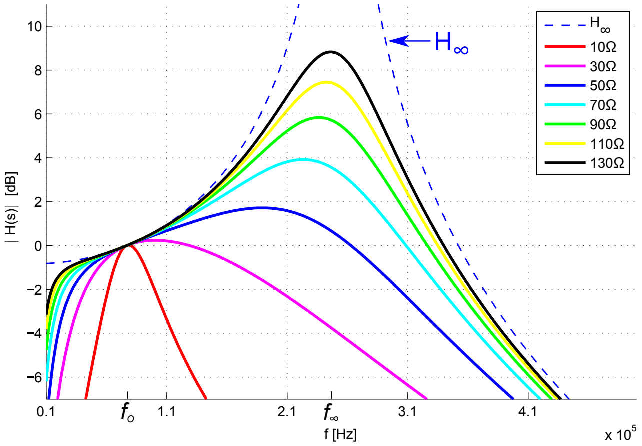

Figure 5.10: Bode plot of the transfer function $H(s)$ for different loads.

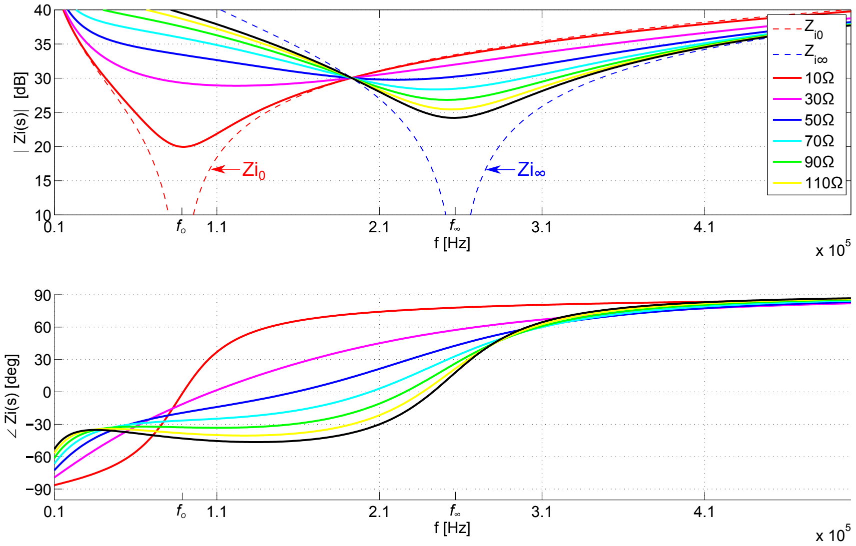

Figure 5.11: Bode plot of the transfer function $Z_i(s)$ for different loads.

Previous figures demonstrate that the desired behavior is accomplished in a LCC operating with $u = sg(i_L)$, as higher loads will produce higher gains and viceversa. Therefore, it is possible to implement a LCC self-oscillating ballast that offers the required ignition and steady-state gains depending on the impedance of the lamp in each situation, provided that some constraints are accomplished. These constraints come from the requirement of having high Q and K_C factors for the existence of self-oscillation. Moreover, the ignition gain depends entirely on the behavior of the lamp, as the resonant tank design is determined in steady-state conditions.

Thus, the design of the resonant tank for steady-state conditions has to be done first and then the value of the ignition gain has to be obtained and the accomplishment of the minimum and maximum ignition voltage restrictions has to be verified.

Therefore, the overall ballast design procedure follows these steps:

1. Establishment of the resonant tank parameters for steady-state design.
2. Analysis of the ignition gain with the previous resonant tank. If the gain is equal or higher than the minimum required for igniting the lamp, the design can continue. Otherwise, redesign the parameters.
3. Evaluation of the accomplishment of the minimum and maximum ignition voltage restrictions given by the lamp's manufacturer.
4. Introduction of a safety limiting circuit if required, in order to limit the parameters above the maximum ratings during ignition.

In the following sections the previous steps are applied and described in detail.

5.3.2 Converter design

Since the accomplishment of the design restrictions depends on the ignition and steady-state lamp impedances, the definition of these parameters for the lamp under study is required. The lamp selected for this work is the Osram Endura 150 W. Different approaches, based on the analysis of the existent models for this lamp in the literature [101,102] and the behavior of commercial ballast [103] have been analyzed in order to establish the lamp impedance.

In [101], a model of the lamp's input impedance as a function of the active power supplied is proposed. A comparison between this model and a simplified model, presented in [102], is shown in Fig. 5.12. The model of [101] is depicted in purple while the model of [102] is depicted in red. Both models show a similar response for powers over 75 W, resulting in an impedance of 200 Ω at steady-state. Besides, all of them indicate that impedance for low power is very high but they differ about the value at startup. Thus, the ignition impedance has to be established by analyzing the response of a ballast commercialized by the same

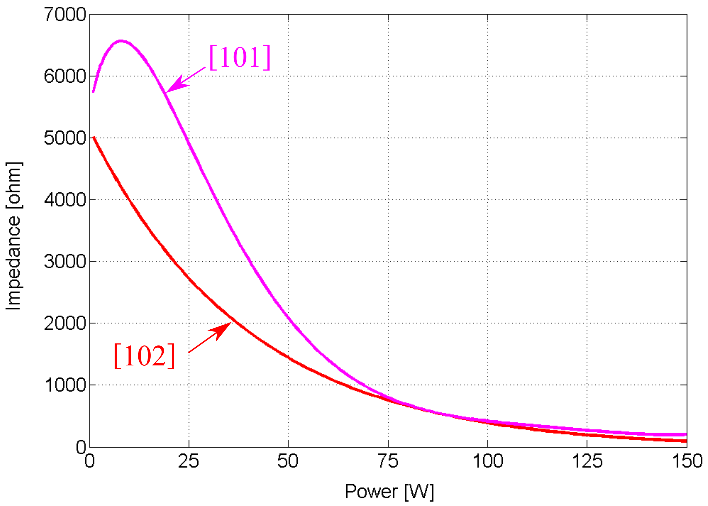

Figure 5.12: Osram Endura 150 W IEFL lamp model comparison. In purple, model presented in [101] and in red, model presented in [102].

company.

An Osram QUICKTRONIC Endura 150/240 S ballast has been tested together with an Osram Endura 150 W lamp. Fig. 5.13 depicts the response of this ballast at ignition, steady-state and slow warm-up (100 s). Fig. 5.13a presents an overview of the different states that presents the lamp when it is started. First, a slim peak is shown, corresponding with the ignition period. After that, the lamp starts lightning and the impedance falls to its steady-state value. Then, it can be seen that the output voltage and current increase slowly, following the warm-up of the lamp, which stabilize when the steady-state temperature is reached. Corresponding output voltage and current levels for ignition and steady-state are depicted in Figs. 5.13b and 5.13c. The ignition period is about 250 μs and the peak voltage reached is 1700 V. The lamp presents a highly inductive behavior under that situation, generating a variation of the peak current between 1.5 to 4.2 A peak. For that reason, the data points of the measurements in Fig. 5.13b are saved and the average impedance value during this period is analyzed. The envelope of the voltage and current is calculated with those data and depicted in Fig. 5.14a. For simplicity in the calculation, the previous results are divided into 8 different sections. The average value of each section is obtained and Ohm's law is applied over each average value in order to obtain the impedance of each section. The results obtained have been depicted in Fig. 5.14b. An average ignition impedance of 1500 Ω is obtained and it is considered during the design of the resonant tank. Significant difference between models and commercial ballast

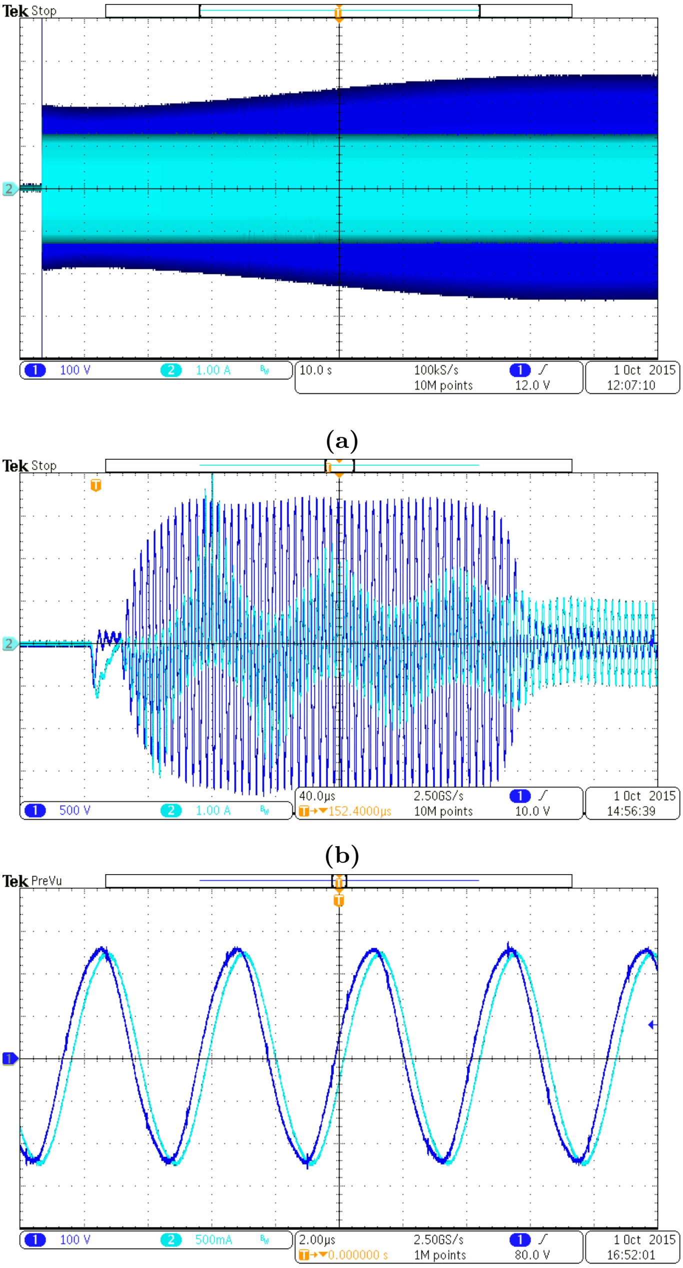

(a)

(b)

(c)

Figure 5.13: Response of a commercial ballast: (a) ignition detail, (b) steady-state detail, (c) ignition and slow warm-up. Light blue lines: output current, dark blue lines: output voltage.

response is observed. In this thesis, it has been considered that the experimental ballast response is more representative of the real conditions. Note, however, that the measured impedance of the commercial ballast in steady-state agrees with both models.

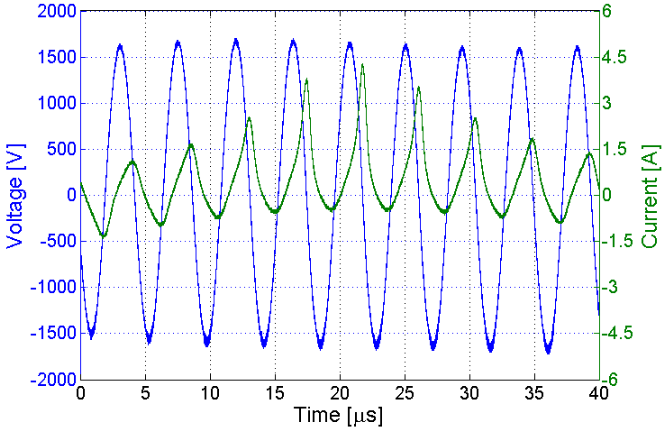

(a)

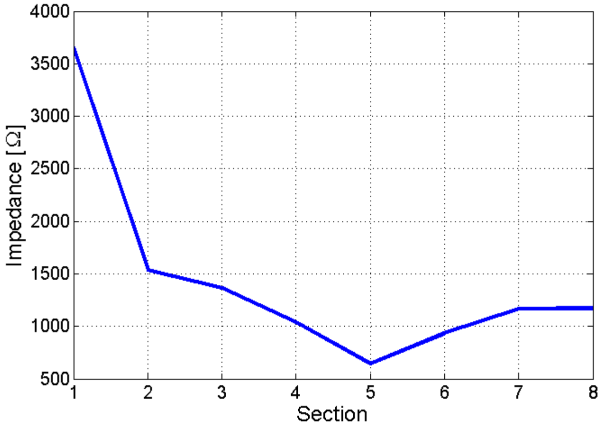

(b)

Figure 5.14: Analysis of the ignition impedance: (a) Data acquired from a commercial ballast, (b) Average impedance per section.

The minimum and maximum ignition voltage allowed by the lamp have to be defined in order to evaluate the correctness of the design. In [[101], Fig. 114] an experimental measurement of the ignition of the same lamp with a novel LCC ballast is illustrated. It can be seen that the ignition peak voltage is 1000 V, which has been considered the minimum ignition voltage. Since the manufacturer does not provide absolute maximum ratings, the voltage provided by the commercial ballast (1700 V) is considered the maximum voltage allowed by the lamp.

This application is designed for operating in a future building with a DC microgrid distribution. Nowadays, a general standard that defines the parameters of a DC network distribution in buildings does not exist. However, existent literature [104–107] describes a distribution network for homes based on a high voltage bus ($\sim$ 380 - 400 V) and a low voltage bus ($\sim$ 48 V). The latter is the recommended for lightning in the previous literature. Additionally, 48 V DC distribution is being employed in electric vehicles according to the LV 148 standard [108–110], implying that future vehicle-to-grid applications will require a 48 V DC bus in buildings. For that reason, an input voltage of 48 V is selected for this design. Moreover, a K_C of 10 is also applied.

Table 5.2 summarizes the parameters of design of the converter. The power stage is the LCC converter depicted in Fig. 5.8.

One of the advantages of the application of the self-oscillation with the previous constraints indicated in Section 5.1.2 is its straightforward design technique. The procedure for selecting the values of L, C_s and C_p is summarized next,

Self-oscillating LCC resonant tank design steps

1. Define input and output voltage in steady-state.
2. Define the desired switching frequency ω_0 and the load R.
3. Calculate Q ($Q|_{\omega_{sw}=\omega_0} = |H(j\omega_0)| = V_{out}/V_{in}$, if $\xi << 1$).
4. Evaluate if $Q \geq 3.15$ is accomplished. If not, the system will not be able to self-oscillate and new parameters have to be selected.
5. Calculate the value of the parallel capacitor with $C_p = \frac{Q}{\omega_0 R}$.
6. Select $K_C \geq 8$ ($K_C = C_s/C_p$). Take into account that K_C value will determine the amplitude of the voltage across the series capacitor C_s. Verify if the capacitor voltage ratio is higher than the amplitude imposed by K_C. Otherwise, reduce K_C if possible or discard the design.
7. Calculate the value of the series capacitor with $C_s = K_C C_p$.
8. Calculate the value of the inductance with $L = \frac{1+K_C}{\omega_0^2 K_C C_p}$.

The equations for C_s ($C_s = K_C C_p$) and C_p ($C_p = \frac{Q}{\omega_0 R}$) are derived from the restrictions imposed by equations (5.43) and (5.55) in Sections 5.1.3 and 5.1.4, while the equation for L ($L = \frac{1+K_C}{\omega_0^2 K_C C_p}$) is obtained from (5.52) and (5.53).

Table 5.2: Design parameters of a self-oscillating LCC ballast

Parameter	**Value**
V_g	48 V
$v_{Cp,peak}$, *ignition min*	1000 V
$v_{Cp,peak}$, *ignition max*	1700 V
$v_{Cp,peak}$, *steady − state*	250 V
Q, *ignition min*	20.8
Q, *ignition max*	35.4
Q, *steady − state*	4.1
Z_{lamp}, *ignition*	1500 Ω
Z_{lamp}, *steady − state*	200 Ω
f_{sw}, *lamp*	250 kHz
K_C	10

The set of parameters in Table 5.2 results in the resonant tank summarized in Table 5.3. Given that these values are not commercially available, a set of alternative values and the resulting values of Q, f_0 and $v_{C,peak}$ have been included in the table.

Table 5.3: Resonant tank design for steady-state conditions

Parameter	**Value obtained**	**Commercial value**
L	34.3 μH	33 μH
C_s	130 nF	130 nF
C_p	13 nF	13 nF
f_0	250 kHz	254.85 kHz
Q	4.1	4.16
$v_{Cp,peak}$	250 V	253.76 V

Then, the ignition gain obtained with that design has to be calculated in order to check if the resulting voltage is inside the ignition limit parameters. If equation (5.47) is applied, a peak output voltage of 1500 V is found at ignition. This voltage is higher than the minimum required for igniting the lamp (1000 V) and less than the offered by the commercial ballast (1700 V), which represents a safe operative value. Additionally, Fig. 5.15 shows the effect of load variation over the resonant tank designed. A peak gain value of 28 for a 1400 Ω load, and a peak gain value of 4.2 for a 200 Ω load are observed, validating the previous theoretical calculation. Thus, the design of the resonant tank is valid and the converter can operate as desired.

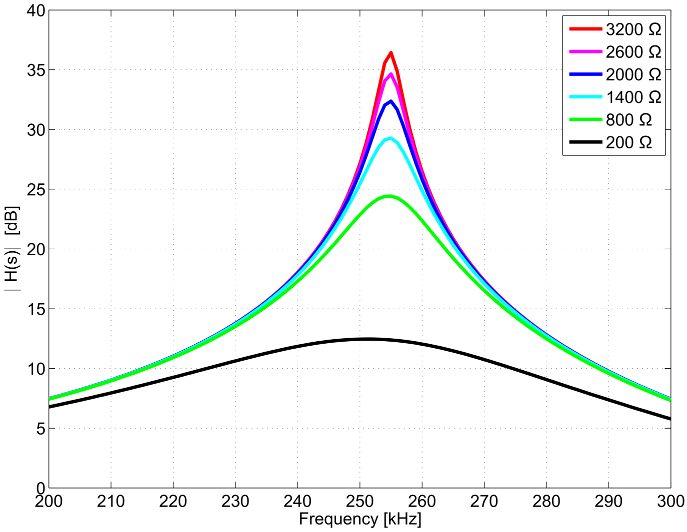

Figure 5.15: Gain variation as a function of the load for the LCC design selected: L=33 μH, C_s=130 nF and C_p=13 nF.

5.3.3 Simulation results

In order to verify the effect of the proposed converter, a simulation of a LCC converter with the proposed resonant tank and the lamp model from [101] has been carried out. Fig. 5.16 shows the output voltage and current during ignition and steady-state. An ignition output peak voltage of 1500 V and an steady-state peak voltage of 248 V have been obtained, in agreement with the expected values in Table 5.3. A steady-state output power of 148 W average has been obtained at a self-oscillating switching frequency of 247 kHz, confirming that the desired power level and frequency of operation of the lamp are achieved, and verifying the theoretical predictions.

5.3.4 Experimental prototype and results

An experimental prototype has been implemented with the parameters previously selected in order to verify the effectiveness of the proposed approach. Although the prototype presents the same structure than the circuit in Fig. 5.8, the selection of different components has been required in order to adapt its operation to the switching frequency and power levels of the ballast. A detailed description of the modifications in each stage is covered below. The control law, as indicated in the previous section, is $u = sg(i_L)$.

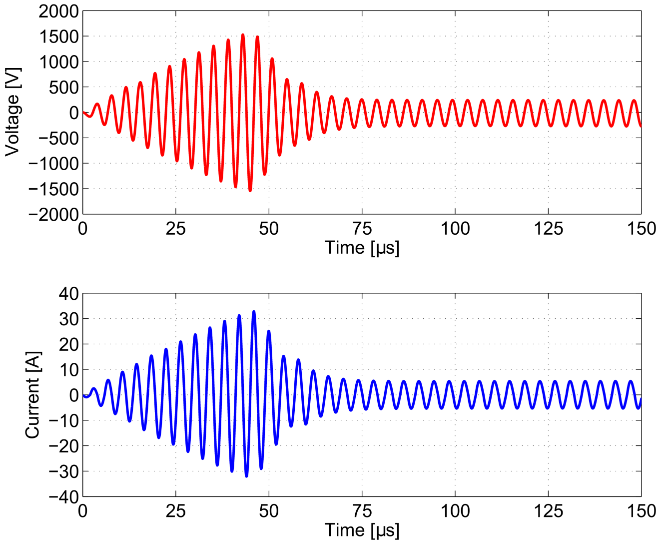

Figure 5.16: Simulation waveforms of the output voltage and current at ignition and steady-state with the selected resonant tank design: L=33 μH, C_s=130 nF and C_p=13 nF.

5.3.4.1 Components selection and stage design

In the circuit schema of Fig. 5.8 four main stages can be identified, which are:

- Full bridge inverter
- Current sensor
- Controller circuit: Comparator, dead time and driver
- Resonant tank

Full bridge inverter

No changes have been required in the MOSFET selection, given that the Infineon device IPB200N15N3 [111] presents a voltage and current maximum ratings of 150 V and 50 A respectively, higher than the 48 V and 30 A required.

Current sensor

The current sensor stage is composed of a transformer and a resistor that transduces current measurement into voltage. Although its structure is the same as in Section 5.1.6, new components have been selected. These new components present better parameters in order to adapt this stage to the higher current amplitudes of this prototype. It is worth to remark that current at ignition can reach peaks of 30 A.

Therefore, a new 1:20 transformer and a resistor of 15 Ω are introduced, resulting in a ratio of 20 A equal to 15 V. The transformer is composed by a toroidal ferrite core and is developed in-house for this application. Equivalently, a SMD resistor is introduced in order to avoid inductive parasitic effects of larger packages and 15.6 V zener diodes are introduced for limiting higher voltages produced by higher sensed currents.

Controller circuit

No remarkable modifications are introduced in that stage. The same comparator (LT1116) is selected as it presents reduced propagation delays and it is able to sense a ± 15 V input and generate a 0-5 V square signal with a complementary output. Moreover, the same driver (Texas Instruments UCC27211 [112]) is also applied as it presents a high performance in comparison with other similar components.

Resonant tank components

A commercial inductor specifically designed for high AC currents is selected in this application: the Coilcraft AGP4233-333 [113]. Its ferrite core and flat solid wire section allows to reduce parasitic effects and decreases drastically the losses at the current level required in steady-state (10 A peak to peak). Additionally, 1600 V C0G capacitors are selected for the resonant tank due to the high input voltage existent at ignition.

Summary of components

Table 5.4 summarizes the components of the experimental prototype.

5.3.4.2 Results

Fig. 5.17 illustrates the ignition and steady-state operation of the previous circuit. It is observed a total ignition time of 3.75 ms, a voltage peak of 1050 V and a power of 150 W average during this period. In comparison with the results obtained with the commercial ballast, this circuit increases the startup time by 3,5 ms, reducing the ignition voltage by 650 V. Zoom over ignition period, shown in Fig. 5.18, validates that no inrush current or voltage is present.

Moreover, a stable switching frequency of 215 kHz and an inductor peak current

Table 5.4: Experimental VSS self-oscillating LCC ballast parameters set

Parameter	**Component**	**Value**
V_g	-	48 V
C_{in}	X7R	11 μF
Q_{1-4}	IPB200N15NS3	-
L	Coilcraft AGP4233-333	33 μH
C_s	C0G/NP0	130 nF
C_p	C0G/NP0	13 nF
Current sensor	Transformer	1:20
R_{sens}	SMD Resistor	15 Ω
Comparator	LT1116	-
Driver	UCC27211	-

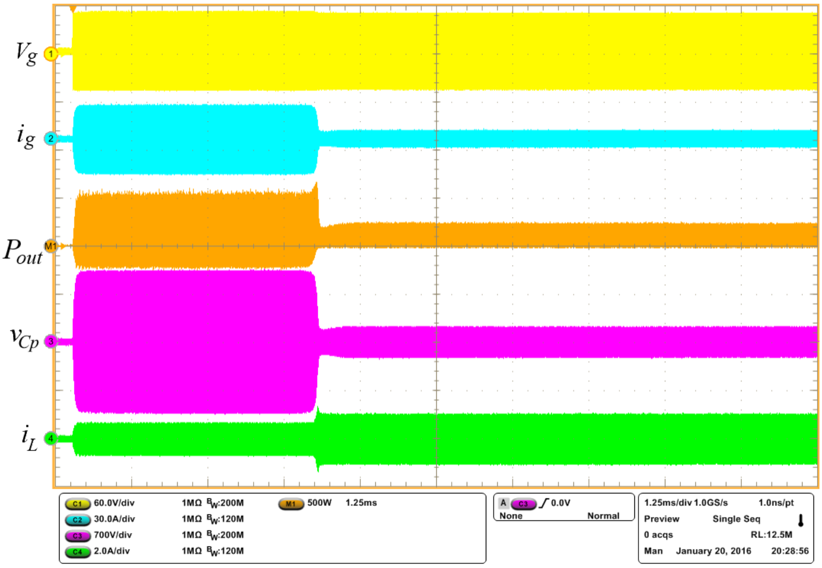

Figure 5.17: Ignition and steady-state experimental results of the LCC lamp ballast.

of 19 A is obtained during the ignition period, as seen in Fig. 5.19a. Output current shows a peak value of 700 mA, presenting a reduction of 85% ($\Delta i_{out} = -3.8$ A) with respect to the commercial ballast. The voltage and current reduction of this approach with respect to the commercial ballast is accomplished due to a reduced phase-shift between output voltage and current during ignition. Besides, as it can be seen in Figs. 5.19b and 5.20 constant sinusoidal signals and a smooth transition between ignition and steady-state are obtained, in contrast with the variable signals obtained in the commercial ballast.

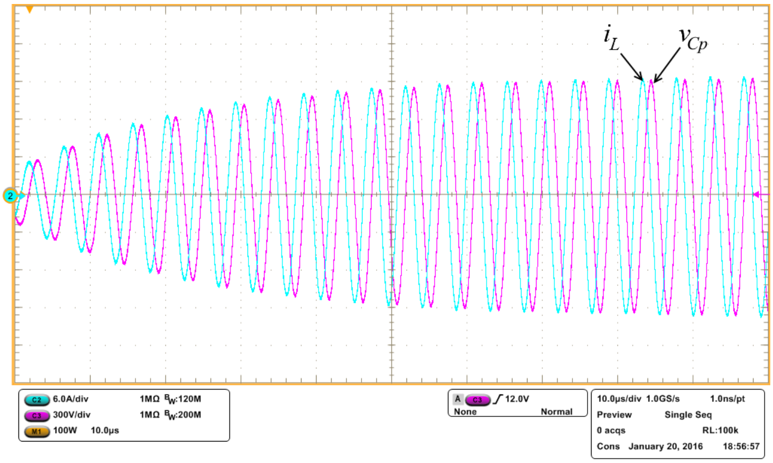

Figure 5.18: Output voltage and input current in the startup from CI = 0.

A zoom of the steady-state signals, shown in Figs. 5.19c and 5.21, depicts an output peak voltage of 277 V and peak current of 1 A whereas inductor peak current is 5.5 A. Switching frequency at steady-state is 215 kHz and power delivered to the lamp is 130 W average, obtaining an efficiency of 85%. Table 5.5 summarizes the expected values and the experimental results obtained at steady-state, showing a good agreement.

Table 5.5: Comparison between expected values and experimental results obtained at steady-state

Parameter	Theoretical value	Experimental value
f_0	255 kHz	215 kHz
$v_{Cp,peak}$	254 V	277 V
$i_{L,peak}$	5.8 A	5.5 A
$i_{out,peak}$	1.27 A	1 A
$P_{out,average}$	150 W	130 W
Q	4.16	4.53

Additionally, the effectiveness of the circuit under the variations produced by the low-frequency dynamics of the impedance in steady-state is verified. As it can be seen in Fig. 5.22, the circuit is able to follow the impedance variation within safe and desired power and voltage levels. The maximum output power is obtained in steady-state, ensuring the safeness of the proposed ballast in ignition and steady-state conditions.

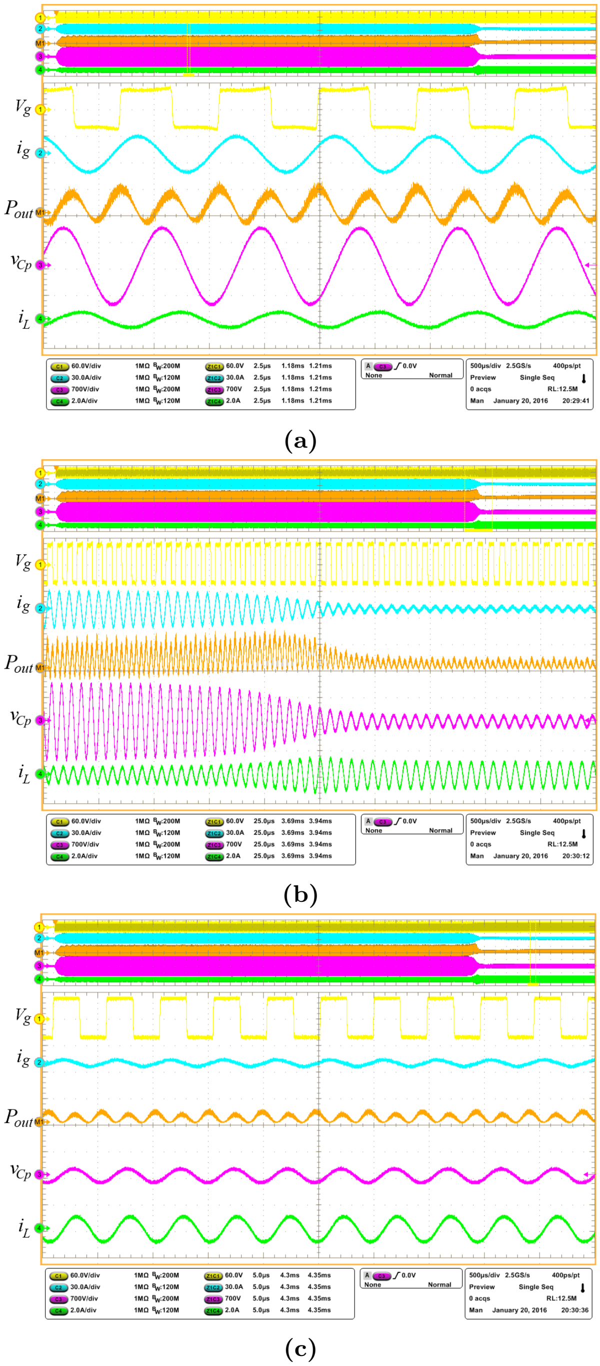

Figure 5.19: Detail of: (a) Ignition, (b) Transition between ignition and steady-state, (c) Steady-state.

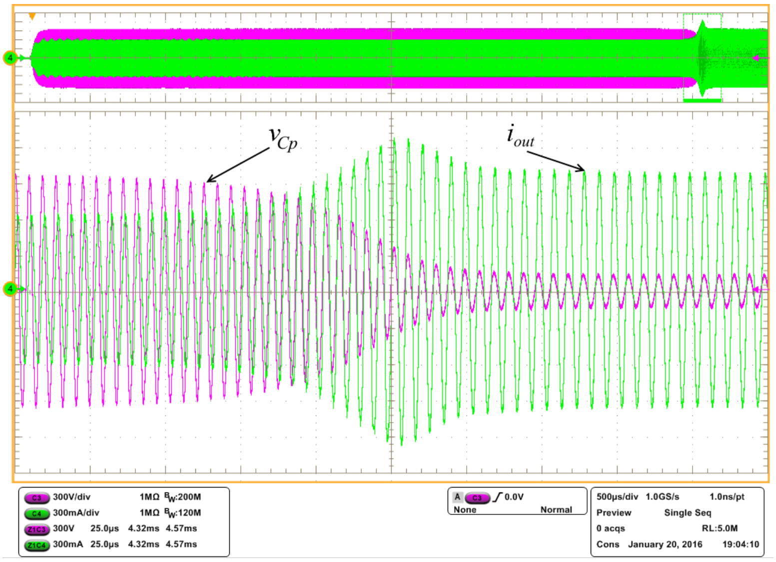

Figure 5.20: Output voltage and output current during transition between ignition and steady-state.

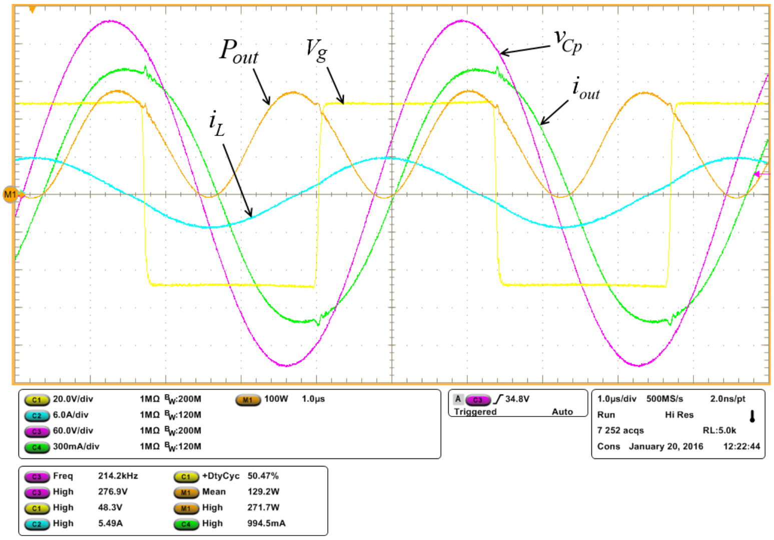

Figure 5.21: Experimental input and output steady-state values.

Therefore, the effectiveness of the self-oscillating LCC converter as a IEFL ballast is verified. Benefits obtained with this approach are increased safety and robustness, cost-efficiency and longer operative life due to the reduction of the stress over the components. The major drawback is an increased ignition period in

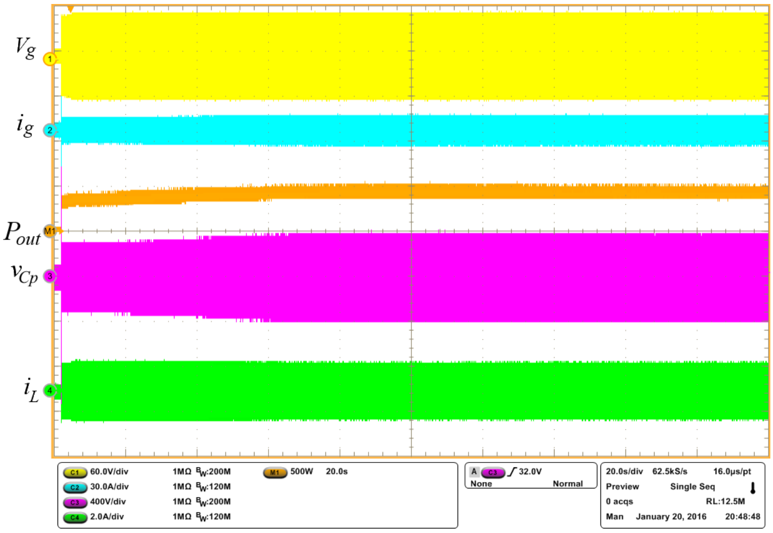

Figure 5.22: Experimental input and output steady-state waveforms.

comparison with the commercial ballast, although the difference is not noticeable for the human eye.

Fig. 5.23 shows a picture of the prototype with its main parts identified. Its size is 137 x 63 x 80 mm (width, depth and height respectively) and weights 200 grams. Fig. 5.24 presents a picture of the lamp under operation, while Fig. 5.25 illustrates the experimental setup, which consist of three different power sources, the prototype and an external relay in conjunction with a signal generator for its activation. Power sources A and B are used as power supplies for the driving and the auxiliary circuitry respectively, whereas power source D is the main DC input source. Relay G of Fig. 5.23 and the signal generator E of Fig. 5.25 are introduced only for safety reasons during the test. They are used as a ON-OFF switch, emulating a domestic power switch. Fig. 5.26 illustrates the overall setup with the lamp in the background.

5.3.5 Gain limiters

Although this application does not require any specific gain limitation at ignition, it is desirable to introduce it for safety reasons. Unexpected variations of the input voltage or the impedance can modify the gain in a way that unsafe output values are produced. Besides, in order to extend the feasibility of this ballast concept to other lamps with higher impedances, such as the High Pressure Sodium (HPS) lamps, it is worth to discuss different possible solutions to limit the gain.

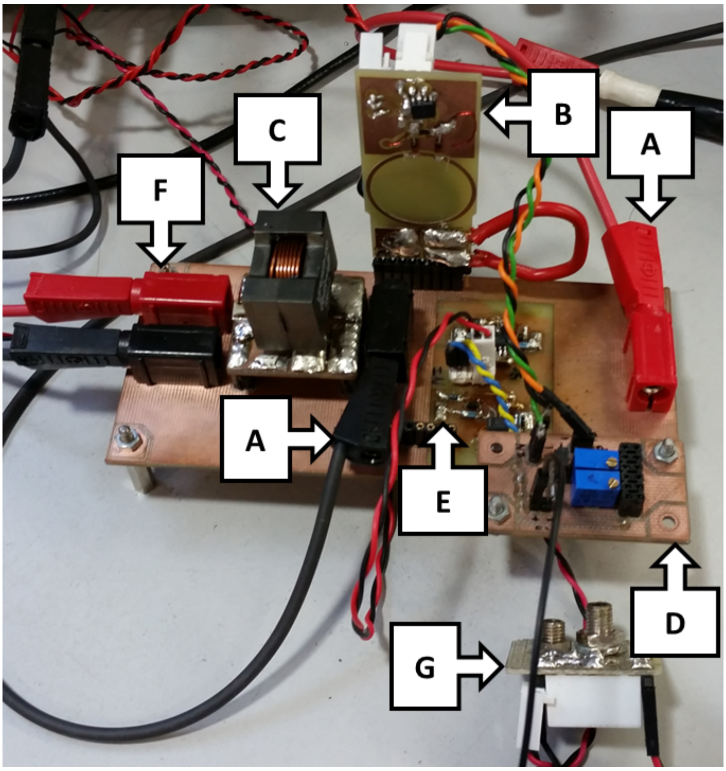

Figure 5.23: Picture of the experimental prototype board. Parts:(a) DC input, (b) Current sensor, (c) Resonant tank (LCC), (d) Dead-time circuit, (e) Driver circuit, (f) AC output, (g) activation relay.

Figure 5.24: Lamp used in the experiment (Model: Osram Endura 150 W).

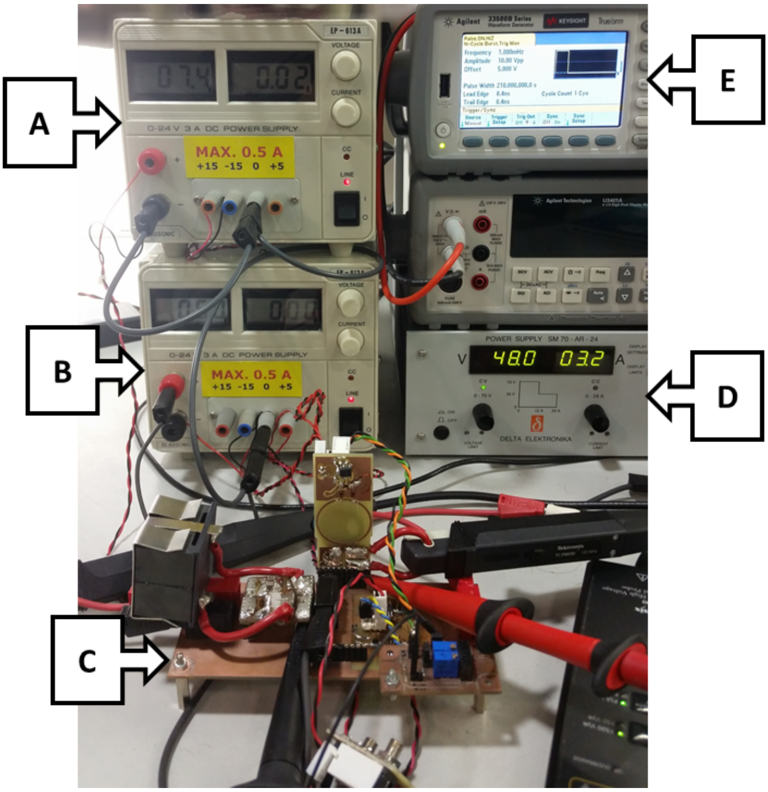

Figure 5.25: Experimental set-up: (a) Drivers supply, (b) Dead time and auxiliary circuitry supply, (c) Self-oscillating LCC prototype under test, (d) Input power supply, (e) Signal generator for relay activation and deactivation.

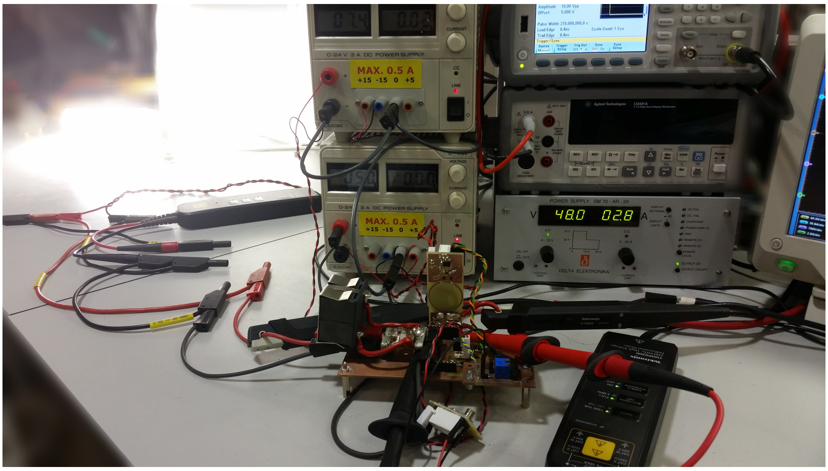

Figure 5.26: Complete experimental set-up with lamp lightning.

Two different gain limiting circuits are proposed and discussed in detail:

- An impedance matching network inserted in parallel with the load.
- A hysteresis gain limiter inserted at the switching stage.

5.3.5.1 Impedance matching network

Its operation principle consists in connecting a variable resistance in parallel with the load device when an unsafe value is detected. When activated, the load impedance is reduced, such that the output voltage also decreases. Fig. 5.27 depicts the circuit diagram of this solution.

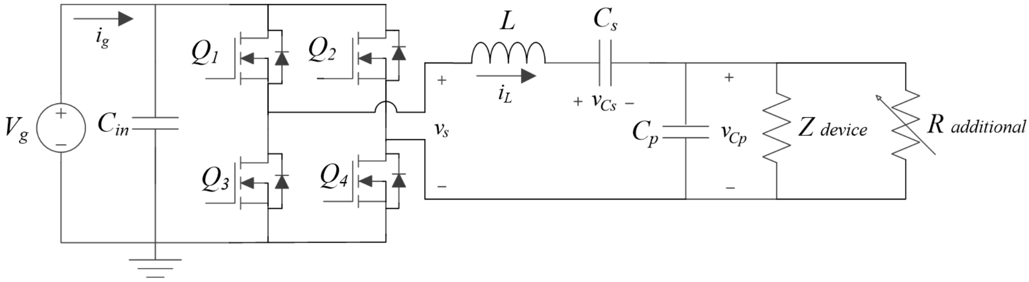

Figure 5.27: Circuit diagram of impedance matching network.

The main advantages of this approach are a straightforward implementation and a reduced cost. Nonetheless, it presents major drawbacks such as reduced efficiency and impossibility to adapt its value to load variations.

This approach can be appropriate, however, if a cheap and simple solution is desired in circuits with known constant impedances. In such case, it is possible to calculate the value of the additional resistance. Fig. 5.28 illustrates a circuit diagram applying this limiter to the circuit proposed in Section 5.3.2.

5.3.5.2 Hysteresis gain limiter

It is also possible to limit the gain by modifying the input voltage accordingly. As simplicity is desired in this application, a solution based on disconnecting the input voltage when an unsafe output value is reached is proposed. When the input is disconnected, voltage at the output of the resonant tank starts decreasing following the self-oscillating pattern until it arrives to zero. If the input is connected again before reaching zero, the amplitude increases until the limit

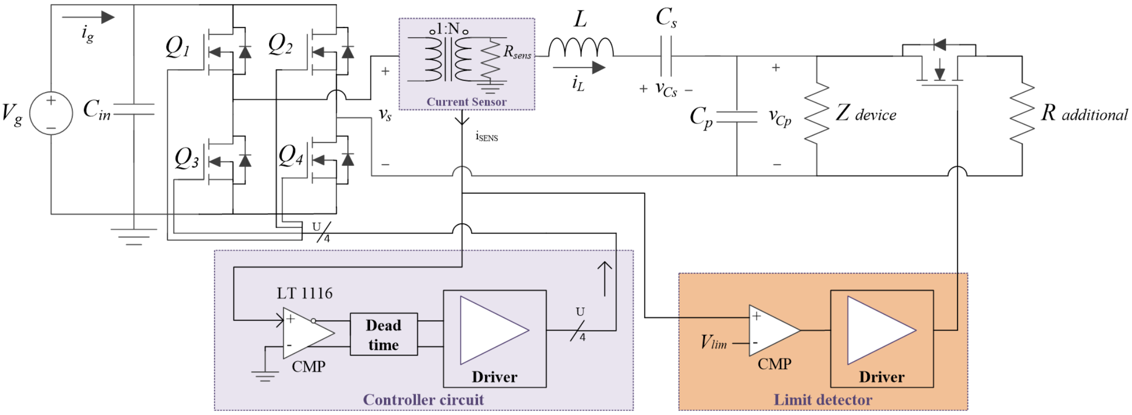

Figure 5.28: Scheme of a simple impedance matching network.

cycle is attained again. Therefore, it is possible to keep the output voltage limited to desired values by connecting and disconnecting the input as a function of the output value and a hysteresis.

As the resonant tank input cannot remain open, the connection of the low-side MOSFETs and disconnection of the high-side MOSFETs is required when limitation is activated in order to close the resonant circuit and disconnect the input correctly. When a safe value is recovered, the circuit continues to operate. In the case that the switching control law is of the form $u = sg(i_L)$, this behavior can be accomplished with a combination of different simple logic elements introduced in the control circuitry. Fig. 5.29 shows the circuit diagram of the limiter, while Fig. 5.30 depicts the scheme of the overall circuit if the limiter is connected to the ballast designed in the previous section.

Operation of this limiter is detailed in the chronogram depicted in Fig. 5.31.

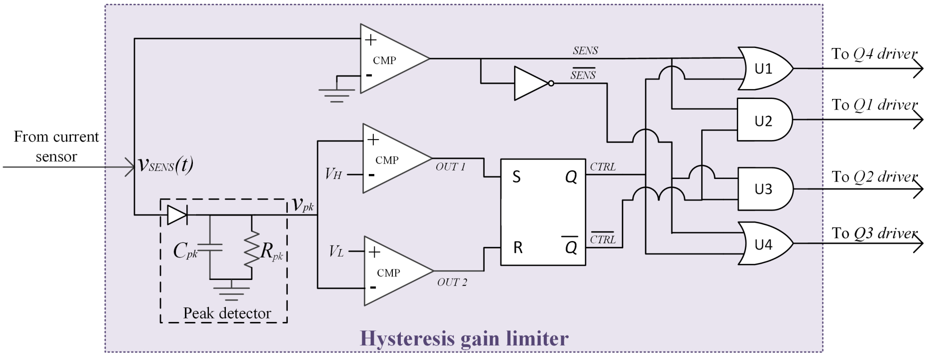

Figure 5.29: Circuit diagram of the proposed hysteresis gain limiter.

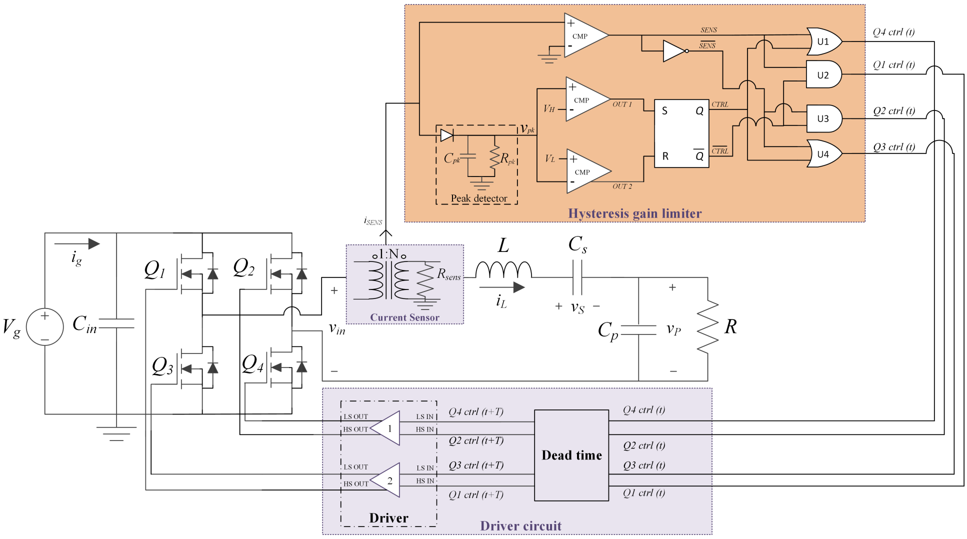

Figure 5.30: Scheme of the complete circuit including the proposed hysteresis gain limiter.

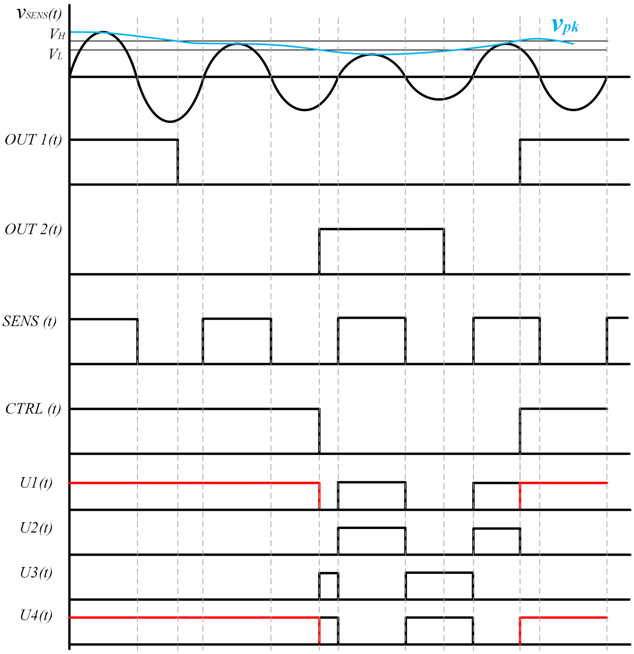

Figure 5.31: Control chronogram of the proposed hysteresis gain limiter. In red: signals generated by the activation of the limiter.

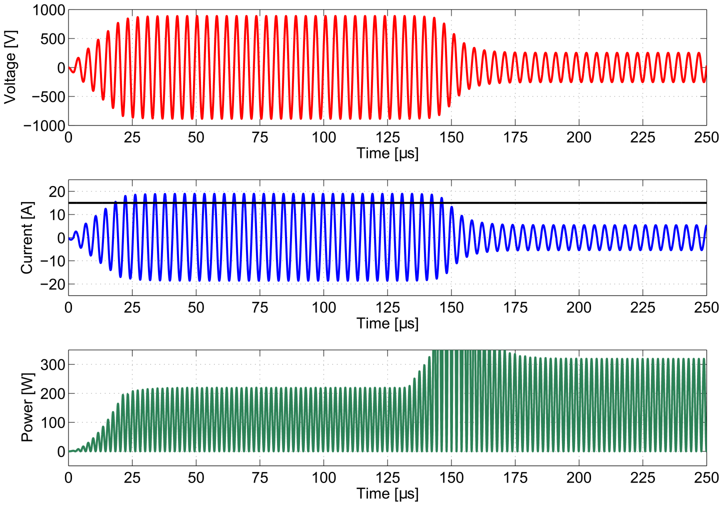

Figure 5.32: Simulated response at ignition and steady-state of the complete circuit including the proposed hysteresis gain limiter. Black line: current limit applied.

When sensed current (v_{SENS}) reaches the positive hysteresis value, the limiter is activated and Q_3-Q_4 are connected while Q_1-Q_2 are disconnected. This situation remains until sensed current reaches the negative hysteresis value, when normal operation of the circuit is resumed. Then, if a current value higher than the positive hysteresis is experimented again, the same operation will restart. Therefore, the amplitude can be limited by adjusting V_H and V_L and the resulting current ripple can be adjusted by increasing or reducing the hysteresis. The efficiency does not change with this implementation because only the switching pattern is modified.

A simulation of the circuit in Fig. 5.30 with the parameters of Table 5.3 is made in order to verify the effectiveness of this approach. Results obtained are depicted in Fig. 5.32. A current limit of 15 A is introduced and displayed in the figure with a black line. A hysteresis of ±1 A is also applied, resulting in a boundary of 16 A. It can be observed that the effectiveness of the circuit as gain limiter is verified, since the maximum output current reached is 16 A in contrast with 20 A reached when no limiter is employed.

Finally, the proposed limiter circuit is implemented experimentally with an ADCMP601 hysteresis comparator, two NC7S04 inverters, two NC7SZ32 OR gates and two NC7S08 AND gates, adding a total delay of 18 ns. Experimental results in Fig. 5.33 ratifies the expected responses and corroborates the effectiveness of the circuit.

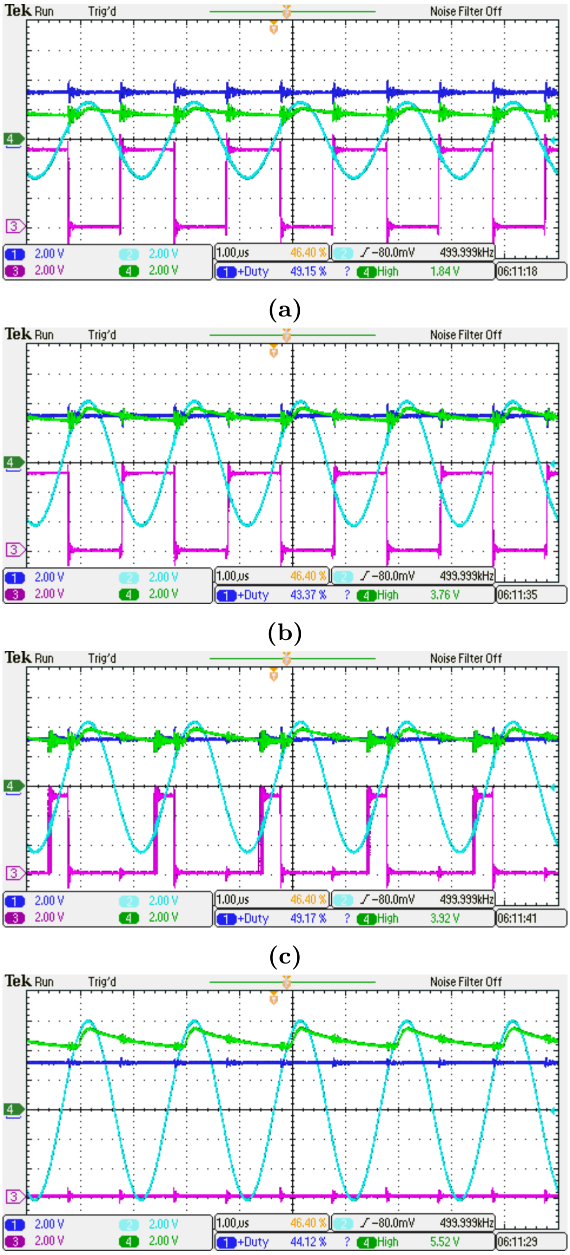

(a)

(b)

(c)

(d)

Figure 5.33: Limiter operation at: (a) Current below limit, (b) Current near limit, (c) Current crossing the limit, (d) Current higher than the limit. Dark blue: limit value, Green: peak current sensed ($v_{SENS,\,pk}$), Light blue: current through the inductor (i_L), Magenta: activation signal of $Q_1 - Q_2$ (corresponding to $U2(t)$ and $U3(t)$).

5.4 Extension of the analysis to other structures

The general analytical procedure described in Section 5.1 can be extended to the LLC resonant converter, depicted in Fig. 1.3d. Since the transient analysis is similar to that of LCC, under equal assumptions on the poles, the only aspect that has to be explored is finding the conditions that ensure a resistive behavior of the input impedance.

5.4.1 Determination of amplitude and period in the limit cycle

Following the previous analysis, the relationship between Q value and the parameters of the circuit has to be defined in order to design an underdamped system. Then, a relationship between α and $\xi\omega_0$ has to be obtained by analyzing the coefficients of the denominator of the input-output transfer function $H(s)$. Input impedance $Z_i(s)$ of the LLC is defined in Table 1.2 as

$$Z_i(s) = \frac{\frac{C_s L_p L_s}{R} s^3 + C_s(L_p + L_s)s^2 + \frac{L_p}{R} s + 1}{C_s s \left(1 + \frac{L_p}{R} s\right)} \tag{5.79}$$

Substituting $s = j\omega_0$ in (5.79) and imposing that $\omega_0^2 = \frac{1}{C_s L_s}$ yield

$$Z_i(j\omega_0) = \frac{-\frac{L_p}{L_s}}{C_s j\omega_0 \left(1 + \frac{L_p}{R} j\omega_0\right)} \tag{5.80}$$

One of the general self-oscillation features presented in Chapter 2 establishes that the input impedance presents a phase of 0° at the limit cycle. Thus, elimination of the imaginary part of the previous equation is required in order to fulfill this condition. As the imaginary part depends on the parameters L_p, R and ω_0, the following constraint is established, which concerns the value of Q for the LLC:

$$Q = \frac{L_p \omega_0}{R} >> 1 \tag{5.81}$$

If the previous hypothesis applies in (5.80), then $Z_i(j\omega_0) = R$, validating the correctness of the previous $\omega_0^2 = \frac{1}{C_s L_s}$ hypothesis.

The denominator of $H(s)$ in the LLC is identified in Table 1.1 as:

$$Den\, H(s) = s^3 + \frac{R(L_s + L_p)}{L_p L_s} s^2 + \frac{1}{L_s C_s} s + \frac{R}{L_p L_s C_s} = (s + \alpha)(s^2 + 2\xi\omega_0 s + \omega_0^2) \tag{5.82}$$

Similarly as in the LCC, if it is considered that the system presents a real pole and two complex conjugate poles (hypothesis 1), the following relationship can be defined:

$$s^3 + \frac{R(L_s+L_p)}{L_pL_s}s^2 + \frac{1}{L_sC_s}s + \frac{R}{L_pL_sC_s} = (s+\alpha)(s^2+2\xi\omega_0 s+\omega_0^2) \tag{5.83}$$

Identifying the coefficients of the third order polynomial results in:

$$\frac{R(L_s+L_p)}{L_pL_s} = 2\xi\omega_0 + \alpha \tag{5.84}$$

$$\frac{1}{L_sC_s} = \omega_0^2 + 2\xi\omega_0\alpha \tag{5.85}$$

$$\frac{R}{L_pL_sC_s} = \alpha\omega_0^2 \tag{5.86}$$

Supposing that $\omega_0 >> 2\xi\alpha$ due to the low damping ratio requirement, (5.85) can be rewritten as

$$\frac{1}{L_sC_s} = \omega_0\left(\omega_0 + 2\xi\alpha\right) \simeq \omega_0^2 \tag{5.87}$$

Introducing (5.87) in (5.86) results in

$$\alpha = \frac{R}{L_pL_sC_s}\frac{1}{\omega_0^2} = \frac{R}{L_p} \tag{5.88}$$

Finally, substituting the previous equations in (5.84) leads to

$$2\xi\omega_0 = \frac{R(L_s+L_p)}{L_pL_s} - \alpha = \frac{R(L_s+L_p)}{L_pL_s} - \frac{R}{L_p} = \frac{R}{L_s} \tag{5.89}$$

Therefore, the relationship between α and $\xi\omega_0$ is established by

$$\frac{\xi\omega_0}{\alpha} = \frac{\frac{R}{2L_s}}{\frac{R}{L_p}} = \frac{L_p}{2L_s} = \frac{K_l}{2} \tag{5.90}$$

with $K_l = L_p/L_s$.

As a result, if L_p is higher than L_s, the pole-separation hypothesis (hypothesis 2) will be accomplished and the system will self-oscillate.

Moreover, it is also required to identify the value of the state-variables in steady-state, in order to define simple design steps for synthesizing a self-oscillating LLC converter. Evaluating the input-output transfer function $H(s)$ at $s = j\omega_0$ and introducing ${\omega_0}^2 = 1/(L_sC_s)$, or equivalently, $\omega_0^2 L_s C_s = 1$, it is obtained that

$$\begin{aligned} H(j\omega_0)_{LLC} &= \frac{-L_pRC_s\omega_0^2}{-jL_p\omega_0 + RC_s(L_s+L_p)\omega_0^2 + jL_p\omega_0 + R} = \\ &= \frac{-L_pC_s\omega_0^2}{1 - C_s(L_s+L_p)\omega_0^2} = \\ &= \frac{-L_pC_s\omega_0^2}{-L_pC_s\omega_0^2} = 1 \end{aligned} \tag{5.91}$$

Therefore, this converter presents a similar behavior than the SRC. Consequently, the output voltage is

$$v_C(t) = V_m \cos(\omega_0 t) \tag{5.92}$$

and the current through the series inductor is

$$i_{Ls}(t) = \frac{V_m}{R}\cos(\omega_0 t) \tag{5.93}$$

with $V_m = \frac{4V_g}{\pi}$.

Moreover, if the system is described in phasor representation, it can be seen that $\overline{V_{Cs}}(j\omega_0) = \overline{I_{Ls}}(j\omega_0)\frac{1}{C_sj\omega_0}$, leading to the following time domain equation:

$$v_{Cs}(t) = \frac{V_m}{C_sR\omega_0}\cos\left(\omega_0 t - 90°\right) = \frac{V_m}{C_sR\omega_0}\sin\left(\omega_0 t\right) \tag{5.94}$$

Applying the same procedure over i_{Lp} taking into account that its phasorial transformation is $\overline{I_{Lp}}(j\omega_0) = \frac{\overline{V_c}(j\omega_0)}{jL_p\omega_0}$, it is obtained that

$$i_{Lp}(t) = \frac{V_m}{RQ}\sin\left(\omega_0 t\right) \tag{5.95}$$

5.4.1.1 Design procedure

The previous constraints lead to the design criteria required for enabling self-oscillation in a LLC converter. The design procedure is summarized next.

Self-oscillating LLC resonant tank design steps

1. Define the input voltage V_g in steady-state.
2. Define the desired switching frequency ω_0 and the load R.
3. Select a Q value taking into account that Q value is directly related with the current i_{Lp}. The higher the Q, the lower the value of i_{Lp}.
4. Verify that the requirement of high Q factor is accomplished ($Q \geq 3.15$).
5. Evaluate if the resulting i_{Lp} presents a value inside the design specifications. Otherwise, select a new Q if possible and recompute the design.
6. Calculate the value of the parallel inductor L_p with $L_p = \frac{QR}{\omega_0}$.
7. Define a K_l value taking into account that $K_l \geq 8$.
8. Calculate the value of the series inductor L_s with $L_s = \frac{L_p}{K_l}$.
9. Evaluate the losses of the resulting value of L_s. If the result is out of design specifications, recalculate with a lower K_l value.
10. Calculate the value of the series capacitor C_s with $C_s = \frac{1}{\omega_0^2 L_s}$.
11. Evaluate the value of v_{Cs} with the resulting C_s. Verify if it is inside design specifications. Otherwise, select a different K_l value and recalculate from step 6.

A design example following these steps is proposed. A switching frequency f_0 of 500 kHz is desired for a load $R = 10\,\Omega$ and an input voltage $V_g = 12$ V. As a low current i_{Lp} is desired, a Q value of 100 is selected. Moreover, a K_l of 10 is selected in order to keep the inductor values in similar range and C_s sufficiently large for obtaining a low v_{Cs} value. With these parameters, $L_p = 318\,\mu$H, $L_s = 31.8\,\mu$H and $C_s = 3.18$ nF. If equations (5.92), (5.93), (5.94) and (5.95) are evaluated with the previous resonant tank design, the results in Table 5.6 are found.

Table 5.6: Predicted amplitudes of the state-variables of the LLC circuit designed

Parameter	Value
$v_{C,\,peak}$	15.3 V
$i_{Ls,\,peak}$	1.53 A
$i_{Lp,\,peak}$	15.3 mA
$v_{Cs,\,peak}$	153 V

A simulation with the same parameters is made in order to verify the previous hypotheses and calculations. Fig. 5.34 illustrates the obtained results. It can be seen that the predicted values are in agreement with the simulated results, validating the previous restrictions and design procedure. Thus, general applicability of the analysis described in Section 5.1 for 3rd order resonant converters is validated.

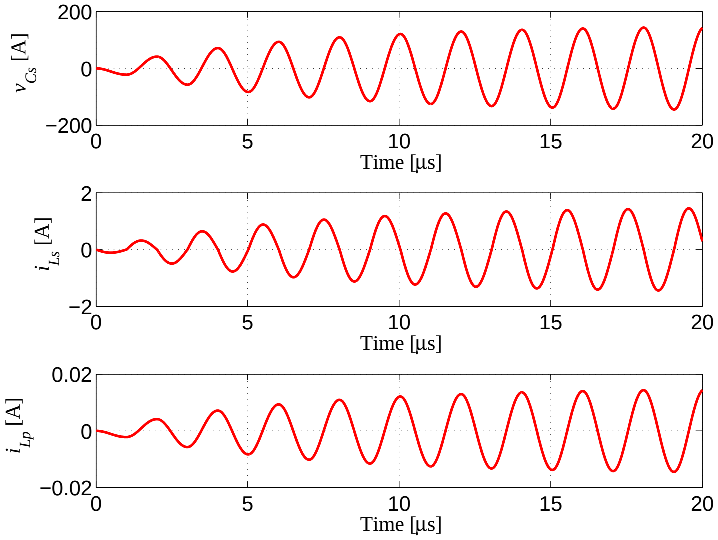

Figure 5.34: Time domain waveforms of the LLC with $f_0 = 500$ kHz, $R = 10\,\Omega$, $K_l = 10$, $L_s = 31.83\,\mu$H, $L_p = 318.3\,\mu$H, $C_s = 3.18$ nF.

Moreover, it can be seen that the behavior of the LLC under those conditions is similar to the SRC with the particularity of having in phase the current through the inductor L_p and the voltage through the capacitor C_s. This characteristic allows to represent the resulting three-dimensional limit cycle in a bi-dimensional plane just by adding the state-variables that are in phase. Fig. 5.35 depicts the generation of the limit cycle in the previous simulation applying that method. The axes are defined by:

$$x_1(t) = v_{Cs}(t) + i_{Lp}(t)(\times 1\Omega) = \frac{4V_g}{\pi R}\left(\frac{1}{C_s\omega_0} + \frac{1}{Q}\right)\sin(\omega_0 t) \tag{5.96}$$

$$x_2(t) = i_{Ls}(t) = \frac{4V_g}{\pi R}\cos(\omega_0 t) \tag{5.97}$$

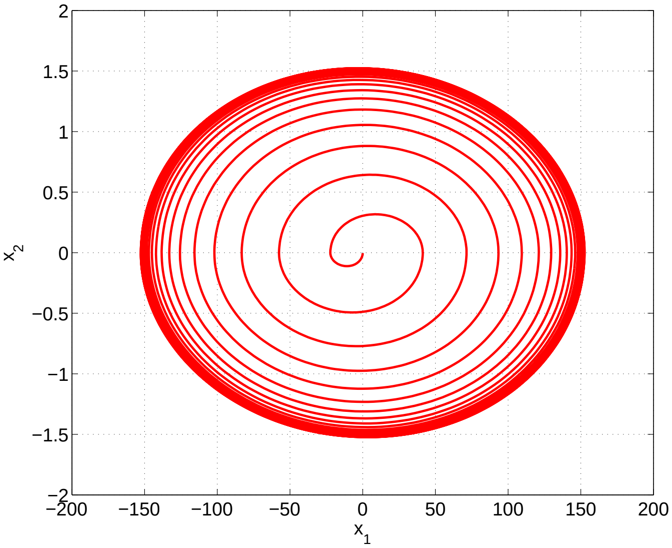

Figure 5.35: Compacted representation of the limit cycle generation in the LLC with $f_0 = 500$ kHz, $R = 10\,\Omega$, $K_l = 10$, $L_s = 31.83\,\mu$H, $L_p = 318.3\,\mu$H, $C_s = 3.18$ nF.

Although the limit cycle can also be represented in a three-dimensional graphic, this new representation method facilitates the validation of the limit cycle generation, giving insight of the stability of the waveforms in a simple graphic.

5.5 Summary

In this chapter a new procedure for analyzing the behavior of 3rd order self-oscillating resonant converters has been introduced. This methodology has allowed to define with accuracy the restrictions required in order to describe analytically the generation of a spiral that eventually becomes a stable limit cycle of elliptic type. In addition, the unconditional stability of the resulting limit cycle has been demonstrated provided that the previous restrictions are accomplished. Finally, a practical application for industrial lightning based on a LCC self-oscillating converter has been designed and its performance has been verified by simulation and experimentally. In this application, different gain limiters have been discussed in order to keep the output voltage inside safe levels.

6

Chapter 6

Fourth order resonant structures: analysis and design

In chapters 3 and 5, the existence of self-oscillation in second and third order resonant converters has been justified by describing analytically the generation of a spiral that converges into an ellipse after having started from zero initial conditions. The study has combined a time-domain analysis to model the spiral and a frequency-domain analysis to describe its final behavior in the limit cycle. As a result, a simple design procedure based on the appropriate selection of the passive elements has emerged.

However, the extension to fourth order converters like LCLC is not straightforward due to the complexity of the time-domain description of the fourth-order differential equations involved. For that reason, the transient-state associated to each pole position will not be exhaustively analyzed as in the mentioned chapters, but rather used as a conjecture to predict which poles will be determinant in the generation of the limit cycle. Besides, the proved fact that the input impedance is resistive in the limit cycle will be used again to eventually establish the design guidelines.

This approach considered, two main operating modes of the LCLC resonant converter are designed for self-oscillation, namely, LCLC working as SRC and LCLC exhibiting a high-gain voltage step-up behavior.

6.1 Amplitude and period of the limit cycle

The amplitude and period of the limit cycle in the LCLC resonant converter depicted in Fig. 1.3e in self-oscillating operation are now investigated. Two cases are considered, each of them corresponding to the pole-zero diagrams depicted in Figs. 6.1a and 6.1b respectively.

The diagram in Fig. 6.1a assumes the same natural oscillation frequency for the two pairs of complex conjugate poles, while the diagram of Fig. 6.1b considers a big difference between the two natural oscillation frequencies. In both cases the constraint $L_sC_s = L_pC_p$ will be introduced in the analysis in order to simplify the design.

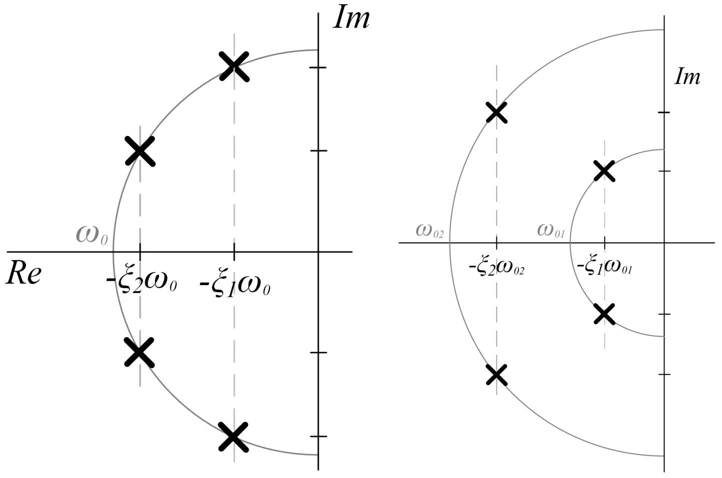

(a) **(b)**

Figure 6.1: Pole-zero diagram of the proposed LCLC converter with: (a) $\omega_{02} = \omega_{01} = \omega_0$, (b) $\omega_{02} >> \omega_{01}$.

6.1.1 Equal natural oscillation frequency

Conjecture

If $\xi_2 >> \xi_1$ in Fig. 6.1a, the self-oscillation will be determined by the complex conjugate pair $-\xi_1\omega_0 \pm j\omega_0\sqrt{1-{\xi_1}^2}$.

Note that in any T_{on} or T_{off} subinterval, the time component associated to the pair of complex conjugate poles $-\xi_2\omega_0 \pm j\omega_0\sqrt{1-{\xi_2}^2}$ will be much more damped exhibiting a very low oscillating frequency, so that it will rapidly decrease to negligible positive values near zero but without crossing this threshold. Therefore, the zero crossings of input inductor current will be determined by the term associated to $-\xi_1\omega_0 \pm j\omega_0\sqrt{1-{\xi_1}^2}$, which is significantly underdamped.

6.1.1.1 Parameter identification

Expressing the normalized parameters ξ_1, ξ_2 and ω_0 of Fig. 6.1a in terms of the converter parameters requires first equating the characteristic polynomial of the LCLC in Table 1.1 with the normalized polynomial derived from the pole-zero diagram as follows:

$$\begin{aligned} &s^4 + \frac{s^3}{RC_p} + \left(\frac{1}{L_pC_p} + \frac{1}{L_sC_s} + \frac{1}{L_sC_p}\right)s^2 + \frac{s}{RC_pL_sC_s} + \frac{1}{L_pC_pL_sC_s} = \\ &= \left(s^2 + 2\xi_1\omega_{01}s + {\omega_{01}}^2\right)\left(s^2 + 2\xi_2\omega_{02}s + {\omega_{02}}^2\right) \end{aligned} \tag{6.1}$$

If $\omega_{02} = \omega_{01}$ is imposed in (6.1) it is found that

$$\omega_0^4 = \frac{1}{L_pL_sC_pC_s} \tag{6.2}$$

Besides, since $L_sC_s = L_pC_p$ then

$${\omega_0}^2 = \frac{1}{L_sC_s} = \frac{1}{L_pC_p} \tag{6.3}$$

Introducing (6.3) and $s = j\omega_0$ into the input impedance transfer function $Zi(s)$ of Table 1.2 yields

$$Zi(j\omega_0) = R. \tag{6.4}$$

Thus, the behavior of the LCLC converter under these conditions is similar to the SRC, where the output is equal to the input at the resonant frequency.

In order to obtain the restrictions for the existence of self-oscillation a relationship between ξ_1 and ξ_2 has to be established. Identifying the coefficients in (6.1) leads to:

$$2(\xi_1 + \xi_2)\omega_0 = \frac{1}{C_pR} \tag{6.5}$$

$$2\omega_0^2(1 + 2\xi_1\xi_2) = \frac{2}{L_sC_s} + \frac{1}{L_sC_p} \tag{6.6}$$

$$2\omega_0^3(\xi_1+\xi_2)=\frac{1}{L_sC_pC_sR} \tag{6.7}$$

Then, from (6.5) it is deduced that

$$\xi_1+\xi_2=\frac{1}{2C_pR\omega_0} \tag{6.8}$$

and from (6.6) it is obtained that

$$\xi_1\xi_2=\frac{\left(\frac{2}{L_sC_s}+\frac{1}{L_sC_p}\right)\frac{1}{2\omega_0^2}-1}{2}=\frac{1}{4\omega_0^2L_sC_p} \tag{6.9}$$

From (6.8) and (6.9) it is derived :

$$\xi^2-\frac{1}{2C_pR\omega_0}\xi+\frac{1}{4\omega_0^2L_sC_p}=0 \tag{6.10}$$

$$\begin{aligned}\xi_{1,2}&=\frac{\frac{1}{2C_pR\omega_0}\pm\sqrt{\frac{1}{4C_p^2R^2\omega_0^2}-\frac{4}{4\omega_0^2L_sC_p}}}{2}=\\&=\frac{1}{4C_pR\omega_0}\pm\frac{1}{4\omega_0}\sqrt{\frac{1}{C_p^2R^2}-\frac{4}{L_sC_p}},\end{aligned} \tag{6.11}$$

which results in

$$\xi_1=\frac{1}{4\omega_0}\left(\frac{1}{C_pR}-\sqrt{\frac{1}{C_p^2R^2}-\frac{4}{L_sC_p}}\right) \tag{6.12}$$

$$\xi_2=\frac{1}{4\omega_0}\left(\frac{1}{C_pR}+\sqrt{\frac{1}{C_p^2R^2}-\frac{4}{L_sC_p}}\right) \tag{6.13}$$

Therefore:

$$\begin{aligned}
\frac{\xi_2}{\xi_1} &= \frac{\frac{1}{C_pR}+\sqrt{\frac{1}{C_p^2R^2}-\frac{4}{L_sC_p}}}{\frac{1}{C_pR}-\sqrt{\frac{1}{C_p^2R^2}-\frac{4}{L_sC_p}}} = \\
&= \frac{\left(\frac{1}{C_pR}+\sqrt{\frac{1}{C_p^2R^2}-\frac{4}{L_sC_p}}\right)^2}{\frac{4}{L_sC_p}} = \\
&= \frac{\frac{2}{C_p^2R^2}-\frac{4}{L_sC_p}+\frac{2}{C_pR}\sqrt{\frac{1}{C_p^2R^2}-\frac{4}{L_sC_p}}}{\frac{4}{L_sC_p}} = \\
&= \frac{1}{2}\frac{\frac{L_s}{C_p}}{R^2}-1+\frac{1}{2}\frac{\frac{L_s}{C_p}}{R^2}\sqrt{1+\frac{4R^2}{\frac{L_s}{C_p}}}
\end{aligned} \tag{6.14}$$

and defining $\frac{\frac{L_s}{C_p}}{R^2}=\kappa$, it can be written that

$$\frac{\xi_2}{\xi_1}=\frac{1}{2}\kappa\left(1+\sqrt{1-\frac{4}{\kappa}}\right)-1\,. \tag{6.15}$$

Then, a minimum κ value of 8 is required, leading to $\xi_2 = 5.82\,\xi_1$. If $\kappa = 4 \Rightarrow \xi_1 = \xi_2$, which does not fulfill the pole separation hypothesis.

6.1.1.2 Design procedure

The previous design-oriented analysis can be summarized in the following steps for a particular design.

Design steps of a Self-oscillating LCLC resonant converter acting as SRC

1. Specify input and output voltage in steady-state.
2. Specify the desired switching frequency ω_0 and the load R.
3. Select an arbitrary C_p value.
4. Determine a value for κ, taking into account that $\kappa \geq 8$ ($\kappa = \frac{L_s}{C_pR}$).
5. Calculate the value of the series inductor L_s from $L_s = \kappa R^2 C_p$
6. Calculate the value of the parallel inductor L_p from $L_p = \frac{1}{\omega_0^2 C_p}$.
7. Calculate the value of the series capacitor C_s from $C_s = \frac{1}{\omega_0^2 L_s}$.

6.1.1.3 Steady-state analysis and two-dimensional representation of the limit cycle

It is also of interest to determine the amplitude and period of the different variables in steady-state.

By simple inspection of the converter at the resonant frequency, the following phasor equations are obtained:

$$\overline{I_{Ls}}(j\omega_0) = \frac{\overline{V_s}(j\omega_0)}{R} \tag{6.16}$$

$$\overline{V_{Cs}}(j\omega_0) = -j\frac{\overline{I_{Ls}}(j\omega_0)}{C_s\omega_0} \tag{6.17}$$

$$\overline{V_{Cp}}(j\omega_0) = \overline{V_s}(j\omega_0) = R\overline{I_{Ls}}(j\omega_0) \tag{6.18}$$

$$\overline{I_{Lp}}(j\omega_0) = \frac{\overline{V_{Cp}}(j\omega_0)}{Lj\omega_0} = -j\frac{\overline{V_s}(j\omega_0)}{L\omega_0} \tag{6.19}$$

Equivalently, in the time-domain:

$$v_{Cp}(t) = v_s cos(\omega_0 t) \tag{6.20}$$

$$i_{Ls}(t) = \frac{v_s}{R}cos(\omega_0 t) \tag{6.21}$$

$$v_{Cs}(t) = \frac{\frac{v_s}{R}}{C_s\omega_0}\sin(\omega_0 t) \tag{6.22}$$

$$i_{Lp}(t) = \frac{v_s}{L_p\omega_0}\sin(\omega_0 t) \tag{6.23}$$

with $v_s = \frac{4V_g}{\pi}$ and $\omega_0 = \frac{1}{\sqrt{L_s C_s}} = \frac{1}{\sqrt{L_p C_p}}$.

Now, a LCLC design example is proposed in order to verify the validity of the previous equations. A switching frequency of 160 kHz and a κ value of 10 are established for a load of $R = 100\,\Omega$ and a DC input voltage V_g of 12 V. Moreover, a parallel capacitor C_p of 10 nF is selected, obtaining the following resonant tank design: $L_s = 1$ mH, $L_p = 100\,\mu$H, $C_s = 1$ nF. Applying these values in (6.20)-(6.23) leads to the expected voltages and currents, which are summarized in Table 6.1. A simulation made with the same parameters and depicted in Fig. 6.2 shows the resulting waveforms. Their peak values are indicated also in Table 6.1. It can be seen a good agreement between the expected values and the simulation results, verifying the validity of the previous analysis.

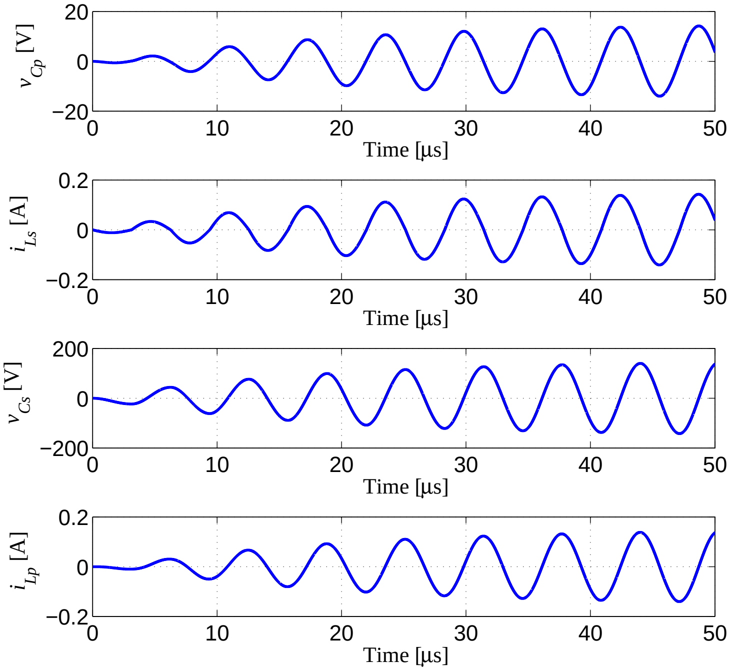

Figure 6.2: Time-domain waveforms of a step-down LCLC with $V_g = 12$ V $f_0 = 160$ kHz, $\kappa = 10$, $R = 100\,\Omega$, $L_s = 1$ mH, $L_p = 0.1$ mH, $C_s = 1$ nF, $C_p = 10$ nF.

Table 6.1: Output parameters in a SRC-like LCLC design example

Parameter	**Theoretical value**	**Simulation result**
$v_{Cp,\,peak}$	15.3 V	15.3 V
$i_{Ls,\,peak}$	153 mA	153 mA
$v_{Cs,\,peak}$	153.6 V	153 V
$i_{Lp,\,peak}$	153 mA	153 mA
f_0	160 kHz	160 kHz

Moreover, it can be seen that $\overline{V_{Cs}}(j\omega_0)$ and $\overline{I_{Lp}}(j\omega_0)$ present a phase-shift of -90° with respect to $\overline{V_{Cp}}(j\omega_0)$ and $\overline{I_{Ls}}(j\omega_0)$, since both phasors are purely imaginary. Therefore, it is possible to visualize the generation of the limit cycle by means of a two-dimensional representation using an appropriate association of signals. Thus, the following signals are associated taking into account the mentioned phase-shift among them:

$$x_1(t) = v_{Cp}(t) + i_{Ls}(t)(\times 1\Omega) \tag{6.24}$$

$$x_2(t) = v_{Cs}(t) + i_{Lp}(t)(\times 1\Omega) \tag{6.25}$$

Fig. 6.3 depicts a compact representation of the limit cycle obtained in the previous simulation example, verifying the stability of the generation.

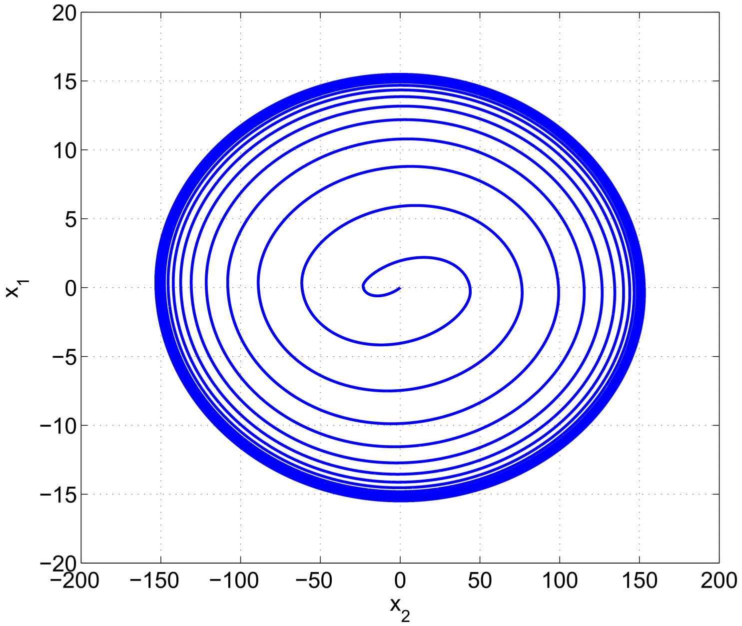

Figure 6.3: Compacted representation of the limit cycle generation in a SRC-like LCLC with $V_g = 12$ V $f_0 = 160$ kHz, $\kappa = 10$, $R = 100\,\Omega$, $L_s = 1$ mH, $L_p = 0.1$ mH, $C_s = 1$ nF, $C_p = 10$ nF.

6.1.2 Different natural oscillation frequency

Conjecture

If $\omega_{02} >> \omega_{01}$ and $\xi_2\omega_{02} >> \xi_1\omega_{01}$ in Fig. 6.1b, the self-oscillation will be determined by the complex conjugate pair $-\xi_2\omega_{02} \pm j\omega_{02}\sqrt{1-\xi_2^2}$.

Note that in any T_{on} or T_{off} subinterval, the time component associated to the pair of complex conjugate poles $-\xi_1\omega_{01} \pm j\omega_{01}\sqrt{1-\xi_1^2}$ will be less damped exhibiting a low oscillating frequency, so that it will be practically constant during the decay of the highly underdamped term created by $-\xi_2\omega_{02} \pm j\omega_{02}\sqrt{1-\xi_2^2}$, whose zero-crossings will establish the change from T_{on} to T_{off} and viceversa.

6.1.2.1 Parameter identification

Taking into account the design constraint $L_sC_s = L_pC_p$, the following identities can be obtained in (6.1):

$$\xi_2\omega_{02} = \frac{1}{2C_pR} \tag{6.26}$$

$$\omega_{02}{}^2 = \frac{2}{L_pC_p} + \frac{1}{L_sC_p} = \frac{2L_s + L_p}{L_sL_pC_p} \tag{6.27}$$

$$\omega_{01}{}^2\omega_{02}{}^2 = \frac{1}{L_p{}^2C_p{}^2} \tag{6.28}$$

$$2\xi_1\omega_{01}\omega_{02}{}^2 + 2\xi_2\omega_{02}\omega_{01}{}^2 = \frac{1}{L_pC_p{}^2R} \tag{6.29}$$

From (6.27) and (6.28), it can be deduced

$$\omega_{01}{}^2 = \frac{\frac{1}{L_p{}^2C_p{}^2}}{\omega_{02}{}^2} = \frac{L_s}{L_pC_p(2L_s + L_p)} \tag{6.30}$$

and from (6.26), (6.27), (6.29) and (6.30) it is derived

$$\xi_1\omega_{01} = \frac{1}{2C_pR}\frac{L_s\left(L_s + L_p\right)}{\left(2L_s + L_p\right)^2} \tag{6.31}$$

Hence, from (6.26) and (6.31) we can write

$$\frac{\xi_2\omega_{02}}{\xi_1\omega_{01}} = \frac{(2L_s + L_p)^2}{L_s(L_s + L_p)} = \frac{\left(\frac{L_p}{L_s} + 2\right)^2}{\frac{L_p}{L_s} + 1} \tag{6.32}$$

Then, in order to satisfy the hypothesis $\xi_2\omega_{02} >> \xi_1\omega_{01}$, a minimum value of the ratio $\frac{L_p}{L_s}$ ($\frac{L_p}{L_s} > 7$) is required since for this value $\frac{\xi_2\omega_{02}}{\xi_1\omega_{01}} > 10$.

Moreover, (6.27) and (6.30) yield

$$\frac{{\omega_{02}}^2}{{\omega_{01}}^2} = \frac{(2L_s + L_p)^2}{{L_s}^2} = \left(\frac{L_p}{L_s} + 2\right)^2 \tag{6.33}$$

Fulfillment of $\frac{\omega_{02}}{\omega_{01}} > 10$ in equation (6.33) will be accomplished if $\frac{L_p}{L_s} > 8$. Consequently, denoting $L_p/L_s = K_l$, a value of K_l greater than 8 has to be selected in order to have self-oscillation in this configuration. Then, the switching frequency will be described by equation (6.27).

6.1.2.2 Input impedance

Introducing the constraint design $L_pC_p = L_sC_s$ in the expression of the input impedance of the LCLC converter given in Table 1.2 results in:

$$Z_{in}(s) = {L_p}^2{C_p}^2 \frac{s^4 + \frac{s^3}{C_pR} + \left(\frac{2}{L_pC_p} + \frac{1}{L_sC_p}\right)s^2 + \frac{s}{L_p{C_p}^2R} + \frac{1}{{L_p}^2{C_p}^2}}{C_s\, s\left(1 + L_pC_ps^2 + \frac{L_p}{R}s\right)} \tag{6.34}$$

Moreover, the assumption of self-oscillation due to the pair of poles $-\xi_2\omega_{02} \pm j\omega_{02}\sqrt{1-{\xi_2}^2}$ suggests that the limit cycle will eventually present an oscillation frequency given by ω_{02}, as it was the case in second and third order converters. Therefore, the input impedance at that frequency must exhibit a resistive behavior.

Particularizing the input impedance at $s = j\omega_{02}$ yields after some manipulations

$$Z_{in}(j\omega_{02}) = \frac{RL_p}{C_s}\frac{K_l(K_l+2)}{(K_l+1)^2R^2 + \frac{L_p}{C_p}(K_l+2)} + j\frac{K_l+1}{C_s\omega_{02}}\frac{R^2 + \frac{L_p}{C_p}(K_l+2)}{(K_l+1)^2R^2 + \frac{L_p}{C_p}(K_l+2)}, \tag{6.35}$$

which implies

$$\tan(\measuredangle Z_{in}(j\omega_{02})) = \frac{\operatorname{Im} Z_{in}(j\omega_{02})}{\operatorname{Re} Z_{in}(j\omega_{02})} = \frac{K_l+1}{\omega_{02}}\frac{R^2 + \frac{L_p}{C_p}(K_l+2)}{RL_pK_l(K_l+2)} \tag{6.36}$$

On the other hand, from (6.27) it can be written

$$\omega_{02} = \sqrt{\frac{2L_s + L_p}{L_sL_pC_p}} = \sqrt{\frac{K_l+2}{L_pC_p}} \tag{6.37}$$

Hence, (6.36) becomes

$$\tan(\measuredangle Z_{in}(j\omega_{02})) = \frac{(K_l+1)\sqrt{\frac{C_p}{L_p}}}{K_l(K_l+2)\sqrt{K_l+2}}\left(R + \frac{L_p}{RC_p}(K_l+2)\right) \tag{6.38}$$

Equivalently,

$$\tan(\measuredangle Z_{in}(j\omega_{02})) = \frac{(K_l+1)}{K_l(K_l+2)^{\frac{3}{2}}}\left(\frac{R}{\sqrt{\frac{L_p}{C_p}}} + \frac{\sqrt{\frac{L_p}{C_p}}}{R}(K_l+2)\right) \tag{6.39}$$

Denominating $Q_p = \frac{R}{\sqrt{\frac{L_p}{C_p}}}$, (6.39) can be expressed as follows:

$$\tan(\measuredangle Z_{in}(j\omega_{02})) = \frac{(K_l+1)}{K_l(K_l+2)^{\frac{3}{2}}}\left(Q_p + \frac{K_l+2}{Q_p}\right) \tag{6.40}$$

For a given value of K_l, the function $f(Q_p) = \left(Q_p + \frac{K_l+2}{Q_p}\right)$ has a minimum at

$$Q_p = \sqrt{K_l+2} \tag{6.41}$$

Therefore, the minimum value of (6.40) will be given by

$$min, \tan(\measuredangle Z_{in}(j\omega_{02})) = \frac{(K_l+1)2\sqrt{K_l+2}}{K_l(K_l+2)^{\frac{3}{2}}} = \frac{2(K_l+1)}{K_l(K_l+2)} \tag{6.42}$$

The optimum value of Q_p given by (6.41) can be selected by choosing the appropriate value of R:

$$R = Q_{p(OPT)}\sqrt{\frac{L_p}{C_p}} = \sqrt{K_l+2}\sqrt{\frac{L_p}{C_p}} \tag{6.43}$$

6.1.2.3 Input to output transfer function

Now, the input-output transfer function $H(s)$ at the switching frequency ($s = j\omega_{02}$) has to be established in order to obtain the output voltage as a function of the resonant tank parameters. In this configuration, the transfer function is obtained from the graphic interpretation of the vectors in the pole-zero diagram, [[114], Section 6.4]. Then, the module of H(s) is described as:

$$|H(s)| = |C|\frac{|(s-z_1)||(s-z_2)|...}{|(s-p_1)||(s-p_2)|...}, \tag{6.44}$$

where C is a constant determined by the resonant tank structure and $|(s-z_n)|$, $|(s-p_n)|$ are the vector modules associated to zeros and poles respectively.

The phase, then, is determined as follows:

$$\measuredangle H(s) = \measuredangle C + [\measuredangle(s-z_1) + \measuredangle(s-z_2) + ...] - [\measuredangle(s-p_1) + \measuredangle(s-p_2) + ...] \quad (6.45)$$

As C is always a real number , its phase is 0 if it is positive or ±180° if it is negative.

Like in Chapter 5, a very small damping factor ξ_2 is assumed, so that

$$\omega_{d2} \simeq \omega_{02} \quad (6.46)$$

as ${\omega_{d2}}^2 = {\omega_{02}}^2(1-{\xi_{02}}^2)$.

In order to proceed with the analysis, first the constant C has to be established. From the LCLC input-output transfer function $H(s)$ in Table 1.1, it is obtained that

$$H(s) = \frac{\frac{1}{L_sC_p}s^2}{s^4 + \frac{s^3}{RC_p} + \left(\frac{1}{L_pC_p} + \frac{1}{L_sC_s} + \frac{1}{L_sC_p}\right)s^2 + \frac{s}{RC_pL_sC_s} + \frac{1}{L_pC_pL_sC_s}} = \frac{N(s)}{D(s)} \quad (6.47)$$

Hence,

$$C = \frac{1}{L_sC_p} \quad (6.48)$$

Then, the module of the vectors established by the zeros and poles of the system has to be determined from their graphic representation. Fig. 6.4 identifies the vectors in the pole-zero diagram evaluated at $s = j\omega_{02}$, taking into account that $\omega_{d2} \simeq \omega_{02}$. In the case of D_1, the module coincides with the length of the real part of the pole. Then,

$$|D_1| = \xi_2\omega_{02}. \quad (6.49)$$

The modules of the rest of the poles are described by the length of the hypotenuse of the triangles existent between the axes and the vectors. As $\xi_2 << 1$, these modules can be approximated by the length of the vertical cathetus corresponding to each vector. Therefore,

$$|D_2| = 2\omega_{02}\,, \quad (6.50)$$

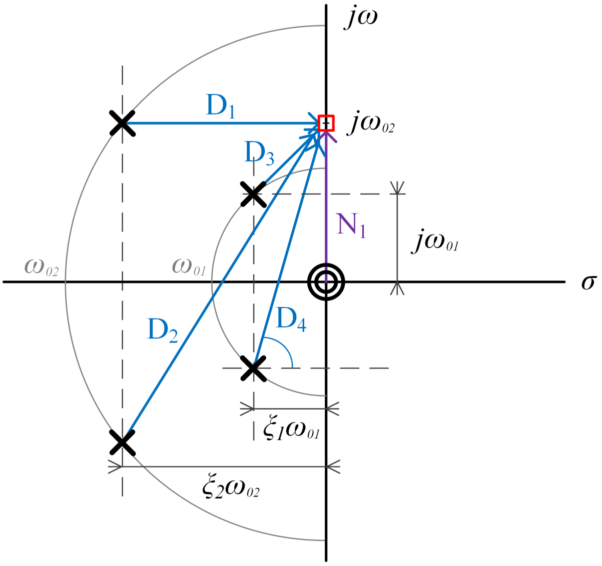

Figure 6.4: Pole-zero diagram of the proposed LCLC converter evaluated at $s = j\omega_{02}$.

$$|D_3| = \omega_{02} - \omega_{01}\ , \tag{6.51}$$

$$|D_4| = \omega_{02} + \omega_{01}\ . \tag{6.52}$$

Similarly, the module of the vector N_1 is described by the length of the segment from the zeros to the evaluation point. Then,

$$|N_1| = {\omega_{02}}^2. \tag{6.53}$$

Note the inclusion of the square factor due to the existence of a double zero.

Then, for establishing the value of $|H(j\omega_{02})|$, the parameters obtained [(6.48), (6.49)-(6.53)] have to be introduced in (6.44), leading to

$$\begin{aligned} |H(j\omega_{02})| &= \frac{1}{L_sC_p}\frac{|N_1|}{|D_1||D_2||D_3||D_4|} \simeq \\ &\simeq \frac{{\omega_{02}}^2\frac{1}{L_sC_p}}{\xi_2\omega_{02}2\omega_{02}\left(\omega_{02}-\omega_{01}\right)\left(\omega_{02}+\omega_{01}\right)} = \\ &= \frac{\frac{1}{L_sC_p}}{2\xi_2\left({\omega_{02}}^2-{\omega_{01}}^2\right)} \simeq \frac{1}{L_sC_p2\xi_2{\omega_{02}}^2} = \\ &= \frac{1}{2\xi_2}\frac{1}{L_sC_p}\frac{L_pC_p}{K_l+2} = \frac{K_l}{K_l+2}\frac{1}{2\xi_2} = \frac{K_l}{K_l+2}\frac{1}{2}2C_pR\omega_{02} = \\ &= \frac{K_l}{K_l+2}C_pR\sqrt{\frac{K_l+2}{L_pC_p}} = \frac{K_l}{\sqrt{K_l+2}}\sqrt{\frac{C_p}{L_p}}R = \boxed{\frac{K_l}{\sqrt{K_l+2}}Q_p}, \end{aligned} \tag{6.54}$$

where $K_l = \frac{L_p}{L_s}$ and $Q_p = \frac{R}{\sqrt{\frac{L_p}{C_p}}}$.

For the optimum value of Q_p given by (6.41), expression (6.54) becomes

$$|H(j\omega_{02})| = K_l \tag{6.55}$$

Besides, as $\xi_2 << 1$, the phase of the input-output transfer function can be approximated as

$$\measuredangle H(j\omega_{02}) = 2\measuredangle N_1 - \measuredangle D_2 - \measuredangle D_3 - \measuredangle D_4 \simeq 180^\circ - 90^\circ - 90^\circ - 90^\circ = -90^\circ. \tag{6.56}$$

6.1.2.4 Design procedure

A simple design procedure, derived from the previous equations, is summarized next:

Design steps of a self-oscillating LCLC resonant converter for high-gain voltage step-up operation

1. Specify gain ($H(j\omega_0) = K_l$, $K_l > 8$), load resistance R and oscillation frequency ω_0.
2. Obtain the value of the parallel capacitor C_p from $C_p = \frac{K_l+2}{R\omega_0}$
3. Calculate the value of the series capacitor C_s from $C_s = K_lC_p$.
4. Calculate the value of the parallel inductor L_p from $L_p = \frac{K_l+2}{{\omega_0}^2C_p}$.
5. Determine the value of the series inductor L_s from $L_s = \frac{L_p}{K_l}$.

Following the previous procedure, a LCLC design example is proposed and its response is verified by simulation. An input voltage of 12 V and a gain of 10 are established for a load of 15 Ω and a switching frequency of 500 kHz. The expected output voltage, then, is 157 V. The resulting resonant tank parameters applying the previous specifications are summarized in Table 6.2 and the results obtained by simulation with the proposed converter are shown in Fig. 6.5. It can be seen that the peak output voltage coincides with the desired one. Moreover, the resulting switching frequency is equal to the specified in the design, validating the previous procedure. However, a large circulating current is observed in the resonant tank.

Table 6.2: Parameters of the step-up self-oscillating LCLC design example with R=15 Ω.

Parameter	**Value**
K_l	10
C_p	255 nF
C_s	2.5 μF
L_p	4.7 μH
L_s	470 nH

Therefore, a new design example with a higher load resistance is proposed. An output voltage of 1000 V is desired for a load of 36 kΩ and the same input voltage and switching frequency as in the previous example. Consequently, the resonant tank design in Table 6.3 is obtained. The results obtained with this configuration are shown in Fig. 6.6. As in the previous example, the output voltage and the switching frequency of the simulation are in perfect agreement with the expected values, confirming the correctness of the previous design procedure. In addition, a reduced circulating current is observed due to the large load imposed. Therefore, the use of the self-oscillating step-up LCLC converter is only recommended when high output voltages and low output powers are desired.

Table 6.3: Parameters of the step-up self-oscillating LCLC design example with R=36 kΩ.

Parameter	**Value**
K_l	66
C_p	600 pF
C_s	40 nF
L_p	11.5 mH
L_s	174 μH

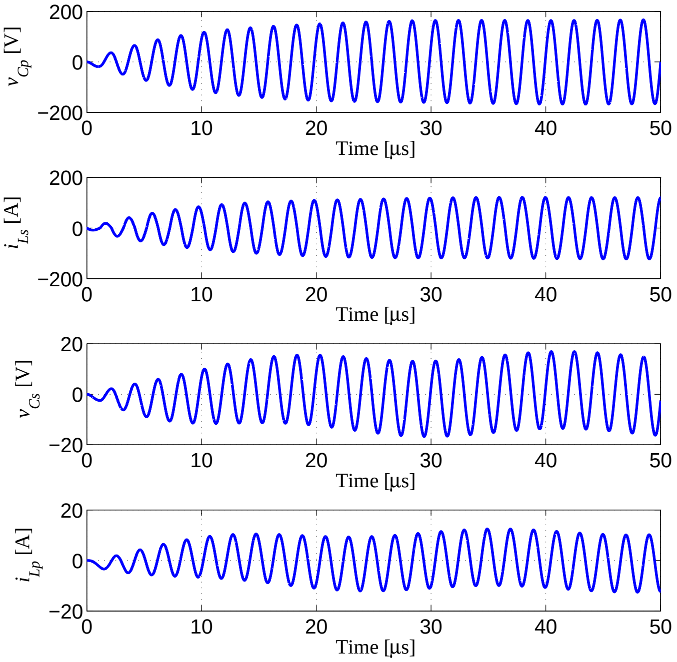

Figure 6.5: Time-domain waveforms of a step-up LCLC with $V_g = 12$ V, $f_0 = 500$ kHz, K_l=10 and $R = 15\,\Omega$.

6.2 Summary

In this chapter, the design guidelines for a self-oscillating LCLC resonant converter have been derived for two different modes, i.e., SRC and high gain voltage step-up characteristics. Unlike in second and third order converters, the resulting design in each case is based on a conjecture and not in a detailed analysis in the time-domain. This conjecture suggests the pair of poles that eventually would cause the self-oscillation.

Under the constraint $L_pC_p = L_sC_s$, big separation between two possible pairs of poles, and the same natural oscillation frequency for both of them, the self-oscillation is assumed to be caused by the nearest pair of poles to the imaginary axis. Under this assumption, the subsequent steady-state analysis of the input impedance is similar to that developed in second and third order structures. Namely, the oscillating frequency of the limit cycle is the natural oscillation frequency of the mentioned pair of poles. As a result, a self-oscillation is produced in the LCLC converter that behaves like a SRC converter.

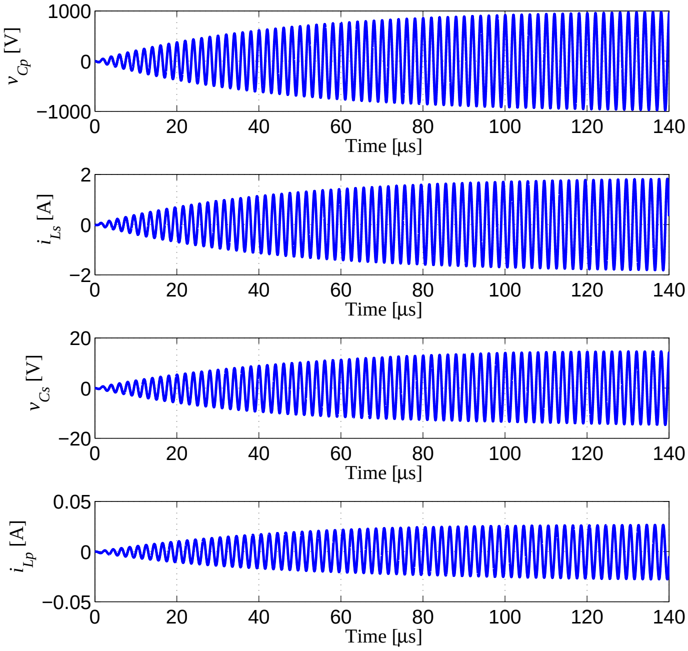

Figure 6.6: Time-domain waveforms of a step-up LCLC with $V_g = 12$ V, $V_{Cp} = 1000$ V, $f_0 = 500$ kHz, K_l=66 and $R = 36\,k\Omega$.

The same constraint and assumption on the pair of poles separation but considering different natural oscillation frequencies suggest a self-oscillation generation similar to the one in third order converters, i.e., provoked by the farthest pair of poles from the imaginary axis. The subsequent analysis of the limit cycle in steady-state reveals that the self-oscillating LCLC operates as high-gain voltage step-up system.

7

CHAPTER 7
CONCLUSIONS

It is well-known that resonant conversion is extensively used in industry due to the inherent advantages derived from soft-switching such as low switching losses, high switching frequency operation, and reduced volume and weight of the converter.

Most resonant converters are regulated through a voltage-controlled oscillator that modifies the switching frequency following the signal provided by the controller. The latter processes the output voltage error and is designed taking into account the dynamic response of the converter assuming that its state variables have the nature of band-pass (FM) signals.

Only few resonant converters have been used in self-oscillating operation. All the examples found in the literature are different cases of self-oscillation without relation among them, i.e., every reported case is a particular solution. However, all examples share the problem of delay in the control feedback path.

It could be ventured to say that the lack of a general approach to describe the resonant converters in self-oscillating operation have prevented its development for many industrial applications. This problematic issue has been addressed in this dissertation.

Self-oscillation has been here generated by the appropriate use of the input inductor current zero-crossings to change the polarity of the input voltage. As a result, the input current and the first harmonic of the input voltage are in phase, which ensures a unity power factor to the steady-state operation of the resonant converter. This fact confers a nature of loss-free resistor (LFR) to the two-port description of the converter. The self-oscillation generating mechanism has been proven to be effective in second, third and fourth order structures.

Although the self-oscillation generation is a relatively simple task, the analytical description of the generation is more involved. It combines time-domain and frequency-domain analyses to justify that a spiral starting from zero initial conditions eventually converges into an ellipse that corresponds to the steady-state behavior of the limit cycle. The stability of the generation has been demonstrated by proving the stability of the resulting discrete recurrence considering two successive zero-crossings of the input inductor current after completing a generic oscillation cycle. This approach has successfully explained the generation of two-dimension and three-dimension spirals in second and third order converters respectively.

The extension of the previous analytical procedure to fourth order converters has been interrupted by the complexity of the time-domain analysis involved. Instead, a conjecture on the dominant poles eventually provoking self-oscillation has been successfully used to predict the amplitude and period of the limit cycle in two different operation modes that share the same design constraint. The assumption about the dominant poles on the spiral generation has been analytically complemented by the fact that the input impedance is resistive at the oscillation frequency of the limit cycle.

An interesting property has arisen in the analysis of third and fourth order converters, i.e., the existence of pairs of variables in phase between them and 90° phase-shifted with respect to the rest of variables. This fact has allowed a two-dimensional description of the spiral generation by means of appropriate combinations of the in-phase variables and their posterior assignment to the Cartesian axes of the phase-plane for a compact representation.

Self-oscillating resonant converters with the previous mechanism to generate oscillations are a simple procedure to transmit power from a DC source to an AC load. However, when perturbations from input voltage or output load penetrate into the system, the amplitude of the output voltage sinusoidal signal is directly affected. Hence, a voltage regulation loop has to be added.

Inserting a voltage regulation loop has required modeling the dynamic behavior of the self-oscillating resonant converter whose switching law is a linear combination of the input inductor current and the output voltage. Relating the variations of the constant of that linear combination to the changes of the switching frequency is the key aspect of the modeling, which has been carried out for second order converters. The resulting closed-loop regulation based on this model exhibits larger bandwidth and a better robustness degree than conventional frequency modulation-based controllers.

Potential applications of this class of resonant converters in industry have been explored in two cases, namely, wireless power transfer and electronic ballast design for IEFL lamps showing promising results in both cases. The problem of delay in the control feedback path has emerged in the wireless power transfer due to the high switching frequency employed (6.78 MHz). The use of an ad-hoc active network to compensate the delay has contributed to the correct operation of the self-oscillating converter.

List of Acronyms, Parameters and Variables

A4WP Alliance for Wireless Power

AM Amplitude Modulation

CST Current Sense Transformer

FM Frequency Modulation

GaN Gallium Nitride

IEFL Induction Electrodeless Fluorescent Lamp

LCC Series-parallel LCC-type Resonant Converter

LLC Series-parallel LLC-type Resonant Converter

LCLC Series-parallel LCLC-type Resonant Converter

PRC Parallel Resonant Converter

PWM Pulse Width Modulated

SRC Series Resonant Converter

VCO Voltage Controlled Oscillator

VSS Variable Structure System

WPT Wireless Power Transfer

ZCS Zero Current Switching

ZVS Zero Voltage Switching

C Resonant tank capacitor

C_{in} Converter input capacitor

C_f Filter capacitor

C_p Resonant tank parallel capacitor

C_s Resonant tank series capacitor

f_{sw} Switching frequency of the converter in Hz

f_0 Resonance frequency of the converter in Hz

f_c Crossing frequency

G_M Gain margin

$\phi_{\mathbf{M}}$ Phase margin

H Input to output voltage transfer function

i_{DC} Current across the DC output

i_f Current across the filter

i_g Converter input current

i_L Current across the resonant tank inductor

i_{out} Current across the load

j_L Normalized current across the resonant tank inductor

K_c Relationship between series and parallel capacitor (C_s/C_p)

K_l Relationship between parallel and series inductor (L_p/L_s)

$k(t)$ Slope of the switching boundary

L Resonant tank inductor

L_f Filter inductor

L_s Resonant tank series inductor

L_p Resonant tank parallel inductor

m_C Normalized voltage across the resonant tank output capacitor

Q Quality factor of a resonant converter

R Load at the output of the resonant tank

R_L Load at the output of the converter if a rectifier is used

R_{SENS} Current sense resistor

R_{eq} Equivalent load seen at the output of the resonant tank if a rectifier is used $(R_{eq} = (R_L\pi)/8)$

$sg(x)$ Sign dependent function. It is 1 if $x \geq 0$ and 0 if $x < 0$

S_x FET switch number X

u Structure control variable

V_g Converter input voltage

v_C Resonant tank output voltage

v_{Cp}	Voltage of the parallel capacitor
v_{Cs}	Voltage of the series capacitor
v_{C2n}	Voltage of the capacitor at the n^{th} crossing over the switching boundary
v_{Cs2n}	Voltage of the series capacitor at the n^{th} crossing over the switching boundary
v_{Cp2n}	Voltage of the parallel capacitor at the n^{th} crossing over the switching boundary
V_C	Voltage of the capacitor at the limit cycle
V_{Cs}	Voltage of the series capacitor at the limit cycle
V_{Cp}	Voltage of the parallel capacitor at the limit cycle
v_{DC}	DC output voltage
v_s	Resonant tank input voltage
v_{s1}	First harmonic of the resonant tank input voltage
Y	Inductor current to input voltage transfer function
Z_i	Resonant tank input impedance
Z_o	Resonant tank output impedance
ω_0	Resonance frequency of the converter in rad/s
ω_m	Damped oscillation frequency of the converter
ω_{sw}	Switching frequency of the converter in rad/s
τ	Time constant
ξ	Damping ratio coefficient
Δx	Difference between two values of variable x
$\|x\|$	Absolute value of variable x
x^*	Complex conjugate of variable x
$\hat{x}$	Small-signal value of variable x

LIST OF FIGURES

LIST OF TABLES

BIBLIOGRAPHY

[1] J. Blanchard, "The history of electrical resonance," *Bell System Technical Journal*, October 1941. (Cited in page 2.)

[2] G. A. Covic and J. T. Boys, "Inductive power transfer," *Proceedings of the IEEE*, vol. 101, no. 6, pp. 1276–1289, 2013. (Cited in page 2.)

[3] H. Hertz, "On very rapid electrical oscillations," *Electric Waves*, 1887. (Cited in page 2.)

[4] R. Severns, "History of soft switching," *Switching Power Magazine*, January 2001. (Cited in pages 2 and 159.)

[5] *Mallory Vibrator Data Handbook.* R.R. Mallory and Co, 1947. (Cited in page 2.)

[6] Caldwell and Wagner, "Boosting power transistor efficiency," *Electronics magazine*, p. 88, November 1958. (Cited in page 2.)

[7] R. Goldfarb, "A new non-dissipative load-line shaping technique eliminates switching stress in bridge converters," in *Powercon8 proceedings*, 1981, Conference Proceedings, pp. D4–1 – D4–6. (Cited in page 2.)

[8] B. Carsten, "High power SMPS require intrinsic reliability," *PCIM81 proceedings*, pp. 118–133, September 1981. (Cited in page 2.)

[9] J. P. Jordan, "Application of vacuum-tube oscillators to inductive and dielectric heating in industry," *Electrical Engineering*, vol. 61, no. 11, pp. 831–834, Nov 1942. (Cited in page 3.)

[10] J. A. Ferreira and E. H. Roos, "100 kHz to 1 MHz converter to generate 1 kVA to 100 kVA high intensity magnetic fields," in *Power Electronics and Variable-Speed Drives, 1991., Fourth International Conference on*, Jul 1990, pp. 484–487. (Cited in page 3.)

[11] I. H. Lee, S. H. Oh, H. J. Kim, and T. Y. Ahn, "A 2 MHz resonant DC/DC converter module for telecommunication application," in *Telecommunications Energy Conference, 1991. INTELEC '91., 13th International*, Nov 1991, pp. 502–508. (Cited in page 3.)

[12] R. N. do Prado, A. R. Seidel, F. E. Bisogno, and M. A. D. Costa, "A design method for electronic ballast for fluorescent lamps," in *Industrial Electronics Society, 2000. IECON 2000. 26th Annual Confjerence of the IEEE*, vol. 4, 2000, pp. 2279–2284 vol.4. (Cited in pages 3 and 10.)

[13] A. R. Seidel, F. E. Bisogno, H. Pinheiro, and R. N. do Prado, "Self-oscillating dimmable electronic ballast," *IEEE Transactions on Industrial Electronics*, vol. 50, no. 6, pp. 1267–1274, Dec 2003. (Cited in pages 3 and 10.)

[14] W. Feng and F. C. Lee, "Optimal trajectory control of LLC resonant converters for soft start-up," *IEEE Transactions on Power Electronics*, vol. 29, no. 3, pp. 1461–1468, March 2014. (Cited in page 3.)

[15] R. W. Schnell, R. A. Zane, and F. J. Azcondo, "Size reduction in low-frequency square-wave ballasts for high-intensity discharge lamps using soft-saturation magnetic material and digital control techniques," *IEEE Transactions on Power Electronics*, vol. 28, no. 2, pp. 1036–1046, Feb 2013. (Cited in page 3.)

[16] P. D. Teodosescu, M. Bojan, and R. Marschalko, "Resonant LED driver with inherent constant current and power factor correction," *Electronics Letters*, vol. 50, no. 15, pp. 1086–1088, July 2014. (Cited in page 3.)

[17] O. Lucia, J. M. Burdio, I. Millan, J. Acero, and D. Puyal, "Load-adaptive control algorithm of half-bridge series resonant inverter for domestic induction heating," *IEEE Transactions on Industrial Electronics*, vol. 56, no. 8, pp. 3106–3116, Aug 2009. (Cited in page 3.)

[18] H. Sarnago, O. Lucia, A. Mediano, and J. M. Burdio, "High-efficiency parallel quasi-resonant current source inverter featuring SiC metal-oxide semiconductor field-effect transistors for induction heating systems with coupled inductors," *IET Power Electronics*, vol. 6, no. 1, pp. 183–191, Jan 2013. (Cited in page 3.)

[19] H. D. Clercq and R. Puers, "A wireless energy transfer platform, integrated at the bedside," in *2013 35th Annual International Conference of the IEEE Engineering in Medicine and Biology Society (EMBC)*, July 2013, pp. 1458–1461. (Cited in page 3.)

[20] P. S. Riehl, A. Satyamoorthy, H. Akram, Y. C. Yen, J. C. Yang, B. Juan, C. M. Lee, F. C. Lin, V. Muratov, W. Plumb, and P. F. Tustin, "Wireless power systems for mobile devices supporting inductive and resonant operating modes," *IEEE Transactions on Microwave Theory and Techniques*, vol. 63, no. 3, pp. 780–790, March 2015. (Cited in pages 3 and 42.)

[21] R. W. Erickson and D. Maksimovic, *Fundamentals of Power Electronics*, 2nd ed. Springer US, 2001. (Cited in pages 8, 9, 24, 60, and 103.)

[22] G. Ivensky, S. Bronshtein, and A. Abramovitz, “Approximate analysis of resonant llc dc-dc converter,” *IEEE Transactions on Power Electronics*, vol. 26, no. 11, pp. 3274–3284, Nov 2011. (Cited in page 9.)

[23] J. G. Hayes and M. G. Egan, “Rectifier-compensated fundamental mode approximation analysis of the series parallel lclc family of resonant converters with capacitive output filter and voltage-source load,” in *Power Electronics Specialists Conference, 1999. PESC 99. 30th Annual IEEE*, vol. 2, 1999, pp. 1030–1036 vol.2. (Cited in page 9.)

[24] R. Farrington, M. M. Jovanovic, and F. C. Lee, “Design oriented analysis of reactive power in resonant converters,” *IEEE Transactions on Power Electronics*, vol. 8, no. 4, pp. 411–422, Oct 1993. (Cited in page 9.)

[25] P. P. Roy, S. R. Doradla, and S. Deb, “Analysis of the series resonant converter using a frequency domain model,” in *Power Electronics Specialists Conference, 1991. PESC ’91 Record., 22nd Annual IEEE*, Jun 1991, pp. 482–489. (Cited in page 9.)

[26] R. M. Nelms, “Harmonic analysis of a parallel-loaded resonant converter,” *IEEE Transactions on Aerospace and Electronic Systems*, vol. 27, no. 4, pp. 683–688, Jul 1991. (Cited in page 9.)

[27] C. P. Dick, “Multi-resonant converters as photovoltaic module-integrated maximum power point tracker,” Ph.D. dissertation, RWTH Aachen University, 2010. (Cited in page 9.)

[28] S. Sooksatra, “A unified approach to the classification and analyses of resonant converters,” Ph.D. dissertation, University of Illinois at Chicago, 1991. (Cited in page 9.)

[29] Y. Yin, R. Zane, J. Glaser, and R. W. Erickson, “Small-signal analysis of frequency-controlled electronic ballasts,” *IEEE Transactions on Circuits and Systems I: Fundamental Theory and Applications*, vol. 50, no. 8, pp. 1103–1110, Aug 2003. (Cited in pages 9 and 57.)

[30] R. Pique and L. Martinez, “Computer-aided large-signal analysis and control of the parallel resonant converter,” in *Computers in Power Electronics, 1992., IEEE Workshop on*, 1992, pp. 67–80. (Cited in pages 9 and 57.)

[31] A. K. S. Bhat and M. M. Swamny, “Analysis and design of a parallel resonant converter including the effect of a high-frequency transformer,” *IEEE Transactions on Industrial Electronics*, vol. 37, no. 4, pp. 297–306, Aug 1990. (Cited in pages 9 and 57.)

[32] Y. Yin, R. Zane, R. W. Erickson, and J. Glaser, “Direct modeling of envelope dynamics in resonant inverters,” in *IEEE Power Electronics Specialist Conference (PESC)*, vol. 3, 15-19 June 2003, pp. 1313–1318. (Cited in pages 9,

57, and 60.)

[33] J. Sebastian, M. Rico, J. Uceda, and F. Aldana, “Regulated self-oscillating resonant converters,” in *European Power Electronics Conference (EPE)*, 1987, pp. 245–249. (Cited in page 9.)

[34] D. R. Williams, C. Bingham, D. A. Stone, M. P. Foster, and A. Gilbert, “Analysis of self-oscillating DC-DC resonant power converters using a hysteretic relay,” in *Power Electronics and Applications, 2007 European Conference on*, 2007, Conference Proceedings, pp. 1–9. (Cited in page 9.)

[35] D. Williams, C. Bingham, M. Foster, and D. Stone, “Hamel locus design of self-oscillating DC-DC resonant converters,” *IET Power Electronics*, vol. 3, no. 1, pp. 86–94, 2010. (Cited in pages 9 and 10.)

[36] V. Vorperian, “Approximate small-signal analysis of the series and the parallel resonant converters,” *IEEE Transactions on Power Electronics*, vol. 4, no. 1, pp. 15–24, 1989. (Cited in page 9.)

[37] C. T. Rim and G. H. Cho, “Phasor transformation and its application to the DC/AC analyses of frequency phase-controlled series resonant converters (SRC),” *IEEE Transactions on Power Electronics*, vol. 5, no. 2, pp. 201–211, 1990. (Cited in page 9.)

[38] S. Glozman and S. Ben-Yaakov, “Dynamic interaction analysis of HF ballasts and fluorescent lamps based on envelope simulation,” *IEEE Transactions on Industry Applications*, vol. 37, no. 5, pp. 1531–1536, 2001. (Cited in page 9.)

[39] H. Pinheiro, P. K. Jain, and G. Joos, “Self-sustained oscillating resonant converters operating above the resonant frequency,” *Power Electronics, IEEE Transactions on*, vol. 14, no. 5, pp. 803–815, 1999. (Cited in pages 9 and 10.)

[40] R. Oruganti and F. C. Lee, “Resonant power processors, part I—state plane analysis,” *IEEE Transactions on Industry Applications*, vol. IA-21, no. 6, pp. 1453–1460, 1985. (Cited in page 10.)

[41] ——, “Resonant power processors, part II - methods of control,” *IEEE Transactions on Industry Applications*, vol. IA-21, no. 6, pp. 1461–1471, 1985. (Cited in page 10.)

[42] A. J. Gilbert, C. M. Bingham, D. A. Stone, and M. P. Foster, “Self-oscillating control methods for the LCC current-output resonant converter,” *Power Electronics, IEEE Transactions on*, vol. 23, no. 4, pp. 1973–1986, 2008. (Cited in page 10.)

[43] H. Sira-Ramirez and R. Silva-Ortigoza, “On the control of the resonant converter: a hybrid-flatness approach,” in *Proc. 15th International Symposium on Mathematical Theory of Networks and Systems*, 2002. (Cited in pages 10, 16, and 18.)

[44] H. Molla-Ahmadian, F. Tahami, A. Karimpour, and N. Pariz, “Hybrid control of DC-DC series resonant converters: The direct piecewise affine approach,” *IEEE Transactions on Power Electronics*, vol. 30, no. 3, pp. 1714–1723, 2015. (Cited in pages 10 and 18.)

[45] M. Momeni, H. M. Kelk, and H. Talebi, “Rotating switching surface control of series-resonant converter based on a piecewise affine model,” *IEEE Transactions on Power Electronics*, vol. 30, no. 3, pp. 1762–1772, 2015. (Cited in pages 10, 14, and 18.)

[46] M. G. Kim, D. S. Lee, and M. J. Youn, “A new state feedback control of resonant converters,” *IEEE Transactions on Industrial Electronics*, vol. 38, no. 3, pp. 173–179, 1991. (Cited in pages 10, 18, and 68.)

[47] L. Rossetto, “A simple control technique for series resonant converters,” *IEEE Transactions on Power Electronics*, vol. 11, no. 4, pp. 554–560, 1996. (Cited in pages 10 and 14.)

[48] A. J. Gilbert, C. M. Bingham, D. A. Stone, and M. P. Foster, “Normalized analysis and design of LCC resonant converters,” *Power Electronics, IEEE Transactions on*, vol. 22, no. 6, pp. 2386–2402, 2007. (Cited in page 10.)

[49] A. B. Carlson and P. B. Crilly, *Communication Systems.* McGraw-Hill Education, 2009. (Cited in page 10.)

[50] J. C. Hsieh and J. L. Lin, “Novel single-stage self-oscillating dimmable electronic ballast with high power factor correction,” *IEEE Transactions on Industrial Electronics*, vol. 58, no. 1, pp. 250–262, Jan 2011. (Cited in page 10.)

[51] O. Jimenez, O. Lucía, I. Urriza, L. A. Barragan, and D. Navarro, “Power measurement for resonant power converters applied to induction heating applications,” *IEEE Transactions on Power Electronics*, vol. 29, no. 12, pp. 6779–6788, Dec 2014. (Cited in page 11.)

[52] H. Ma, J. S. . Lai, C. Zheng, and P. Sun, “A high-efficiency quasi-single-stage bridgeless electrolytic capacitor-free high-power AC-DC driver for supplying multiple LED strings in parallel,” *IEEE Transactions on Power Electronics*, vol. 31, no. 8, pp. 5825–5836, Aug 2016. (Cited in page 11.)

[53] Y. Wang, Y. Guan, X. Liang, W. Wang, and D. Xu, “Two-stage LED street lighting system based on a novel single-stage AC/DC converter,” *IET Power Electronics*, vol. 7, no. 6, pp. 1374–1383, June 2014. (Cited in page 11.)

[54] X. Wu, C. Hu, J. Zhang, and Z. Qian, “Analysis and design considerations of LLCC resonant multioutput DC/DC LED driver with charge balancing and exchanging of secondary series resonant capacitors,” *IEEE Transactions on Power Electronics*, vol. 30, no. 2, pp. 780–789, Feb 2015. (Cited in page 11.)

[55] C. Chang, J. Chang, and G. W. Bruning, “Analysis of the self-oscillating

series resonant inverter for electronic ballasts," *IEEE Transactions on Power Electronics*, vol. 14, no. 3, pp. 533–540, May 1999. (Cited in page 11.)

[56] H. S. Han, T. H. Ryu, and G. H. Cho, "Mixed mode excitation and low cost control ic for electronic ballast," *IEEE Transactions on Power Electronics*, vol. 22, no. 3, pp. 871–880, May 2007. (Cited in page 11.)

[57] M. Kadota, H. Shoji, and S. Furuya, "A dimming method for hot cathode fluorescent lamp using a resonant inverter operating at fixed switching frequency," *IEEE Transactions on Power Electronics*, vol. 30, no. 4, pp. 2253–2261, April 2015. (Cited in page 11.)

[58] Y. J. Choi, S. Y. Choi, and R. Y. Kim, "An integrated voltage-current compensator of LLC resonant converter for Li-ion battery charger applications," in *2016 IEEE 8th International Power Electronics and Motion Control Conference (IPEMC-ECCE Asia)*, May 2016, pp. 3783–3790. (Cited in page 11.)

[59] J. Park, M. Kim, and S. Choi, "Zero-current switching series loaded resonant converter insensitive to resonant component tolerance for battery charger," *IET Power Electronics*, vol. 7, no. 10, pp. 2517–2524, 2014. (Cited in page 11.)

[60] H. Wang, "A phase shift full bridge based reconfigurable PEV onboard charger with extended ZVS range and zero duty cycle loss," in *2016 IEEE Applied Power Electronics Conference and Exposition (APEC)*, March 2016, pp. 480–486. (Cited in page 11.)

[61] J. Deng, C. C. Mi, R. Ma, and S. Li, "Design of LLC resonant converters based on operation-mode analysis for level two PHEV battery chargers," *IEEE/ASME Transactions on Mechatronics*, vol. 20, no. 4, pp. 1595–1606, Aug 2015. (Cited in page 11.)

[62] K. H. Chao and M. S. Yang, "High step-up interleaved converter with soft-switching using a single auxiliary switch for a fuel cell system," *IET Power Electronics*, vol. 7, no. 11, pp. 2704–2716, 2014. (Cited in page 11.)

[63] U. K. Madawala and D. J. Thrimawithana, "Modular-based inductive power transfer system for high-power applications," *IET Power Electronics*, vol. 5, no. 7, pp. 1119–1126, August 2012. (Cited in page 11.)

[64] C. Zheng, B. Chen, L. Zhang, R. Chen, and J. S. Lai, "Design considerations of LLC resonant converter for contactless laptop charger," in *2015 IEEE Applied Power Electronics Conference and Exposition (APEC)*, March 2015, pp. 3341–3347. (Cited in page 11.)

[65] V. Utkin, "Variable structure systems with sliding modes," *IEEE Transactions on Automatic Control*, vol. 22, no. 2, pp. 212–222, 1977. (Cited in page 14.)

[66] S. Singer, "Realization of loss-free resistive elements," *IEEE Transactions on*

Circuits and Systems, vol. 37, no. 1, pp. 54–60, Jan 1990. (Cited in page 16.)

[67] ——, "The application of loss-free resistors in power processing circuits," *IEEE Transactions on Power Electronics*, vol. 6, no. 4, pp. 595–600, Oct 1991. (Cited in page 16.)

[68] L. Katzir, S. Singer, and D. Shmilovitz, "Resonant converter with loss free resistor characteristic," in *2005 IEEE 36th Power Electronics Specialists Conference*, June 2005, pp. 656–659. (Cited in page 16.)

[69] R. V. Langmuir, "Repetitively switched circuits," *IEEE Transactions on Aerospace and Electronic Systems*, vol. AES-9, no. 1, pp. 59–64, Jan 1973. (Cited in pages 24 and 66.)

[70] L. Martínez-Salamero, G. García, M. Orellana, C. Lahore, and B. Estibals, "Start-up control and voltage regulation in a boost converter under sliding-mode operation," *IEEE Transactions on Industrial Electronics*, vol. 60, no. 10, pp. 4637–4649, Oct 2013. (Cited in page 24.)

[71] I. Babaa, T. Wilson, and Y. Yu, "Analytic solutions of limit cycles in a feedback-regulated converter system with hysteresis," *IEEE Transactions on Automatic Control*, vol. 13, no. 5, pp. 524–531, Oct 1968. (Cited in page 31.)

[72] V. M. Hernandez, R. Silva, and H. Sira-Ramirez, "On the stability of limit cycles in resonant DC-to-DC power converters," in *Decision and Control, 2003. Proceedings. 42nd IEEE Conference on*, vol. 2, Dec 2003, pp. 1141–1146 Vol.2. (Cited in page 31.)

[73] F. Carobolante, "Wireless power transfer: Overcoming the technological hurdles," in *2013 Applied Power Electronics Conference (APEC)*, 2013. (Cited in page 41.)

[74] L. Chung, "Wireless power transfer technology," August 2015, accessed: 2016-08-22. [Online]. Available: http://www.eet-cn.com/STATIC/PDF/201509MAPS.pdf (Cited in pages 41 and 42.)

[75] A. for Wireless Power, "A4WP Wireless Power Transfer System Baseline System Specifications (BSS)," November 2013. (Cited in pages 41 and 42.)

[76] R. Tseng, B. von Novak, S. Shevde, and K. A. Grajski, "Introduction to the alliance for wireless power loosely-coupled wireless power transfer system specification version 1.0," in *Wireless Power Transfer (WPT), 2013 IEEE*, May 2013, pp. 79–83. (Cited in pages 41 and 42.)

[77] H. G. Park, J. H. Jang, H. J. Kim, Y. J. Park, S. Oh, Y. Pu, K. C. Hwang, Y. Yang, and K. Y. Lee, "A design of a wireless power receiving unit with a high-efficiency 6.78-MHz active rectifier using shared DLLs for magnetic-resonant A4 WP applications," *IEEE Transactions on Power Electronics*, vol. 31, no. 6, pp. 4484–4498, June 2016. (Cited in pages 41 and 42.)

[78] X. Lu, P. Wang, D. Niyato, D. I. Kim, and Z. Han, "Wireless charging technologies: Fundamentals, standards, and network applications," *IEEE Communications Surveys Tutorials*, vol. 18, no. 2, pp. 1413–1452, Secondquarter 2016. (Cited in pages 41 and 42.)

[79] M. A. de Rooij, "The ZVS voltage-mode class-D amplifier, an eGaN FET-enabled topology for highly resonant wireless energy transfer," in *2015 IEEE Applied Power Electronics Conference and Exposition (APEC)*, March 2015, pp. 1608–1613. (Cited in pages 41 and 42.)

[80] E. P. C. Corporation, "Demonstration System EPC9111 Quick Start Guide: 6.78 MHz, ZVS Class-D Wireless Power System using EPC2014," 2015, accessed: 2016-08-22. [Online]. Available: http://epc-co.com/epc/Portals/0/epc/documents/guides/EPC9111_qsg.pdf (Cited in pages 41 and 42.)

[81] M. A. de Rooij, "Performance comparison for A4WP Class-3 Wireless Power Compliance between eGaN FET and MOSFET in a ZVS Class D Amplifier," in *PCIM Europe 2015; International Exhibition and Conference for Power Electronics, Intelligent Motion, Renewable Energy and Energy Management; Proceedings of*, May 2015, pp. 1–8. (Cited in pages 41 and 42.)

[82] K. G. Moh, F. Neri, S. Moon, P. Yeon, J. Yu, Y. Cheon, Y. s. Roh, M. Ko, and B. H. Park, "A fully integrated 6W wireless power receiver operating at 6.78MHz with magnetic resonance coupling," in *2015 IEEE International Solid-State Circuits Conference - (ISSCC) Digest of Technical Papers*, Feb 2015, pp. 1–3. (Cited in pages 41 and 42.)

[83] J. Lautner and B. Piepenbreier, "Impact of current measurement on switching characterization of GaN transistors," in *Wide Bandgap Power Devices and Applications (WiPDA), 2014 IEEE Workshop on*, Oct 2014, pp. 98–102. (Cited in page 44.)

[84] Y. Ye, D. Liang, J. Du, M. Tang, and X. Liu, "Design and optimization of high frequency current transformer," in *Electrical Machines and Systems (ICEMS), 2014 17th International Conference on*, Oct 2014, pp. 963–966. (Cited in page 44.)

[85] L. Xu, Q. Chen, X. Ren, S. Ping, and S. C. Wong, "Self-oscillating contactless resonant converter with power transfer and current sensing integrated transformer," in *2015 IEEE Energy Conversion Congress and Exposition (ECCE)*, Sept 2015, pp. 4539–4543. (Cited in page 44.)

[86] F. Costa, E. Laboure, F. Forest, and C. Gautier, "Wide bandwidth, large AC current probe for power electronics and EMI measurements," *IEEE Transactions on Industrial Electronics*, vol. 44, no. 4, pp. 502–511, Aug 1997. (Cited in page 44.)

[87] C. H. Chia, P. S. Lei, and R. C. H. Chang, “A high-speed converter with light-load improvement circuit and transient detector,” in *2012 IEEE International Symposium on Circuits and Systems*, May 2012, pp. 456–459. (Cited in page 44.)

[88] H. Mao, “High efficiency high frequency resonant power conversion,” August 2014, uS Patent App. 14/177,049. [Online]. Available: http://www.google.com/patents/US20140225439 (Cited in page 44.)

[89] H. Li and S. Munk-Nielsen, “Challenges in switching SiC MOSFET without ringing,” in *PCIM Europe 2014; International Exhibition and Conference for Power Electronics, Intelligent Motion, Renewable Energy and Energy Management; Proceedings of*, May 2014, pp. 1–6. (Cited in page 44.)

[90] R. W. Erickson, “FM/AM modeling of the envelope transfer function,” http://ecee.colorado.edu/~ecen5817/notes/acmodeling/notes2-13-06.pdf, Accessed: 2016-10. (Cited in page 60.)

[91] ——, “Equivalent circuit modeling,” http://ecee.colorado.edu/~ecen5817/notes/acmodeling/dynamics2.pdf, Accessed: 2016-10. (Cited in page 60.)

[92] ——, “AC modeling slides,” http://ecee.colorado.edu/~ecen5817/notes/acmodeling/ResConvACslides.pdf, Accessed: 2016-10. (Cited in page 60.)

[93] C. L. Phillips and H. T. Nagle, *Digital control system analysis and design.* Prentice Hall Press, 2007. (Cited in page 100.)

[94] American Green Technology, “AGT Introduction Overview,” http://www.agtus.org/knowledgebase/, 2012, Accessed: 2016-08-06, Posted: 2012-11-04. (Cited in page 102.)

[95] N. Tesla, “Experiments with alternate currents of very high frequency and their application to methods of artificial illumination,” in *Transactions of the American Institute of Electrical Engineers*, vol. VIII, 1891, pp. 266–319. (Cited in page 102.)

[96] J. Hooker, “Electrodeless Induction Lamps,” http://www.lamptech.co.uk/Electrodeless.htm, accessed: 2016-08-06. (Cited in page 102.)

[97] D. Tadesse, F. P. Dawson, and S. B. Dewan, “A comparison of power circuit topologies and control techniques for a high frequency ballast,” in *Industry Applications Society Annual Meeting, 1993., Conference Record of the 1993 IEEE*, Oct 1993, pp. 2341–2347 vol.3. (Cited in page 102.)

[98] R. M. Nelms, T. D. Jones, and M. C. Cosby, “A comparison of resonant inverter topologies for hps lamp ballasts,” in *Industry Applications Society Annual Meeting, 1993., Conference Record of the 1993 IEEE*, Oct 1993, pp. 2317–2322 vol.3. (Cited in page 102.)

[99] J. M. Alonso, C. Blanco, E. Lopez, A. J. Calleja, and M. Rico, “Analysis, design, and optimization of the lcc resonant inverter as a high-intensity discharge lamp ballast,” *IEEE Transactions on Power Electronics*, vol. 13, no. 3, pp. 573–585, May 1998. (Cited in page 102.)

[100] C. S. Lin and W. S. Chen, “60 kHz electronic ballast for electrodeless fluorescent lamp,” in *Industrial Technology, 2009. ICIT 2009. IEEE International Conference on*, Feb 2009, pp. 1–6. (Cited in pages 102 and 103.)

[101] A. León-Masich, “High voltage efficient lightning based on the loss-free resistor concept,” Ph.D. dissertation, Department of Electrics, Electronics and Automatic Engineering. Rovira i Virgili University, May 2015. (Cited in pages 105, 106, 108, 111, and 163.)

[102] N. B. Chagas, M. F. da Silva, M. E. Schlittler, J. Fraytag, R. N. do Prado, and F. E. Bisogno, “Electrodeless fluorescent lamps model operated at high frequency,” in *2011 IEEE International Symposium on Industrial Electronics*, June 2011, pp. 245–250. (Cited in pages 105, 106, and 163.)

[103] Osram, “The high-performance electrdeless fluorescent lamp OSRAM ENDURA,” http://www.osram.es/media/resource/HIRES/333886/554635/endura-quicktronic-system--qt-endura.pdf, Accessed: 2016-08-22. (Cited in page 105.)

[104] M. Amin, Y. Arafat, S. Lundberg, and S. Mangold, “Low voltage DC distribution system compared with 230 V AC,” in *Electrical Power and Energy Conference (EPEC), 2011 IEEE*, Oct 2011, pp. 340–345. (Cited in page 109.)

[105] S. Oliver, “High-voltage DC distribution is key to increased system efficiency and renewable-energy opportunities,” http://www.vicorpower.com/documents/whitepapers/wp-High-voltage-DC-Distribution.pdf, Accessed: 2016-08-22, Posted: 2012-11. (Cited in page 109.)

[106] J. Rekola, “DC distribution and power electronics applications in smart grids,” https://webhotel2.tut.fi/units/set/opetus/kurssit/SET_1520/Materiaalit-2012/Jenni_DC-distribution.pdf, accessed: 2016-08-22. (Cited in page 109.)

[107] K. Martín, M. R. Rogina, A. Vázquez, D. G. Lamar, A. Francés, R. Asensi, J. Sebastián, and J. Uceda, “Distribución con nano-redes de corriente continua en el hogar,” in *2016 Seminario Anual de Automática, Electrónica Industrial e Instrumentación (SAAEI 16)*, July 2016. (Cited in page 109.)

[108] M. Kuypers, “Application of 48 volt for mild hybrid vehicles and high power loads,” *SAE Technical Paper 2014-01-1790*, 2014. (Cited in page 109.)

[109] U. Stenzel, “48V mild hybrid systems: Market needs and technical solutions,” https://www.avl.com/documents/10138/1379144/AVL_UK_Expo_

48V_Mild_Hybrid_Systems.pdf, accessed: 2016-08-22, Posted: 2014. (Cited in page 109.)

[110] M. Fuhrer, "LV 124 & LV 148: Electrical normative basics and practical challenges for vehicle components and systems," http://www.testforce.com/testforce_files/Seminars/SpirentAutomotiveSeminar2016/SpirentAutomotiveLV124-LV148V.pdf, accessed: 2016-08-22, Posted: 2016-04-05. (Cited in page 109.)

[111] Infineon Technologies, "Infineon IPB200N15N3 datasheet," http://www.infineon.com/dgdl/Infineon-IPB200N15N3+G-DS-v02_07-EN.pdf?fileId=5546d4624fb7fef2014ff59230602dbb, 2014, Accessed: 2016-08-22, Posted: 2014-01-09. (Cited in page 112.)

[112] Texas Instruments, "Texas Instruments UCC2721X datasheet," http://www.ti.com/lit/ds/symlink/ucc27211.pdf, 2014, Accessed: 2016-08-22, Posted: 2014-12. (Cited in page 113.)

[113] Coilcraft, "Coilcraft AGP4233 Power Inductors datasheet," http://www.coilcraft.com/pdfs/agp4233.pdf, 2014, Accessed: 2016-08-22, Posted: 2014-12-12. (Cited in page 113.)

[114] C. Close, *The analysis of linear circuits.* Harcourt, Brace & World, 1966. (Cited in page 143.)

LIST OF PUBLICATIONS

Journal Articles

[JA1] R. Bonache-Samaniego, C. Olalla, and L. Martínez-Salamero, "Dynamic modeling and control of self-oscillating parallel resonant converters based on a variable structure systems approach," *IEEE Transactions on Power Electronics*, vol. 32, no. 2, pp. 1469–1480, 2017.

[JA2] R. Bonache-Samaniego, C. Olalla, L. Martínez-Salamero, and H. Valderrama-Blavi, "Design of self-oscillating resonant converters based on a variable structure systems approach," *IET Power Electronics*, vol. 9, no. 1, pp. 111–119, 2016.

Conference Articles

[CA1] R. Bonache-Samaniego, C. Olalla, L. Martínez-Salamero, and D. Maksimovic, "6.78 MHz self-oscillating parallel resonant converter based on GaN technology," in *2017 Applied Power Electronics Conference (APEC 2017)*, March 2017, pp. 1–8.

[CA2] R. Bonache-Samaniego, C. Olalla, and L. Martínez-Salamero, "Análisis orientado al diseño de un convertidor resonante LCC auto-oscilante," in *2016 Seminario en Automática, Electrónica Industrial e Instrumentación (SAAEI 2016)*, July 2016, pp. 1–6.

[CA3] C. Olalla, R. Bonache-Samaniego, and L. Martínez-Salamero, "Dynamic modeling of self-oscillating resonant converters," in *2015 IEEE 16th Workshop on Control and Modeling for Power Electronics (COMPEL 2015)*, July 2015, pp. 1–8.

[CA4] R. Bonache-Samaniego, C. Olalla, and L. Martínez-Salamero, "Diseño de convertidores resonantes auto-oscilantes basado en control de estructura variable," in *2015 Seminario en Automática, Electrónica Industrial e Instrumentación (SAAEI 2015)*, July 2015, pp. 549–554.

Patents

[PA1] R. Bonache-Samaniego, C. Olalla, and L. Martínez-Salamero, "Balastro electrónico auto-oscilante con atenuación de luz para una lámpara y sistema que lo incluye," Spanish Patent P201 631 618 (Patent Pending), 2016.

UNIVERSITAT ROVIRA i VIRGILI

Automatic Control and Industrial Electronics Group

DOCTORAL THESIS

Self-oscillating resonant converters: general approach and applications

Ricardo Bonache Samaniego

2016